Biogeochemical cycling and paleoenvironmental reconstructions of the Toarcian Oceanic Anoxic Event from western North America

Theodore Roland Them, II

Dissertation submitted to the faculty of the Virginia Polytechnic Institute and State University in partial fulfillment of the requirements for the degree of

Doctor of Philosophy
In
Department of Geosciences

Benjamin C. Gill
Kenneth A. Eriksson
Brian W. Romans
Shuhai Xiao

June 2, 2016
Blacksburg, Virginia

Keywords: Toarcian Oceanic Anoxic Event; carbon isotope excursion; abrupt climate change; chemical weathering; anoxia; euxinia; iron speciation

Biogeochemical cycling and paleoenvironmental reconstructions of the Toarcian Oceanic Anoxic Event from western North America

Theodore Roland Them, II

ABSTRACT

The Toarcian Oceanic Anoxic Event (T-OAE; ~183 million years ago) represents an interval during the Mesozoic when the emplacement of the Karoo-Ferrar Large Igneous Province (LIP) is thought to have resulted in significant environmental change. Associated with this interval was the widespread deposition of organic-rich sediments, carbon cycle and seawater chemistry changes, global warming, the development of marine anoxia, and major extinction events. The majority of studies of this event that have documented these responses have come from the Boreal and Tethyan regions of Europe, thus casting some doubt to the regional versus global significance of the event. Thus my dissertation has sought to reconstruct biogeochemical and paleoenvironmental changes across the T-OAE from a sedimentary succession that was deposited on the margins of a different ocean basin away from the well-studied European successions. Specifically, I have studied the chemostratigraphy of the Fernie Formation of the Western Canada Sedimentary Basin (WCSB), which was deposited on the eastern margin of the Panthalassa Ocean. The Toarcian carbon isotope excursions (CIEs) in the WCSB confirm that these features are global phenomena. I have suggested a new driver for small-scale CIEs observed during the event: the release of wetland-derived methane during progressive global warming. The osmium isotope record and numerical modeling of the osmium cycle suggests that continental weathering rates increased during the T-OAE by 230 – 540%. Rhenium abundance data also suggests that the increased geographic extent of marine anoxia during the T-OAE caused a global drawdown in the seawater rhenium inventory. Iron speciation data are used to

reconstruct redox conditions within the WCSB, which suggest ferruginous conditions developed in the more distal locations at the onset of the T-OAE before returning to euxinic (anoxic and sulfidic) conditions. This is likely related to enhanced pyrite burial on a global scale, which caused the drawdown of the seawater sulfate inventory, thus limiting pyrite formation in the distal locations. The proximal setting remained euxinic across the T-OAE, and in all locations the iron speciation data suggest anoxic conditions persistent well after the interval that has been traditionally called the end of the T-OAE.

Dedication

This dissertation is dedicated to my grandfather, the original T.R. Them.

Acknowledgments

I would first like to thank my committee chair, Ben, for taking me on as your first PhD student. The last four years have been filled with wonderful experiences, of which I will always remember. You have helped me develop into a much better geologist and have guided me through all the novel and state-of-the-art geochemical procedures that we use to reconstruct ancient environments preserved in the sedimentary record. I also appreciate all of your patience as it pertains to me actually writing this dissertation. I look forward to collaborating with you in the future and maintaining our friendship.

I would like to thank my committee members Ken Eriksson, Brian Romans, and Shuhai Xiao. Ken, I have a new appreciation for the evolution of the Appalachian system, and especially tidalites. I'm glad I was able to help your former student, Ty, with the geochemical aspects of his project on the Pride Shale. I hope someone will continue that work in much finer detail, as it is a very interesting geological unit and may have important implications on better understanding ancient monsoonal systems. Brian, I thoroughly enjoyed watching sand move on the beach with you. Sometimes it is just more exciting watching geology happen in front of our eyes. I promise that I will help out in any way that I can regarding future field excursions. Shuhai, it has been a pleasure listening and learning while you lecture. Also, we have yet to determine who is the master ping-pong player in our best-of-three series; the score remains 1-1. I will miss discussing all aspects of geology in our PaleoSedStrat seminars and hope that wherever I end up, these types of learning experiences will continue to occur.

I would also like to acknowledge some of my collaborators, including Andrew Caruthers, Darren Gröcke, Rowan Martindale, Terry Poulton, Dave Selby, Paul Smith, and João Trabucho-

Alexandre. Andrew and Darren (and Ben), I look forward to working with you guys in the future, as I know we have plenty of projects in the back of our minds. I think we're a pretty good team who also know how to have fun.

Thank you to all of the Seddies who have cohabitated our wonderful office in the windowless corner of Room 1091, Derring Hall. Our first group, Cody, Neal, Pat, Ty, and Angela, I am not sure how we survived each other, but it was definitely a ride worth remembering. I am sure we will all continue to the best of friends in Houston, if there are ever jobs again. As the saying goes, "first is the worst" (unknown philosopher, potentially a geologist), and I'd also like to thank Group 2 (who encouraged the last quote), including Cody and Neal (again), and Kristin, Matt, Sarah, and Sam. I have enjoyed our time together, and I'm sure that you will all be successful.

Thank you to my former mentee, Emma. I appreciate all the help you gave me over the past couple years, and I hope that you learned a thing or two along the way. Keep up the good work.

Thank you to my parents, who pushed me to work hard in school and in life. I appreciate all the support you have given me.

To my sister, Alexis, brother-in-law, Bryan, and nephew, Peter, thank you for everything. I always look forward to visiting you in Ithaca and just relaxing. You are doing a great job as parents and I look forward to watching Peter grow up. Thank you for coming to my graduation, even though I still had yet to defend this dissertation! And to Peter, who thought I was dressed in a superhero cape to be in a talent show during my graduation (it was just my gown), you are

probably too smart for your own good. Also, Alexis and Bryan, I look forward to meeting my newest niece or nephew later this year.

To Leslie, thank you for everything. We met at what may have been one of the busiest times of my life. Your patience with me is much appreciated, and I am so thankful for the time that we get to spend together. I'd also like to acknowledge FaceTime for making our long distance situation just a little more bearable. I am looking forward to traveling around the U.S. for a substantial part of the summer, and then flying out to England to attend Darren's wedding, before the big move to Tallahassee.

Thanks to my mentors from my previous academic institutions. Sean Cornell, the only geologist at Shippensburg University, introduced me to research as an undergraduate and paved the way for the rest of my academic career. Matthew Schmidt and Niall Slowey, at Texas A&M University, gave me wonderful opportunities to conduct fascinating research in paleoclimatology and paleoceanography, and helped me grow into the scientist I am today.

Finally, I'd like to thank my friends and colleagues and the department faculty and staff for making my time at Virginia Tech a great experience. I also want to extend my gratitude to the National Science Foundation, Virginia Tech College of Science Roundtable committee, Virginia Tech Department of Geosciences, Geological Society of America, American Association of Petroleum Geologists, Society for Sedimentary Geologists, International Association of Sedimentologists, ConocoPhillips, and Statoil. The support received from these sources offset the total cost of tuition, fees, stipend, travel support, and all geochemical analyses. This research would not have been possible without it.

TABLE OF CONTENTS

LIST OF FIGURES

Chapter 1

Chapter 2

Chapter 3

LIST OF TABLES

Chapter 1

Nomenclature

OAE	Oceanic Anoxic Event
CIE	Carbon Isotope Excursion
T-OAE	Toarcian Oceanic Anoxic Event
LIP	Large Igneous Province
TOC	Total Organic Carbon
WCSB	Western Canada Sedimentary Basin
PCS	Poker Chip Shale
MSR	Microbial Sulfate Reduction
Ma	Mega-annum
Kyr	Kiloyear
Fe_T	Total Iron
Fe_{HR}	Highly Reactive Iron
Fe_{py}	Pyrite Iron
Fe_{carb}	Carbonate-Hosted Iron
Fe_{ox}	Oxyhydroxide-Hosted Iron
Fe_{mag}	Magnetite-Hosted Iron

Introduction

Oceanic anoxic events (OAEs) represent time intervals in the Mesozoic of the widespread deposition of organic-rich sediments. OAEs are thought to represent the culmination of feedbacks within the Earth system to significant increases in greenhouse gases content of the atmosphere caused by the emplacement of large igneous provinces (LIPs). This dissertation focuses on the oldest identified OAE, the Toarcian OAE or T-OAE of the Early Jurassic (~183 million years ago). The overwhelming majority of studies that have focused on this time interval have come from the Boreal and Tethyan regions of Europe. Thus, there has been considerable debate over the last 15 years regarding the global versus regional extent of environmental changes associated with the T-OAE. These three chapters are focused on biogeochemical and paleoenvironmental changes that occurred in eastern Panthalassa during the Pliensbachian to Toarcian interval recorded in stratigraphic sections of Fernie Formation from the Western Canada Sedimentary Basin.

Chapter 1 presents an organic carbon isotope ($\delta^{13}C_{org}$) stratigraphy from an outcrop section of the Fernie Formation located at Ya Ha Tinda in the foothills of the Canadian Rocky Mountains of Alberta. With these data I have identified the negative carbon isotope excursion (CIE) associated with the T-OAE. This was possible by pairing the carbon isotope data with high-resolution ammonite biostratigraphy that was determined by my collaborator Andrew Caruthers of Western Michigan University. Further, I also identified the small-scale CIEs observed on the onset of the broader Toarcian CIE elsewhere. This is the first time that these features have been observed in a record outside of Europe. I propose a new mechanism for the generation of these small-scale CIEs: enhanced methanogenesis in wetlands. Wetlands represent an important source of greenhouse gases, such as methane, and have generally been overlooked

when determining causal mechanisms of abrupt global warming events the past. This work represents an important contribution to better understanding not only the mechanisms behind Toarcian climate change, but also may be applied to other intervals of abrupt climate change after the proliferation of land plants (e.g., Cretaceous OAEs, end-Permian, end-Triassic).

Chapter 2 presents a rhenium and osmium record from the same section studied in Chapter 1. I generated these data at Durham University with my colleagues, David Selby and Darren Gröcke. With these data I have identified an osmium isotope excursion ($^{187}Os/^{188}Os$) associated with the T-OAE. This is important because it demonstrates that 1) during the T-OAE, increased amounts of continental materials were delivered to the global oceans; 2) increased chemical weathering rates were a feedback to Toarcian global warming and enhanced hydrological cycle; and 3) that more broadly silicate weathering may sequester atmospheric CO_2 on shorter timescales ($10^3 – 10^4$ yr) than what is generally accepted (>10^6 yr). Further, I have also utilized a forward box model to investigate and quantify the Toarcian osmium cycle. Model simulations suggest that weathering rates increased by 230 – 540% during the T-OAE, which may represent one of the largest observed during the Phanerozoic. I have also identified significant decreases in rhenium abundances during the T-OAE, which suggests increased geographic extent of marine anoxia and the global drawdown of its seawater inventory. I compared my dataset to one available from Europe, and I argue that the European dataset was heavily modified by local or regional oceanographic processes. This work represents an important contribution to better understanding how silicate weathering may change and be an important climate feedback on short timescales, and its potential relation to enhanced primary productivity and subsequent marine anoxia.

Chapter 3 presents the first proximal-to-distal carbon isotope records from a basin outside Europe. With these data I have identified the Toarcian CIE at each site, confirming the ubiquity of this CIE as a chemostratigraphic marker. In this chapter, iron speciation data are also presented from each site, which are used to reconstruct redox conditions in the WCSB across the T-OAE. I argue that the most proximal location was euxinic (anoxic and sulfidic) during the T-OAE and into the middle to late Toarcian, and that the distal locations became ferruginous during the onset of the T-OAE, and later transitioning to euxinia at the same time (constrained by $\delta^{13}C_{org}$ values). I interpret these data as the consequence of both the global and local drawdown of sulfate, which was a function of the global increase in pyrite burial rates during the T-OAE. This dataset is broadly similar to an unpublished iron speciation dataset from England, suggesting a similar redox response during the T-OAE. This work represents an important contribution to understanding the variability of marine anoxia both spatially and temporally across an OAE. I argue that the WCSB was also anoxic before and after the T-OAE, which does not fit the paradigm of oxic-anoxic-oxic conditions describing the ocean redox state before, during, and after an OAE. I suggest that the paleoceanographic community redefines the temporal extent of OAE.

Chapter 1

High-resolution carbon isotope records of the Toarcian Oceanic Anoxic Event (Early Jurassic) from North America and implications for the global drivers of the Toarcian carbon cycle

T.R. Them II[a,*], B.C. Gill[a], A.H. Caruthers[b,c], D.R. Gröcke[d], E.T. Tulsky[a], R.C. Martindale[e], T.P. Poulton[f], P.L. Smith[b]

[a] Department of Geosciences, Virginia Tech, 1405 Perry St., Derring Hall RM4044, Blacksburg, VA 24061, USA

[b] Department of Earth, Ocean and Atmospheric Sciences, University of British Columbia, Vancouver, V6T 1Z4, Canada

[c] Department of Geosciences, Western Michigan University, 5272 W Michigan Ave, Kalamazoo, MI 49006, USA

[d] Department of Earth Sciences, Durham University, South Road, Durham DH1 3LE, UK

[e] Department of Geological Sciences, University of Texas at Austin, 1 University Station C1100, Austin, TX 78712, USA

[f] Geological Survey of Canada, 3303 33 St. NW, Calgary, Alberta T2L 2A7, Canada

[*]Corresponding author: theo1085@vt.edu (T.R Them II).

Formatted for *Earth and Planetary Science Letters*

Abstract

The Mesozoic Era experienced several instances of abrupt environmental change that are associated with instabilities in the climate, reorganizations of the global carbon cycle, and elevated extinction rates. Often during these perturbations, oxygen-deficient conditions developed in the oceans resulting in the widespread deposition of organic-rich sediments — these events have been referred to as Oceanic Anoxic Events or OAEs. Such events have been linked to massive injections of greenhouse gases into the ocean-atmosphere system by transient episodes of voluminous volcanism and the destabilization of methane clathrates within the marine reservoir. Nevertheless, uncertainty surrounds the specific environmental drivers and feedbacks that occurred during OAEs that caused perturbations in the carbon cycle; this is particularly true of the Early Jurassic Toarcian OAE (~183.1 Ma). Here, we present biostratigraphically constrained carbon isotope data from western North America (Alberta and British Columbia, Canada) to better assess the global extent of the carbon cycle perturbations. We identify the large negative carbon isotope excursion associated with the OAE along with high-frequency oscillations and steps within the onset of this excursion. We propose that these high-frequency carbon isotope excursions reflect changes to the global carbon cycle and also that they are related to the production and release of methanogenic gases from terrestrial wetlands on astronomical timescales. Furthermore, increased wetland methanogenesis should be considered an important climatic feedback during Ocean Anoxic Events and other similar events in Earth history after the proliferation of land plants.

1. Introduction

The Early Jurassic Toarcian Oceanic Anoxic Event (T-OAE) represents a time of severe global environmental change that has been associated with a major extinction of marine organisms (Harries and Little, 1999; Guex et al., 2012; Sandoval et al., 2012; Caruthers et al., 2014; Danise et al., 2015), widespread deposition of organic-rich sediments (Jenkyns, 1988), and large-scale perturbations to the global carbon cycle recorded as carbon isotope excursions (CIEs) (e.g., Jenkyns and Clayton, 1997; Hesselbo et al., 2000). To date, the large negative CIE has been recognized in organic carbon, carbonate carbon, and fossil wood, indicating that the global carbon cycles in the marine and terrestrial realms were affected during the T-OAE (Fig. 1) (e.g., Hesselbo et al., 2000). While initial studies identified a Toarcian CIE of up to -8‰ in magnitude, recent studies indicate the absolute global magnitude of the CIE as only -3‰ to -4‰ (Schouten et al., 2000; van Breugal et al., 2006; French et al., 2014; Suan et al., 2015). U-Pb age dates around the Toarcian CIE estimate the duration to be ~300 kyr (Sell et al., 2014), and a recent age model based on orbital tuning suggests a duration of ~500 kyr (Boulila et al., 2014), which is a similar timeframe as the CIE associated with the much younger Paleocene-Eocene Thermal Maximum (PETM) (Hesselbo et al., 2000; Cohen et al., 2007). The PETM is thought to have been the result of a massive transitory release of carbon to the ocean–atmosphere system via marine clathrate destabilization, volcanic outgassing, oxidation of organic matter, increased terrestrial methane cycling, or a combination of these drivers (Dickens et al., 1995; Svensen et al., 2004; Storey et al., 2007; Higgins and Schrag, 2006; Pancost et al., 2007; Panchuk et al., 2008). Similar forcings have also been implicated for the Toarcian OAE (e.g., Hesselbo et al., 2000; McElwain et al., 2005; Svensen et al., 2007; Beerling and Brentnall, 2007).

High-resolution sampling over the falling limb of the Toarcian CIE has identified small-scale CIEs — described by some authors as abrupt steps or oscillations — recorded in organic and carbonate carbon and fossil wood at several geographic locations in the former Tethys and Boreal seas (Kemp et al., 2005; Hesselbo et al., 2007; Hermoso et al., 2009; Hesselbo and Pieńkowski, 2011; Hermoso et al., 2012). These small-scale CIEs have been interpreted to represent discrete methane clathrate destabilization events tied to astronomically forced changes to the global climate (Kemp et al., 2005; Hesselbo and Pieńkowski, 2011; Hermoso et al., 2012) (Fig. 1).

The temporal association of the T-OAE with the emplacement of the Karoo-Ferrar large igneous province (LIP) (Pálfy and Smith, 2000; Svensen et al., 2007; Caruthers et al., 2013, 2014; Sell et al., 2014; Burgess et al., 2015) has led to the proposition of a causal correlation of these events to the CIE through injection of mantle-derived carbon dioxide (CO_2) into the atmosphere. This scenario would lead to a cascade of synergistic environmental feedbacks, including global warming, increased precipitation and weathering, ocean anoxia and acidification, and marine extinctions (Caruthers et al., 2013, 2014; Bond and Wignall, 2014). Importantly, Ferrar sills intrude through coal seams, which may have released additional methane and carbon dioxide into the atmosphere (McElwain et al., 2005; Svensen et al., 2007), but the significance of this process in the Toarcian carbon cycle has been disputed (Gröcke et al., 2006).

Although some studies have challenged the global nature of the Toarcian carbon cycle perturbations (e.g., Wignall et al., 2006), new geochemical records from outside European Boreal and Tethyan regions support the global extent of the Toarcian CIE; it has now been documented in Argentina (Al-Suwaidi et al., 2011, 2016), the Arctic (Suan et al., 2011), British

Columbia (Caruthers et al., 2011, 2014), and Japan (Gröcke et al., 2011; Izumi et al., 2012; Kemp and Izumi, 2014) (Fig. 2). Nevertheless, the small-scale CIEs observed in the falling limb of the Toarcian CIE in records from Europe (Fig. 1) have not been documented at these new localities due to lower sampling resolution; therefore, it is uncertain whether these small-scale CIEs are truly global in nature. However, a recent study of $\delta^{13}C$ of fossil wood from Europe suggests that these small-scale CIEs also occurred in atmospheric carbon dioxide and were thus global phenomena (Hesselbo and Pieńkowski, 2011). Understanding the nature and extent of these small-scale CIEs is imperative for distinguishing carbon-isotope excursions as either global events or as byproducts of regional oceanographic or tectonic processes.

Herein, we present a biostratigraphically-constrained, high-resolution, organic carbon isotope ($\delta^{13}C_{org}$) records from two western North American sites that were located in eastern Panthalassa (Fig. 2). These new and recently published data constitute the most detailed carbon isotope record of the Toarcian OAE and surrounding intervals outside the European region. Taken together, the data reveal that small-scale CIEs on the falling limb of the large Toarcian CIE were, in fact, global phenomena, providing strong evidence for multiple global carbon cycle perturbations during the initiation of the Toarcian CIE.

2. Study locations

The Fernie Formation of Alberta and British Columbia comprises Jurassic strata deposited in the Western Canada Sedimentary Basin. The formation crops out in the foothills of the Canadian Rocky Mountains and is present in the subsurface to the north and east (Frebold, 1957; Hall, 1984; Poulton and Hall, 1993; Asgar-Deen et al., 2003). The Pliensbachian to Aalenian interval of the Fernie Formation has been identified in outcrop and drill cores with

ammonite biostratigraphy (Frebold, 1957; Hall, 1984; Poulton and Hall, 1993; Asgar-Deen et al., 2003), and was recognized as a potential area to identify the Toarcian CIE (Asgar-Deen et al., 2003). Jenkyns (1988) considered the Poker Chip Shale as the lithologic expression of the T-OAE in his global compilation of Early Jurassic organic-rich facies, though the resolution of the biostratigraphic data was insufficient to definitively link the Poker Chip Shale Member to the T-OAE.

We present an expanded section of the Pliensbachian and Toarcian interval measured along East Tributary of Bighorn Creek located in Ya Ha Tinda Ranch, Alberta. At the East Tributary section, the Pliensbachian and Toarcian stages consist of dominantly organic-rich calcareous mudstones and siltstones of the Red Deer and Poker Chip Shale members of the Fernie Formation (Fig. 3). The diverse ammonite assemblages preserved in this succession indicate late Pliensbachian to middle Toarcian stages (Hall et al., 1998) and provide the framework for global correlation of our geochemical records (Fig. 3). We cannot disclose the precise location (GPS coordinates) of the East Tributary section because it is a fossil-bearing locality and is protected under the Canadian National Parks Act. However, enquiries about the site for scientific investigation can be directed to Parks Canada or the Royal Tyrrell Museum of Palaeontology in Drumheller, Canada; the East Tributary of Bighorn Creek is Royal Tyrrell Museum of Palaeontology Locality #L2428.

We also provide a high-resolution $\delta^{13}C_{org}$ record from a site located on the Yakoun River in Haida Gwaii, western British Columbia, where the Toarcian CIE has been previously identified (Caruthers et al., 2011, 2014). The Haida Gwaii sequence was deposited in a relatively open-ocean environment on the allochthonous Wrangellia terrane, although its original position (with respect to North America) is enigmatic (Caruthers et al., 2011, 2014). Here, the Toarcian is

part of the Whiteaves Formation, and the CIE interval generally consists of slightly elevated total organic carbon (TOC) siltstones (Caruthers et al., 2011).

3. Methods

3.1 Sampling and geochemical analyses

Hand samples were initially collected in outcrop from the East Tributary section at a decimeter-scale along with ammonite fossils for biostratigraphic control (see Supplementary Data). Later, a portable Shaw Backpack Drill was used to recover a continuous sequence of strata in order to perform an ultra high-resolution sampling (cm- to mm-scale) across the carbon isotope excursion. Rock samples were subsampled for geochemical analyses using a handheld Dremel tool. 2N HCl was added to approximately 0.1 g of sample powder and allowed to react for ~24 hours in order to remove the carbonate fraction. The acid was removed and sample was then brought to a neutral pH with multiple rinses with deionized water and dried in an oven. Total organic carbon (TOC) and $\delta^{13}C_{org}$ values of the carbonate-free residues were analyzed by an Isotope Cube elemental analyzer connected to an Isoprime 100 gas source isotope-ratio mass spectrometer (IRMS) in the Department of Geosciences at Virginia Tech. Stable-isotope measurements of the samples from Haida Gwaii were performed at Durham University using a Costech Elemental Analyser (ECS 4010) coupled to a ThermoFinnigan Delta V Advantage (wet chemical procedures were similar to those described above).

The isotope composition of the samples is expressed in the standard delta (δ) notation as per mil deviations (‰) from Vienna Pee Dee Belemnite (VPDB) using the following equation:

$$\delta^{13}C = \left[\frac{\left[\frac{^{13}C}{^{12}C}\right]_{sample} - \left[\frac{^{13}C}{^{12}C}\right]_{standard}}{\left[\frac{^{13}C}{^{12}C}\right]_{standard}} \right] \times 1000 \quad (1)$$

The East Tributary samples were calibrated to the VPDB scale using international (IAEA-CH-6 and IAEA-CH-7) and commercial standards (wheat flour, sorghum flour, low organic soil, and urea). Long-term analytical precision for the $\delta^{13}C$ measurements is 0.1 ‰ based on replicated analyses on isotope standards: this provided a linear range in $\delta^{13}C$ between -48.66‰ and -10.42‰. Total organic carbon was obtained as part of the isotopic analysis using internal standards (i.e., Acetanilide, 71.09% C). Approximately 31% of hand samples (n = 128) were replicated at least once; 71% of drill core samples (n = 69) were replicated at least once. Average analytical uncertainty for replicated analyses (n = 89) was 0.07‰. For the Haida Gwaii samples that were analyzed at Durham, data accuracy is monitored through routine analyses of in-house standards, which are stringently calibrated against international standards (e.g., USGS 40, USGS 24, IAEA 600): this provided a linear range in $\delta^{13}C$ between –46.7‰ and +2.9‰. Analytical uncertainty for $\delta^{13}C_{org}$ measurements is typically ±0.1‰ for replicate analyses of the international standards and typically <0.2‰ on replicate sample analysis. Total organic carbon was obtained as part of the isotopic analysis using an internal standard (i.e., Glutamic Acid, 40.82% C).

All ammonite specimens from the East Tributary section are curated at the Royal Tyrrell Museum of Palaeontology in accordance with Provincial laws. Ammonites were excavated with hand tools (rock hammers, sledges, picks, chisels and brushes) and power tools (Hilti TE 500-AVR Demolition Hammer and Hilti DEG 600 6" Angle grinder with a diamond blade). Fossils that broke during excavation or transportation were glued together with Paraloid B-72

consolidate (diluted with acetone); where fossil material was flaking (drying of the shales), a thin coat of Primal WS-24 (a water soluble acrylic polymer) was used to veneer the top surface of the specimen to keep it intact. Full details of fossil preparation or consolidation for each specimen are recorded in the Royal Tyrrell Museum of Palaeontology specimen database. All fossils and geological samples were collected under a Parks Canada collection and research permit (#YHTR-2014-16156) and fossil excavation permits from the Alberta Government (RTMP Permit #13-058, #14-009, and #15-019).

4. Results

4.1 Biostratigraphy

Here we report new biostratigraphic data from the East Tributary section. The biostratigraphy from the Haida Gwaii section can be found in Caruthers et al. (2011). Specimens of *Amaltheus*, *Protogrammoceras*, and *Tiltoniceras* occur below the negative CIE interval at East Tributary, from 0 to 10.9 m, and indicate a late Pliensbachian to early Toarcian age (Smith and Tipper, 1996). Of these specimens, *Amaltheus*, *P. kurrianum*, and *P. skidegatense* are restricted to the late Pliensbachian (Kunae and Carlottense Zones) while in western North America *T.* cf. *antiquum*, and *P. paltum*, are known to span the Pliensbachian–Toarcian boundary (Smith and Tipper, 1996). From ~10 to 16 m in the section, species of *Dactylioceras, Cleviceras*, *Hildaites*, and *Harpoceras* occur in abundance and span the negative CIE interval. In northwest Europe these genera are common throughout the early Toarcian Tenuicostatum and Serpentinum zones (Howarth, 1992) and in western North America they represent the larger Kanense Zone (Jakobs et al., 1994, Jakobs, 1997). Above the negative CIE interval *Zugodactylites*, *Dactylioceras commune*, *D. athleticum*, *Harpoceras* cf. *subplanatum*, *Pseudolioceras* cf. *lythense*,

Peronoceras, and *Phymatoceras* occur from ~16 to 22 m in the section. Of these species, only *D. athleticum* and *D. commune* are known to span the early–middle Toarcian boundary (Howarth, 1962; Howarth, 1992), while the other taxa from this interval are restricted to the middle Toarcian Bifrons Zone from Europe and Russia or Planulata Zone of western North America (Howarth, 1992; Jakobs, 1997; Howarth, 1978).

4.2 Carbon isotope chemostratigraphies

Our new high-resolution organic carbon isotope ($\delta^{13}C_{org}$) record from East Tributary shows the prominent negative CIE that occurs over 5 meters of strata within the Kanense Zone of the Early Toarcian, confirming this is the CIE associated with the T-OAE (Fig. 3). In this section, data show an overall decrease in $\delta^{13}C_{org}$ values with high-frequency variations from ~ -27‰ to -30‰ over a decimeter at the Red Deer–Poker Chip Member transition (Fig. 3). Values remain at ~ -30.5‰ for 1.3 meters, approaching a minimum of -30.7‰, before gradually increasing to -26.8‰ over the next four meters. Post-CIE $\delta^{13}C_{org}$ values are relatively constant at approximately -27.5‰, which is similar to European $\delta^{13}C_{org}$ datasets. The overall magnitude of the excursion of -3.5‰ is also consistent with compound-specific carbon isotope records in Europe and those values suggested for the true global magnitude of the Toarcian CIE (Schouten et al., 2000; van Breugal et al., 2006; French et al., 2014; Suan et al., 2015). In the Yakoun River Section, high-resolution $\delta^{13}C_{org}$ values show a positive trend immediately before the CIE (Fig. 4). On the falling limb, high-frequency "steps" are present from ~ -25‰ to -32‰ over a meter interval. Over the next 5 meters in the Yakoun River Section, there are several $\delta^{13}C_{org}$ oscillations on the order of 0.5‰ that occur over the most negative interval of the Toarcian CIE.

5. Discussion

5.1 The Toarcian carbon isotope records

Along with other recently published records outside of the Tethyan and Boreal regions (Fig. 2), the new biostratigraphic and $\delta^{13}C_{org}$ records reported here confirm the assertion that the broader Toarcian CIE was a global phenomenon. It is difficult to envision a scenario where the eruption of a sizeable igneous province would trigger oceanographic changes isolated to the Tethys and Boreal seas if the Karoo-Ferrar were the ultimate driver of the T-OAE. Importantly, these new high-resolution records from western Canada document multiple, small-scale CIEs in $\delta^{13}C$ in the falling limb of the overall T-OAE CIE at both locations and indicate that these features also represent global perturbations to the carbon cycle.

Apart from the overall influence of the Karoo-Ferrar LIP on the global carbon cycle, one of the more fascinating features of this Toarcian CIE is its highly dynamic falling limb. The abrupt small-scale CIEs within this interval of the overall CIE may have been generated by the destabilization of methane clathrate reservoirs linked to astronomically paced changes in climate and oceanic circulation (Kemp et al., 2005; Hesselbo and Pieńkowski, 2011; Hermoso et al., 2012). However, whether the apparently abrupt nature of the small-scale CIEs is reflective of the process that drove them has recently been challenged (Trabucho-Alexandre, 2014). A detailed analysis of the sedimentology from one of the best-studied Toarcian successions at Yorkshire in the United Kingdom suggests that the sequence contains several sedimentary hiatuses that have changed the morphology of $\delta^{13}C$ record. Specifically, these changes in sediment accumulation resulted in the abrupt or stepped appearance of the small-scale CIEs (Trabucho-Alexandre, 2014) (Fig. 1). While depositional rates and erosion likely played a role in the shape of the $\delta^{13}C$ datasets at Yorkshire and certainly other Toarcian successions (e.g., Hesselbo and Pieńkowski,

2011; Hermoso et al., 2012) in Europe, a similar number of small-scale CIEs between sections is evidence that they are likely correlative to one another and represent true perturbations to the carbon cycle. It has also been proposed that the small-scale CIEs are a product of variation in the mixing of different sources of organic matter (Suan et al., 2015). However, the fact that these small-scale CIEs are also present in both carbonate carbon (Hermoso et al., 2009, 2012) and higher plant matter (Hesselbo and Pieńkowski) (Fig. 1) suggests that they represent carbon cycle perturbations.

The high-resolution western North American $\delta^{13}C$ records (Fig. 4) presented here are certainly less complete than some European records. The North American successions are more condensed during the onset of the Toarcian CIE and potentially contain significant sedimentary gaps as evidenced by the abrupt jumps in the $d^{13}C$ records. However, these records display similar small-scale CIEs that are likely correlative to those observed in European records (Kemp et al., 2005; Hesselbo et al., 2007; Hermoso et al., 2009; Hesselbo and Pieńkowski, 2011; Hermoso et al., 2012). Therefore, based on our datasets combined with the existing European records, it is evident that during the initial phase of the CIE, there were indeed higher-frequency changes within the global carbon cycle.

5.2 Drivers of the Toarcian carbon cycle perturbations

Previous studies have suggested that the Toarcian CIE may have been caused by one or a combination of the following mechanism(s): efflux of mantle-derived carbon, methane hydrate destabilization, or thermogenic methane release related to the emplacement of the Karoo-Ferrar LIP (Hesselbo et al., 2000, Pálfy and Smith, 2000; McElwain et al., 2005; Svensen et al., 2007; Beerling and Brentnall, 2007) (see Table S1) with discrete methane clathrate destabilization events as the cause of the multiple, small-scale CIEs on the falling limb (Kemp et al., 2005;

Hesselbo and Pieńkowski, 2011; Hermoso et al., 2012). However, modeling of the Toarcian carbon cycle (Beerling and Brentnall, 2007) has shown that these forcings do not fully explain the magnitude of the Toarcian CIE and the associated climatic responses (McElwain et al., 2005, Beerling and Brentnall, 2007). Simulations involving thermogenic emissions of CH_4 from the Karoo-Ferrar LIP also cannot reproduce the magnitude of the CIE or result in carbon fluxes, which vastly exceeds the estimates (McElwain et al., 2005) for the increased atmospheric pCO_2 during the T-OAE (Beerling and Brentnall, 2007). Invoking methane clathrate destabilization requires a substantial amount of methane (>6,000 Gt C) (Beerling and Brentnall, 2007) that greatly exceeds estimates of the modern clathrate reservoir (~500 – 2500 Gt C) (Milkov, 2004); and given the greenhouse climate of the Early Jurassic, the size of the standing clathrate reservoir potentially may have been substantially less. Moreover, in order to produce the short-term oscillations observed in the carbon isotope record, large clathrate releases would need to be followed by rapid and repeated replenishment of the marine clathrate reservoir, which is an unlikely scenario under a progressively warming climate (McElwain et al., 2005; Wignall et al., 2006).

We propose a new feedback mechanism to help explain the Toarcian carbon isotope excursions — enhanced methanogenesis in terrestrial wetlands. Wetlands represent the dominant non-anthropogenic source of atmospheric methane today (Denman et al., 2007; O'Connor et al., 2010; Bridgham et al., 2013), and wetland methane emissions should respond significantly and rapidly to increases in global temperature (increases of up to ~20% per 1ºC) and precipitation (8% increase per 20% increase in precipitation) (Walter et al., 2001). Furthermore, recent reports of terrestrial methane budgets and distributions are painting a much clearer picture of its important role in the global carbon cycle (Wik et al., 2016; Holgerson et al., 2016; Tian et al.,

2016). Past releases of terrestrial carbon stocks have also been identified to be a causal mechanism behind extreme global warming events during the early Cenozoic (e.g., Pancost et al., 2007; DeConto et al., 2012). The Early Jurassic is considered to be a greenhouse time interval with warm and humid climates (Korte et al., 2015), constituting ideal conditions for the formation of extensive wetlands, such as peatlands and swamps. Therefore, we posit that global warming and the enhanced hydrological cycle resulting from the eruption of the Karoo-Ferrar LIP led to a positive feedback — increased methane emission rates from wetland environments — which led to continued warming. A similar feedback scenario has been proposed for the PETM (Pancost et al., 2007).

Further, we propose that the small-scale CIEs that are present in the Toarcian carbon-isotope records could be linked to astronomically paced changes in the climate system, which affected rates of wetland methanogenesis (e.g., changes in precipitation patterns, solar insolation, etc.), rather than releases from marine methane clathrate reservoirs on similar timescales. However, it is important to point out that terrestrial methanogenesis and the destabilization of methane clathrates would operate on similar timescales and respond to warming in a similar fashion, so it is likely that these two drivers could have both contributed to the shorter-term perturbations in the global carbon cycle during the Toarcian. An alternative scenario, in which pulses of volcanogenic CO_2 or thermogenic methane drove these small-scale CIEs, is possible. Eruptions of the Karoo-Ferrar large igneous province during the late Pliensbachian and Toarcian have been linked to global marine extinction events (Caruthers et al., 2013). However, similar to marine clathrates, the amount of carbon necessary from these sources on such short timescales is difficult to reconcile (Beerling and Brentnall, 2007).

Numerical models suggest the release of 6,000 to 9,000 Gt carbon derived from biogenic

methane ($\delta^{13}C$ of -60‰) over 220 thousand years can reproduce the overall magnitude and shape of a T-OAE CIE ranging from -3 to -5‰ (Beerling and Brentnall, 2007). Based on a more recent 100-kyr estimation (Sell et al., 2014) for the duration of the falling limb of the CIE, an increase in global average air temperature of 4.5ºC (Dera and Donnadieu, 2012), an estimated range of modern wetland methanogenesis rates, 0.0691 – 0.210 Gt C/year (as summarized by Denman et al., 2007; O'Connor et al., 2010; Bridgham et al., 2013), and the response of methanogenesis rates to temperature (~20% increase per 1°C increase based on both empirical and modeling studies) (Walter et al., 2001; Christensen et al., 2003), we calculate an approximate two-fold (~2x) increase in terrestrial methanogenesis rates (~0.131 – 0.399 Gt C/year) or an additional 0.062 – 0.189 Gt C/year across the T-OAE. Overall this warming alone has the potential to release an additional ~6,620 – 18,869 Gt C (8,307 – 25,200 Gt CH_4) from wetlands. These magnitudes represent values that are similar or much larger than what is necessary to cause and sustain the CIE (Beerling and Brentnall, 2007).

If we consider the full range of air and sea surface temperature estimates for the T-OAE (Bailey et al., 2003; Rosales et al., 2004; Suan et al., 2008; Dera et al., 2009; Gómez et al., 2015; Korte et al., 2015) (see Table S1) combined with the full range of estimates for modern methanogenesis rates (Denman et al., 2007; O'Connor et al., 2010; Bridgham et al., 2013), then an additional 3,455 – 33,544 Gt C could have been released to the atmosphere. Note that there would be a significant latitudinal gradient in warming (Dera and Donnadieu, 2012) (see Table S1) that will affect the regional methane fluxes. Proxy reconstructions and modeling of sea surface and air temperature changes during the T-OAE suggest increases that range from 3 to > 10ºC (Bailey et al., 2003; Rosales et al., 2004; Suan et al., 2008; Dera et al., 2009; Dera and Donnadieu, 2012; Gómez et al., 2015; Korte et al., 2015) that are highly dependent on

paleolatitude; thus, there is potential for larger terrestrial methane releases based on regional temperature changes (refer to SI Table 2). A recent modeling study suggests that there was a global increase in precipitation of 9 cm/year during the T-OAE, reaching up to 10 – 20 cm/year in high latitudes and equatorial regions of Gondwana and the Tethys (Dera and Donnadieu, 2012). During methanogenesis, organic carbon is decomposed, and its renewal rate may have limited the total methanogenesis rate on longer timescales, which could have dampened the amount of methane released to the atmosphere. However, even fractions of the amounts calculated here would release enough carbon to the atmosphere to cause and sustain the CIE, and produce significant changes in global temperatures. Although several processes govern methanogenesis rates in wetlands (Walter and Heimann, 2000; Walter et al., 2001), e.g. precipitation rates (which appear to have also significantly increased during the T-OAE (Cohen et al., 2004; Dera and Donnadieu, 2012), here we only attempt to show temperature effects.

Importantly, combining carbon fluxes from other plausible sources (mantle CO_2, thermogenic CH_4, and clathrate CH_4) diminishes the amount needed from any individual source; less wetland-derived methane would be necessary when the other drivers are involved. As multiple drivers are likely responsible for the T-OAE CIE and global warming, we suggest that methane release from wetlands can provide a plausible and important feedback flux that fills outstanding deficiencies of Toarcian carbon cycle budgets. The flux of wetland carbon should be considered in future refinements of Toarcian carbon cycle models; furthermore, wetland-derived methane should be considered as a driver of rapid carbon cycle perturbations during climatic warm periods in the geologic record (following the proliferation of land plants).

6. Conclusions

The Toarcian CIE and the high-frequency fluctuations within it have now been documented from multiple oceanic basins spanning the globe. This observation is consistent with a global perturbation to the carbon cycle triggered by volcanism associated with the emplacement of the Karoo-Ferrar LIP and escalated by biogeochemical feedbacks. A better understanding of the T-OAE record may serve to inform models of other events triggered by rapid injections of greenhouse gases, such as the PETM. While these two events were separated by roughly 130 million years and had significantly different boundary conditions, the resulting environmental change and ecological deterioration were broadly similar. Additionally, the combination of increased temperature, ocean acidification, and oxygen depletion in the ocean during these events led to greater rates of turnover in the marine biosphere. As our planet experiences another significant perturbation to the global carbon cycle and climatic warming, the record of environmental change recorded during these geologic events represent an invaluable archive for models of future climate and oceanographic change.

Acknowledgements

This work is dedicated to our late friend and colleague Russell Hall, whose work in the Jurassic of Canada stimulated this study. A grant to BCG from the NSF (EAR-1324752) funded this work. TRT would also like to thank the Geological Society of America, Society for Sedimentary Geology, and Virginia Tech Department of Geosciences graduate student grant programs for funding. RCM would like to thank a UT-Austin seed grant for funding fieldwork. Thanks to Angela Gerhardt, Selva Marroquín, and Joshua Lively for their help in the field work portion of the study as well as the staff at the RTMP for fossil curation. This is Natural Resources Canada Contribution No. ESS 20150492.

7. References

Al-Suwaidi, A.H., Angelozzi, G.N., Baudin, F., Damborenea, S.E. Hesselbo, S.P., Jenkyns, H.C., Manceñido, M.O., and Riccardi, A.C., 2010, First record of the Early Toarcian Oceanic Anoxic Event from the Southern Hemisphere, Neuquén Basin. Arg. J. Geol. Soc. [Lon.] 167, 633–636.

Al-Suwaidi, A.H., Hesselbo, S.P., Damborenea, S.E., Manceñido, M.O., Riccardi, A.C., Angelozzi, G.N., and Baudin, F., 2016, The Toarcian Oceanic Anoxic Event (Early Jurassic) in the Neuquén Basin, Argentina: A Reassessment of Age and Carbon Isotope Stratigraphy. J. Geol. 124, 000–000.

Asgar–Deen, M., Hall, R., Craig, J., and Riediger, C., 2003, New biostratigraphic data from the Lower Jurassic Fernie Formation in the subsurface of west-central Alberta and their stratigraphic implications. Can. J. Earth Sci. 40, 45–63.

Bailey, T.R., Rosenthal, Y., McArthur, JM, van de Schootbrugge, B., and Thirlwall M.F., 2003, Paleoceanographic changes of the Late Pliensbachian-Early Toarcian interval, a possible link to the genesis of an Oceanic Anoxic Event. Earth Planet. Sci. Lett. 212, 307–320.

Beerling, D.J., and Brentnall, S.J., 2007, Numerical evaluation of mechanisms driving Early Jurassic changes in global carbon cycling. Geology 5, 247–250.

Bond, D.P.G., and Wignall, P.B., 2014, Large igneous provinces and mass extinctions: An update *in* Keller, G., and Kerr, A.C., eds., Volcanism, Impacts and Mass Extinction: causes and effects. Geol. Soc. Amer. Spec. Paper 505, 29–55.

Boulila, S., Galbrum, B., Huret, E., Hinnov, L.A., Rouget, I., Gardin, S., and Bartolini, A., 2014, Astronomical calibration of the Toarcian Stage: Implications for sequence stratigraphy

and duration of the early Toarcian OAE. Earth Planet. Sci. Lett. 386, 98–111.

Bridgham, S.D., Cadillo-Quiroz, H., Keller, J.K., and Zhuang, Q., 2013, Methane emissions from wetlands: biogeochemical, microbial, and modeling perspectives from local to global scales. Glob. Change Biol. 19, 1325–1346.

Burgess, S.D., Bowring, S.A., Fleming, T.H., and Elliot, D.H., 2015, High-precision geochronology links the Ferrar large igneous province with early-Jurassic ocean anoxia and biotic crisis. Earth Planet. Sci. Lett. 415, 90–99.

Caruthers, A.H., Gröcke, D.R., and Smith, P.L., 2011, The significance of an Early Jurassic (Toarcian), carbon-isotope excursion in Haida Gwaii (Queen Charlotte Islands), British Columbia, Canada. Earth Planet. Sci. Lett. 307, 19–26.

Caruthers, A.H., Smith, P.L., and Gröcke, D.R., 2013, The Pliensbachian-Toarcian (Early Jurassic) extinction, a global multi-phased event. Palaeogeo. Palaeoclim. Palaeoecol. 386, 104–118.

Caruthers, A., Smith, P.L., and Gröcke, D.R., 2014, The Pliensbachian-Toarcian (Early Jurassic) extinction: a North American perspective, *in* Keller, G., and Kerr, A.C., eds., Volcanism, Impacts and Mass Extinction: causes and effects. Geol. Soc. Amer. Spec. Paper 505, 225–243.

Christensen, T.R., Ekberg, A., Ström, L., and Mastepanov, M., 2003, Factors controlling large scale variations in methane emissions from wetlands. Geo. Res. Lett. 30, 1414.

Cohen, A.S., Coe, A.L., Harding, S.M., and Schwark, L., 2004, Osmium isotope evidence for the regulation of atmospheric CO_2 by continental weathering. Geology 32, 157–160.

Cohen, A.S., Coe, A.L., and Kemp, D.B., 2007, The Late Palaeocene—Early Eocene and

Toarcian (Early Jurassic) carbon isotope excursions: a comparison of their time scales, associated environmental changes, causes and consequences. J. Geol. Soc., London 164, 1093–1108.

Danise, S., Twitchett, R.J., and Little, C.T.S., 2015, Environmental controls on Jurassic marine ecosystems during global warming. Geology 43, 263–266.

DeConto, R.M., Galeotti, S., Pagani, M., Tracy, D., Schaefer, K., Zhang, T., Pollard, D., and Beerling, D.J., 2012, Past extreme warming events linked to massive carbon release from thawing permafrost. Nature 484, 87–91.

Denman, K., et al., 2007, Couplings between changes in the climate system and biogeochemistry, Climate Change. The Physical Science Basis *in* Solomon, S., et al., eds., Contribution of Working Group I to the Fourth Assessment Report of the Intergovernmental Panel on Climate Change. (Cambridge University Press, Cambridge, U.K.), 499–587.

Dera, G.D., Pucéat, E., Pellenard, P., Neige, P., Delsate, D., Joachimski, M.M., Reisberg, L., and Martinez, M., 2009, Water mass exchange and variations in seawater temperature in the NW Tethys during the Early Jurassic: Evidence from neodymium and oxygen isotopes of fish teeth and belemnites. Earth Planet. Sci. Lett. 286, 198–207.

Dera, G.D., and Donnadieu, Y., 2012, Modeling evidence for global warming, Arctic seawater freshening, and sluggish ocean circulation during the Early Toarcian anoxic event. Paleoceanography 27, PA2211.

Dickens, G.R., O'Neil, J.R., Rea, D.K., and Owen, R.M., 1995, Dissociation of oceanic methane

hydrate as a cause of the carbon isotope excursion at the end of the Paleocene. Paleoceanography 10, 965–971.

Frebold, H., 1957, The Jurassic Fernie Group in the Canadian Rocky Mountains and foothills. Geol. Surv. Can. Mem. 287, 197 pp.

French, K.L., Sepúlveda, J., Trabucho-Alexandre, J., Gröcke, D.R., and Summons, R.E., 2014, Organic geochemistry of the early Toarcian oceanic anoxic event in Hawsker Bottoms, Yorkshire, England. Earth Planet. Sci. Lett. 390, 116–127.

Gómez, J.J., Comas-Rengifo, M.J., and Goy, A., 2015, Palaeoclimatic oscillations in the Pliensbachian (Lower Jurassic) of the Asturian Basin (Northern Spain). Clim. Past Discuss. 11, 4039–4076.

Gröcke, D.R., Rimmer, S.M., Yoksoulian, L.E., Cairncross, B., Harilaos, T., and van Hunen, J., 2006, No evidence for thermogenic methane release in coal from the Karoo-Ferrar large igneous province. Earth Planet. Sci. Lett. 277, 204–212.

Gröcke, D.R., Hori, R.S., Trabucho-Alexandre, J., Kemp, D.B., and Schwark, L., 2011, An open record of the Toarcian oceanic anoxic event. Sol. Earth Discuss. 2, 245–257.

Guex, J., Bartolini, A., Spangenberg, J., Vicente, J.-C., and Schaltegger, U., 2012, Ammonoid multi-extinction crises during the Late Pliensbachian – Toarcian and carbon cycle instabilities. Sol. Earth Discuss. 4, 1205–1228.

Hall, R.L., 1984, Lithostratigraphy and biostratigraphy of the Fernie Formation (Jurassic) in the southern Canadian Rocky Mountains, *in* Stott, D.F., and Glass, D.J., eds., The Mesozoic of Middle North America. Can. Soc. Petr. Geol. Mem. 9, 233–247.

Hall R.L., Poulton, T.P., and Monger, J.W.H., 1998, Chapter 2 Field Trip A1: Calgary-Vancouver, *in* Smith, P.L., ed., Field Guide for the Fifth International Symposium on the Jurassic System, Vancouver, Jurassic Subcommission of the Stratigraphic Commission of the International Union of Geological Sciences, Vancouver, 29–61.

Harries, P., and Little, C.T.S., 1999, The early Toarcian (Early Jurassic) and Cenomanian-Turonian Late Cretaceous, mass extinctions, similarities and contrasts. Palaeogeo. Palaeoclim. Palaeoecol. 154, 39–66.

Hermoso, M., Le Callonnec, L., Minoletti, F., Renard, M., and Hesselbo, S.P., 2009, Expression of the Early Toarcian negative carbon-isotope excursion in separated carbonate microfractions (Jurassic, Paris Basin). Earth Planet. Sci. Lett. 277, 194–203.

Hermoso, M., Minoletti, F., Rickaby, R.E.M., Hesselbo, S.P., Baudin, F., and Jenkyns, H.C., 2012, Dynamics of a stepped carbon-isotope excursion: Ultra high-resolution study of Early Toarcian environmental change. Earth Planet. Sci. Lett. 319-320, 45–54.

Hesselbo, S.P., Gröcke, D.R., Jenkyns, H.C., Bjerrum, C.J., Farrimond, P., Morgans Bell, H.S., and Green, O.R., 2000, Massive dissociation of gas hydrate during a Jurassic oceanic anoxic event. Nature 406, 392–395.

Hesselbo, S.P., Jenkyns, H.C., Duarte, L.V., and Oliveira, L.C.V., 2007, Carbon-isotope record of the Early Jurassic (Toarcian) Oceanic Anoxic Event from fossil wood and marine carbonate Lusitanian Basin, Portugal. Earth Planet. Sci. Lett. 253, 455–470.

Hesselbo, S.P., and Pieńkowski, G., 2011, Stepwise atmospheric carbon-isotope excursion during the Toarcian Oceanic Anoxic Event (Early Jurassic, Polish Basin). Earth Planet.

Sci. Lett. 301, 365–372.

Higgins, J.A., and Schrag, D.P., 2006, Beyond methane: Towards a theory for the Paleocene-Eocene Thermal Maximum. Earth Planet. Sci. Lett. 245, 523–537.

Holgerson, M.A., and Raymond, P.A., 2016, Large contribution to inland water CO_2 and CH_4 emissions from very small ponds. Nature Geosci. 9, 222–226.

Howarth, M.K., 1962, The Jet Rock Series and the Alum Shale Series of the Yorkshire Coast. Proc. York. Geol. Soc. 33, 381–422.

Howarth, M.K., 1978, The stratigraphy and ammonite fauna of the Upper Lias of Northamptonshire. Bull. Brit. Mus. (Nat. Hist.) 29, 235–288.

Howarth, M.K., 1992, The ammonite family Hildoceratidae in the Lower Jurassic of Britain. Mono. Palaeont. Soc. 145, 1–200.

Izumi, K., Miyaji, T., and Tanabe, K., 2012, Early Toarcian (Early Jurassic) oceanic anoxic event recorded in the shelf deposits in the northwestern Panthalassa: Evidence from the Nishinakayama Formation in the Toyora area, west Japan. Palaeogeo. Palaeoclim. Palaeoecol. 315-316, 100–108.

Jakobs, G.K., Smith, P.L., and Tipper H.W., 1994, An ammonite zonation for the Toarcian (Lower Jurassic) of the North American Cordillera. Can. J. Earth Sci. 31, 919–942.

Jakobs, G.K., 1997, Toarcian (Early Jurassic) Ammonoids from Western North America. Geol. Surv. Can. Bull. 428, 1–137.

Jenkyns, H.C., 1988, The early Toarcian (Jurassic) anoxic event: Stratigraphic, sedimentary, and

geochemical evidence. Am. J. Sci. 288, 101–151.

Jenkyns, H.C., and Clayton, C.J., 1997, Lower Jurassic epicontinental carbonates and mudstones from England and Wales: chemostratigraphic signals and the early Toarcian anoxic event. Sedimentology 44, 687–706.

Kemp D.B., Coe, A.L., Cohen, A.S., and Schwark, L., 2005, Astronomical pacing of methane release in the Early Jurassic period. Nature 437, 396–399.

Kemp, D.B., and Izumi, K., 2014, Multiproxy geochemical analysis of a Panthalassic margin record of the Early Toarcian oceanic anoxic event (Toyora area, Japan). Palaeogeo. Palaeoclim. Palaeoecol. 414, 332–341.

Korte, C., Hesselbo, S.P., Ullmann, C.V., Dietl, G., Ruhl, M., Schweigert, G., and Thibault, N., 2015, Jurassic climate mode governed by ocean gateway. Nature Comm. 6, 10015.

McElwain, J.C., Wade-Murphy, J., and Hesselbo, S.P, 2005, Changes in carbon dioxide during an oceanic anoxic event linked to intrusion into Gondwana coals. Nature 435, 479–482.

Milkov, A.V., 2004, Global estimates of hydrate-bound gas in marine sediments: how much is really out there? Earth-Sci. Rev. 66, 183–197.

O'Connor, F.M., et al., 2010, Possible role of wetlands, permafrost, and methane hydrates in the methane cycle under future climate change: A review. Rev. Geophys. 48, RG4005.

Pálfy, J., and Smith, P.L., 2000, Synchrony between Early Jurassic extinction, oceanic anoxic event, and the Karoo-Ferrar flood basalt volcanism. Geology 28, 747–750.

Panchuk, K., Ridgwell, A., and Kump, L.R., 2008, Sedimentary response to Paleocene-Eocene

Thermal Maximum carbon release, A model-data comparison. Geology 36, 315–318.

Pancost, R.D., Steart, D.S., Handley, L., Collinson, M.E., Hooker, J.J., Scott, A.C., Grassineau, N.V., and Glasspool, I.J., 2007, Increased terrestrial methane cycling at the Palaeocene-Eocene thermal Maximum. Nature 449, 332–335.

Poulton T.P., and Hall, R.L. 1993, Western Interior Canada. The Jurassic of the Circum-Pacific, *in* Westermann, G.E.G., ed., (Cambridge University Press), 38–44.

Rosales, I., Quesada, S., and Robles, S., 2004, Paleotemperature variations of Early Jurassic seawater recorded in the geochemical trends of belemnites from the Basque-Cantabrian basin, northern Spain. Palaeogeo. Palaeoclim. Palaeoecol. 203, 253–275.

Sandoval, J., Bill, M., Aguado, R., O'Dogherty, L., Rivas, P., Morard, A., and Guex, J., 2012, The Toarcian in the Subbetic basin (southern Spain): Bio-events (ammonite and calcareous nannofossils) and carbon-isotope stratigraphy, Palaeogeo. Palaeoclim. Palaeoecol. 342-343, 40–63.

Schouten, S., van Kaam-Peters, H.M.E., Rijpstra, W.I.C., Schoell, M., and Damsté, J.S.S., 2000, Effects of an oceanic anoxic event on the stable carbon isotopic composition of early Toarcian carbon. Am. J. Sci. 300, 1–22.

Scotese, C.R., 2001, Atlas of Earth History. PALEOMAP Project, Arlington, Texas.

Sell, B., Ovtcharoca, M., Bartolini, A., Jourdan, F., Spangenberg, J.E., Vicente, J.-C., and Schaltegger, U., 2014, Evaluating the temporal link between the Karoo LIP and climatic—biologic events of the Toarcian Stage with high-precision U-Pb geochronology. Earth Planet. Sci. Lett. 408, 48–56.

Smith P.L., and Tipper H.W., 1996, Pliensbachian (Lower Jurassic) Ammonites of the Queen Charlotte Islands, British Columbia. Bull. Am. Paleont. 108, 1–122.

Storey, M., Duncan, R.A., and Swisher, C.C. III, 2007 Paleocene-Eocene thermal-maximum and the opening of the Northeast Atlantic. Science 316, 587–589.

Suan, G., Mattioli, E., Pittet, B., Mailliot, S., and Lécuyer, C., 2008, Evidence for major environmental perturbation prior to and during the Toarcian (Early Jurassic) oceanic anoxic event from the Lusitanian basin, Portugal. Paleoceanography 23, PA1202.

Suan, G., et al. 2011, Polar record of Early Jurassic massive carbon injection. Earth Planet. Sci. Lett. 312, 102–113.

Suan, G., van de Schootbrugge, B., Adatte, T., Fiebig, J., and Oschmann, W., 2015, Calibrating the magnitude of the Toarcian carbon cycle perturbation. Paleoceanography 30, 495–509.

Svensen, H., Planke, S., Chevallier, L., Malthe-Sørenssen, A., Corfu, F., and Jamtveit, B., 2007, Hydrothermal venting of greenhouse gases triggering Early Jurassic global warming. Earth Planet. Sci. Lett. 256, 554–566.

Svensen, H., Planke, S., Malthe-Sørenssen, A., Jamtveit, B., Myklebust, R., Rasmussen Eidem, T., and Rey, S.S., 2004 Release of methane from a volcanic basin as a mechanism for initial Eocene global warming. Nature 429, 542–545.

Tian, H., et al., 2016, The terrestrial biosphere as a net source of greenhouse gases to the atmosphere. Nature 531, 225–228.

Trabucho-Alexandre, J., 2014, More gaps than shale: erosion of mud and its effect on preserved geochemical and palaeobiological signals, *in* Smith, D.G., Bailey, R.J., Burgess, P.M., Fraser, and A.J., eds., Strata and Time: Probing the Gaps in Our Understanding. Geol. Soc. Lon. Spec. Pub. 404, 251–270.

van Breugal, Y., Baas, M., Schouten, S., Mattioli, E., and Damsté, J.S.S., 2006, Isorenieratane record in black shales from the Paris Basin, France: Constraints on recycling of respired CO_2 as a mechanism for negative carbon isotope shifts during the Toarcian oceanic anoxic event. Paleoceanography 21, PA4220.

Walter, B.P., and Heimann, M., 2000, A process-based, climate-sensitive model to derive methane emissions form natural wetlands: Application to five wetland sites, sensitivity to model parameters, and climate. Glob. Biogeo. Cyc. 14, 745–765.

Walter, B.P., Heimann, M., and Matthews, E., 2001, Modeling Modern Methane Emissions from Natural Wetlands 2. Interannual Variations 1982-1993. J. Geophys. Res. 106, D24, 34,207–34,219.

Wignall, P.B., McArthur, J.M., Little, C.T.S., and Hallam, A., 2006, Methane release in the Early Jurassic period: Comment. Nature 442, 441.

Wik, M., Varner, R.K., Anthony, K.W., MacIntyre, S, and Bastviken, D., 2016, Climate-sensitive northern lakes and ponds are critical components of methane release. Nature Geosci. 9, 99–105.

8. Table

Table 1. Potential masses of carbon released during the Toarcian carbon isotope excursion.

Driver	$\delta^{13}C$ (‰)	Mass (Gt C)	Source of estimate	Reference
Wetland methanogenesis	-60	6,220 – 18,869*	Model predictions	*This study*
Biogenic methane clathrate	-60	>6,000	Model requirements	Beerling and Brentnall (2007)
Thermogenic methane	-35	2,600 – 4,400	Proxy data – Stomatal index	McElwain et al. (2005)
Thermogenic methane	-29 to -24	491 – 7,487	Proxy data – Organic carbon loss	Svensen et al. (2007)
Mixture	-13.6 to -8.2	>40,000**	Model predictions	Brazier et al. (2015)
Mantle CO_2	-5	15,340 – 24,750	Model requirements	Beerling and Brentnall (2007)

*This calculation is based on a global 4.5ºC temperature increase (Dera and Donnadieu, 2012).
**This calculation is based on calcium isotope changes (Brazier et al., 2015).

9. Figures

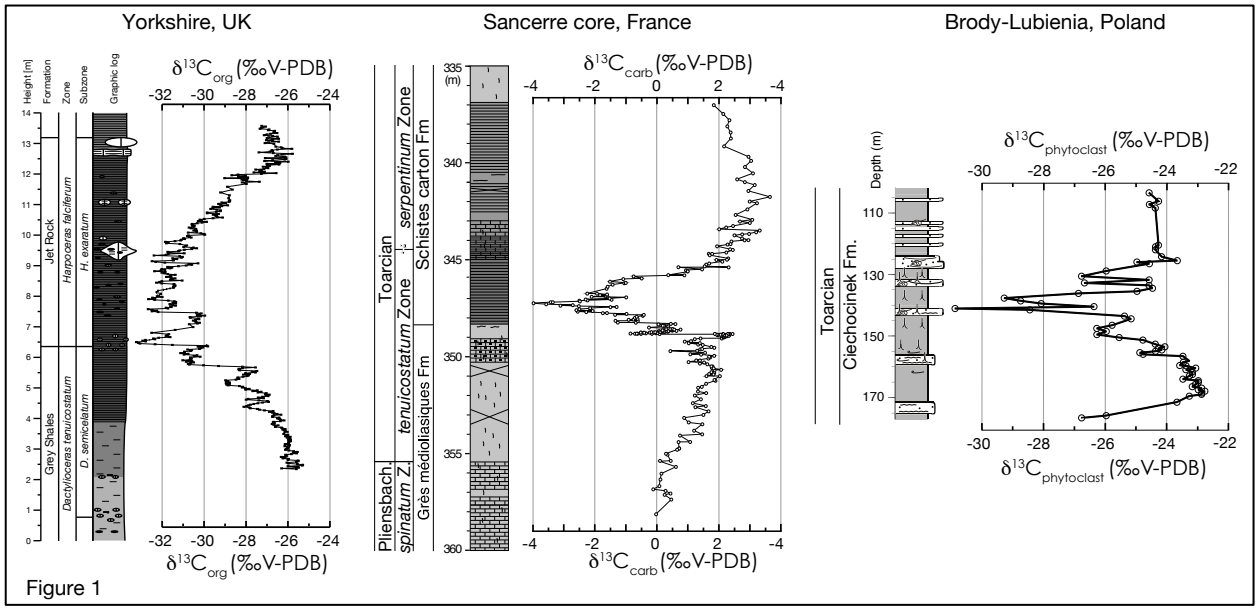

Figure 1. High-resolution $\delta^{13}C_{org}$, $\delta^{13}C_{carb}$, and $\delta^{13}C_{phytoclast}$ records across Toarcian carbon isotope excursion (CIE). These records are from Yorkshire, England, the Sancerre-Couy borehole, France, and Brody-Lubienia, Poland respectively (modified from Hesselbo et al., 2000; Kemp et al., 2005; Hermoso et al., 2009, 2012; Hesselbo and Pieńkowski, 2011). Note the small-scale CIEs on the falling limb of the overall CIE. $\delta^{13}C_{phytoclast}$ values represent wood fragments, cuticle, and spores from terrestrial locations.

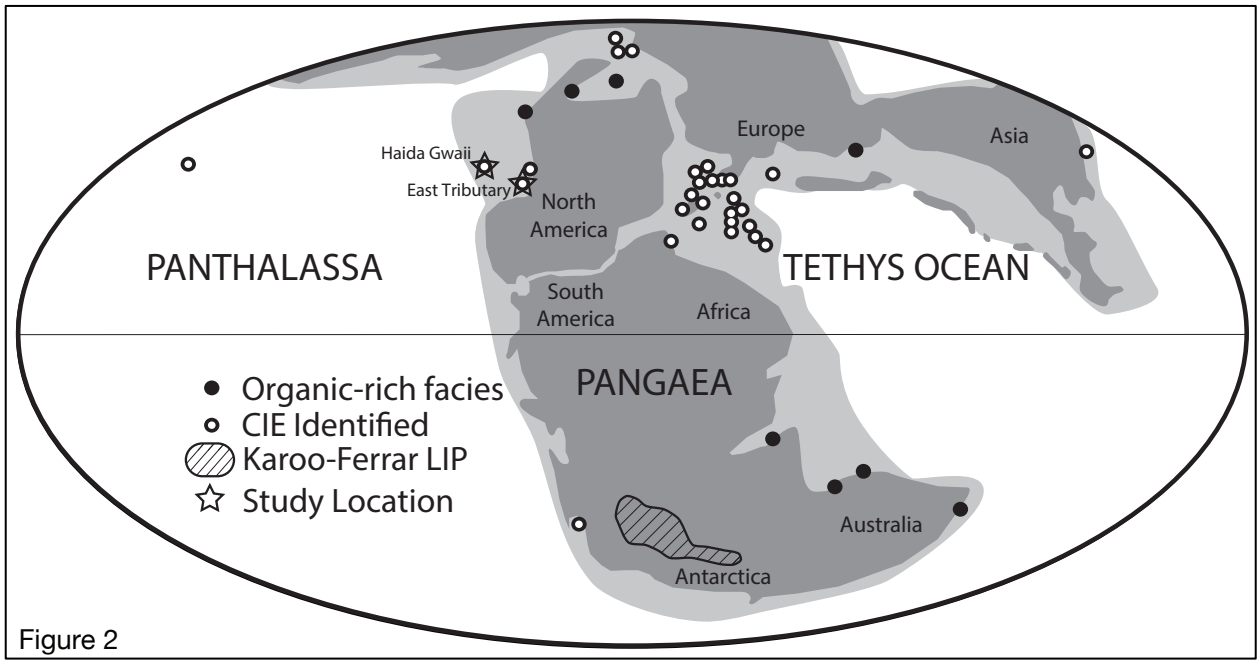

Figure 2. Global paleogeography of the Early Toarcian (modified from Scotese, 2001). Black circles represent presence of Toarcian organic-rich facies (updated from Jenkyns, 1988; additional references provided in Table S2). Open circles represent locations where Toarcian CIE has been recognized. Hatched outline in southern Africa and Antarctica represents location and extent of Karoo-Ferrar large igneous province. Dark grey represents landmasses, light grey represents shallow seas, and white represents open oceans. Note some circles represent multiple localities in close proximity.

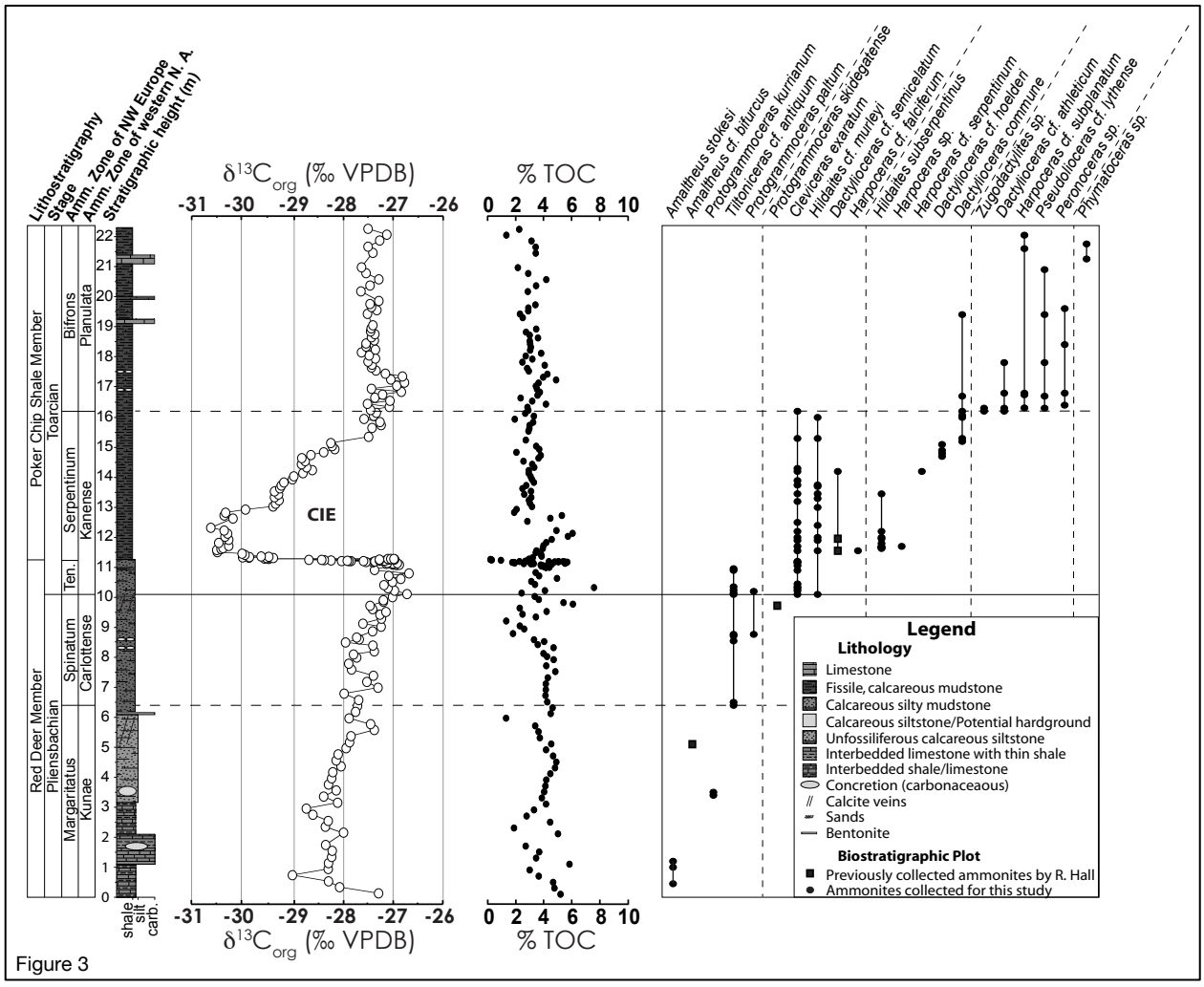

Figure 3

Figure 3. Chemostratigraphy and ammonite biostratigraphy of East Tributary of Bighorn Creek Alberta. $\delta^{13}C_{org}$ = organic carbon isotopic compositions; TOC = total organic carbon. Lithostratigraphic members of the Fernie Formation, stages of the Jurassic, and ammonite zonations for both northwestern Europe and western North American shown to the left of the stratigraphic column (refer to the supplementary material for details of the placement of these zonations). Ammonite zone boundaries are noted across the data plots with dashed lines. The Pliensbachian-Toarcian stage boundary is marked with a solid line. Ten. = Tenuicostatum.

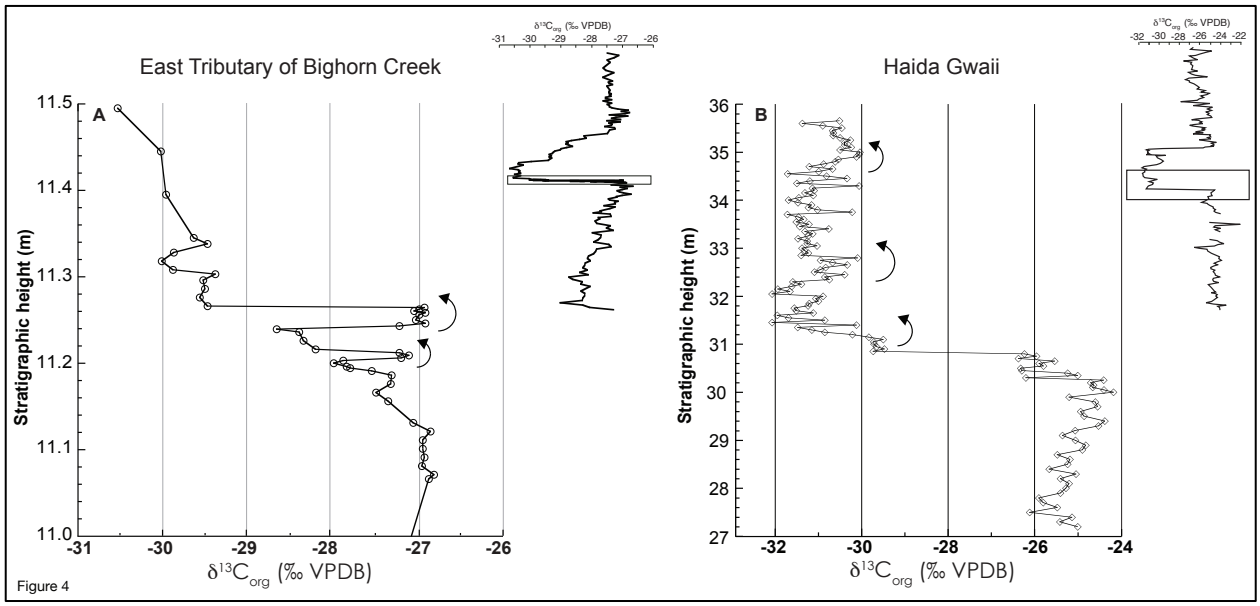

Figure 4: High-resolution $\delta^{13}C_{org}$ records of the T-OAE CIE from western North America. **(A)** East Tributary of Bighorn Creek, AB, and **(B)** Haida Gwaii (formerly Queen Charlotte Islands), BC. In comparison to some of the European records (Fig. 1), it is clear that both sections contain a less complete record of the overall falling limb of the Toarcian CIE. Despite this incompleteness, both sections contain several small-scale CIEs (arrows). At East Tributary, these are expressed as oscillations on the falling limb of the overall CIE likely correlative to those seen at the beginning of the CIE in Europe. At Haida Gwaii, small-scale CIEs that occur at the nadir of the overall CIE are better represented.

10. Supplemental Information:

High-resolution carbon isotope records of the Toarcian Oceanic Anoxic Event (Early Jurassic) from North America and implications for the global drivers of the Toarcian carbon cycle

(T.R. Them II, B.C. Gill, A.H. Caruthers, D.R. Gröcke, E.T. Tulsky, R.C. Martindale, T.P. Poulton, P.L. Smith)

Supplemental Information

Table S1. Paleotemperature reconstructions during the Toarcian OAE.

Location	Technique	Temp. change (ºC)	Material	Reference
UK, Germany	$\delta^{18}O$ and Mg/Ca	6.5*	Belemnite	Bailey et al. (2003)
Spain	$\delta^{18}O$ and Mg/Ca	6.5*	Belemnite	Rosales et al. (2004)
Denmark	Modeled relationship between pCO_2 and temperature	2.5 to 4.5†	Fossil leaves (stomatal index) and model	McElwain et al. (2005)
Portugal	$\delta^{18}O$	4*	Brachiopod	Suan et al. (2008)
Belgium, France, Luxembourg	$\delta^{18}O$	4*	Belemnite, fish teeth	Dera et al. (2009)
Asturian Basin, Northern Spain	$\delta^{18}O$	up to 8*	Belemnite	Gómez et al. (2015)
N/A	Moderate complexity GCM	4.5† (>10 at the poles) (5 at mid-latitudes) (3 degrees at tropics)	Model results	Dera and Donnadieu (2012)

*Sea surface temperature change

† Global mean air temperature change

Table S2. Locations of reported Toarcian CIE.

Location	Reference(s)
Alberta	*This study*
Argentina	Al-Suwaidi et al. (2011, 2016)
British Columbia	Caruthers et al. (2011, 2014); this study
Bulgaria	Metodiev et al. (2013)
Croatia	Sabatino et al. (2013)
Denmark	Hesselbo et al. (2000)
France	Van Breugal et al. (2006); Hermoso et al. (2009); Léonide et al. (2012)
Germany	Röhl et al. (2001); Suan et al. (2015)
Greece	Kafousia et al. (2011, 2014)
Italy	Jenkyns et al. (2001); Woodfine et al. (2008); Sabatino et al. (2009)
Japan	Gröcke et al. (2011); Izumi et al. (2012); Kemp and Izumi (2014)
Morocco	Bodin et al. (2010)
Netherlands	Trabucho-Alexandre et al. (2012)
Poland	Hesselbo and Pieńkowski (2011)
Portugal	Duarte et al. (2007); Hesselbo et al. (2007); Pittet et al. (2014)
Russia	Suan et al. (2011)
Spain	Gómez et al. (2008); Gómez and Arias (2010); Reolid et al. (2014)
United Kingdom	Jenkyns and Clayton (1997); Hesselbo et al. (2000); Kemp et al. (2005)

References Cited in Supplementary Material

Al-Suwaidi, A.H., Angelozzi, G.N., Baudin, F., Damborenea, S.E. Hesselbo, S.P., Jenkyns, H.C., Manceñido, M.O., and Riccardi, A.C., 2010, First record of the Early Toarcian Oceanic Anoxic Event from the Southern Hemisphere, Neuquén Basin. Arg. J. Geol. Soc. [Lon.] 167, 633–636.

Al-Suwaidi, A.H., Hesselbo, S.P., Damborenea, S.E., Manceñido, M.O., Riccardi, A.C., Angelozzi, G.N., and Baudin, F., 2016, The Toarcian Oceanic Anoxic Event (Early Jurassic) in the Neuquén Basin, Argentina: A Reassessment of Age and Carbon Isotope Stratigraphy. J. Geol. 124, 000–000.

Bailey, T.R., Rosenthal, Y., McArthur, JM, van de Schootbrugge, B., and Thirlwall M.F., 2003, Paleoceanographic changes of the Late Pliensbachian-Early Toarcian interval, a possible link to the genesis of an Oceanic Anoxic Event. Earth Planet. Sci. Lett. 212, 307–320.

Beerling, D.J., and Brentnall, S.J., 2007, Numerical evaluation of mechanisms driving Early Jurassic changes in global carbon cycling. Geology 5, 247–250.

Bodin, S., Mattioli, E., Fröhlich, S., Marshall, J.D., Boutib, L., Lahsini, S., and Redfern, J., 2010, Toarcian carbon isotope shifts and nutrient changes from the Northern margin Gondwana (High Atlas, Morocco, Jurassic): Palaeoenvironmental implications. Palaeogeography, Palaeoclimatology, Palaeoecology, 297, 377–390.

Brazier, J.-M., Suan, G., Tacail, T., Simon, L., Martin, J.E., Mattioli, E., and Balter, V., 2015 Calcium isotope evidence for dramatic increase in continental weathering during the Toarcian oceanic anoxic event (Early Jurassic). Earth and Planetary Science Letters, v. 411, p. 164-176.

Caruthers, A.H., Gröcke, D.R., and Smith, P.L., 2011, The significance of an Early Jurassic (Toarcian), carbon-isotope excursion in Haida Gwaii (Queen Charlotte Islands), British Columbia, Canada. Earth Planet. Sci. Lett. 307, 19–26.

Caruthers, A., Smith, P.L., and Gröcke, D.R., 2014, The Pliensbachian-Toarcian (Early Jurassic) extinction: a North American perspective, *in* Keller, G., and Kerr, A.C., eds., Volcanism, Impacts and Mass Extinction: causes and effects. Geol. Soc. Amer. Spec. Paper 505, 225–243.

Dera, G.D., Pucéat, E., Pellenard, P., Neige, P., Delsate, D., Joachimski, M.M., Reisberg, L., and Martinez, M., 2009, Water mass exchange and variations in seawater temperature in the NW Tethys during the Early Jurassic: Evidence from neodymium and oxygen isotopes of fish teeth and belemnites. Earth Planet. Sci. Lett. 286, 198–207.

Dera, G.D., and Donnadieu, Y., 2012, Modeling evidence for global warming, Arctic seawater freshening, and sluggish ocean circulation during the Early Toarcian anoxic event. Paleoceanography 27, PA2211.

Duarte, L.V., Oliveira, L.C., and Rodrigues, R., 2007, Carbon isotopes as a sequence stratigraphic tool: examples from the Lower and Middle Toarcian marly limestones of Portugal. Geológico y Minero, 118, 3–18.

Gómez, J.J., Goy, A., and Canales, M.L., 2008, Seawater temperature and carbon isotope variations in belemnites linked to mass extinction during the Toarcian (Early Jurassic) in Central and Northern Spain. Comparisons with other European sections. Palaeogeo. Palaeoclim. Palaeoecol. 258, 28–58.

Gómez, J.J., and Arias, C., 2010, Rapid warming and ostracods mass extinction at the Lower Toarcian (Jurassic) of central Spain. Mar. Micro. 74, 119–135.

Gómez, J.J., Comas-Rengifo, M.J., and Goy, A., 2015, Palaeoclimatic oscillations in the Pliensbachian (Lower Jurassic) of the Asturian Basin (Northern Spain). Clim. Past Discuss. 11, 4039–4076.

Gröcke, D.R., Hori, R.S., Trabucho-Alexandre, J., Kemp, D.B., and Schwark, L., 2011, An open record of the Toarcian oceanic anoxic event. Sol. Earth Discuss. 2, 245–257.

Hermoso, M., Le Callonnec, L., Minoletti, F., Renard, M., and Hesselbo, S.P., 2009, Expression of the Early Toarcian negative carbon-isotope excursion in separated carbonate microfractions (Jurassic, Paris Basin). Earth Planet. Sci. Lett. 277, 194–203.

Hesselbo, S.P., Gröcke, D.R., Jenkyns, H.C., Bjerrum, C.J., Farrimond, P., Morgans Bell, H.S., and Green, O.R., 2000, Massive dissociation of gas hydrate during a Jurassic oceanic anoxic event. Nature 406, 392–395.

Hesselbo, S.P., Jenkyns, H.C., Duarte, L.V., and Oliveira, L.C.V., 2007, Carbon-isotope record of the Early Jurassic (Toarcian) Oceanic Anoxic Event from fossil wood and marine carbonate Lusitanian Basin, Portugal. Earth Planet. Sci. Lett. 253, 455–470.

Hesselbo, S.P., and Pieńkowski, G., 2011, Stepwise atmospheric carbon-isotope excursion during the Toarcian Oceanic Anoxic Event (Early Jurassic, Polish Basin). Earth Planet. Sci. Lett. 301, 365–372.

Izumi, K., Miyaji, T., and Tanabe, K., 2012, Early Toarcian (Early Jurassic) oceanic anoxic event recorded in the shelf deposits in the northwestern Panthalassa: Evidence from the Nishinakayama Formation in the Toyora area, west Japan. Palaeogeo. Palaeoclim. Palaeoecol. 315-316, 100–108.

Jenkyns, H.C., and Clayton, C.J., 1997, Lower Jurassic epicontinental carbonates and mudstones from England and Wales: chemostratigraphic signals and the early Toarcian anoxic event.

Sedimentology 44, 687–706.

Jenkyns, H.C., Gröcke, D.R., and Hesselbo, S.P., 2001, Nitrogen isotope evidence for water mass denitrification during the early Toarcian (Jurassic) oceanic anoxic event. Paleoceanography 16, 593–603.

Kafousia, N., Karakitsios, V., Jenkyns, H.C., and Mattioli, E., 2011, A global event with a regional character: the Early Toarcian Oceanic Anoxic Event in the Pindos Ocean (northern Peloponnese, Greece). Geol. Mag. 148, 619–631.

Kafousia, N., Karakitsios, V., Mattioli. E, Kenjo, S., and Jenkyns H.C., 2014, The Toarcian Oceanic Anoxic Event in the Ionian Zone, Greece. Palaeogeo. Palaeoclim. Palaeoecol. 393, 135–145.

Kemp D.B., Coe, A.L., Cohen, A.S., and Schwark, L., 2005, Astronomical pacing of methane release in the Early Jurassic period. Nature 437, 396–399.

Kemp, D.B., and Izumi, K., 2014, Multiproxy geochemical analysis of a Panthalassic margin record of the Early Toarcian oceanic anoxic event (Toyora area, Japan). Palaeogeo. Palaeoclim. Palaeoecol. 414, 332–341.

Korte, C., Hesselbo, S.P., Ullmann, C.V., Dietl, G., Ruhl, M., Schweigert, G., and Thibault, N., 2015, Jurassic climate mode governed by ocean gateway. Nature Comm. 6, 10015.

Léonide, P., Floquet, M., Durlet, C., Baudin, F., Pittet, B., and Lécuyer, C., 2012, Drowning of a carbonate platform as a precursor state of the Early Toarcian global anoxic event (Southern Province sub-Basin, South-east France). Sedimentology 59, 156-184.

McElwain, J.C., Wade-Murphy, J., and Hesselbo, S.P, 2005, Changes in carbon dioxide during an oceanic anoxic event linked to intrusion into Gondwana coals. Nature 435, 479–482.

Metodiev, L.S., Savov, I.P., Gröcke, D.R., Wignall, P.B., Newton, R.J., Andreeva, P.V., and

Koleva-Rekalova, E.K., 2014, Paleoenvironmental conditions recorded by $^{87}Sr/^{86}Sr$, $\delta^{13}C$, and $\delta^{18}O$ in late Pliensbachian-Toarcian (Jurassic) belemnites from Bulgaria. Palaeogeo. Palaeoclim. Palaeoecol. 409, 98–113.

Pittet, B., Suan, G., Lenoir, F., Duarte, L.V., and Mattioli, E., 2014, Carbon isotope evidence for sedimentary discontinuities in the lower Toarcian of the Lusitanian Basin (Portugal): Sea level change at the onset of the Oceanic Anoxic Event. Sed. Geol. 303, 1–14.

Reolid, M., Emanuela, M., Nieto, L.M., and Rodríguez-Tovar, F., 2014, The Early Toarcian Oceanic Anoxic Event in the External Subbetic (Southiberian Palaeomargin, Westernmost Tethys): Geochemistry, nannofossils and ichnology. Palaeogeo. Palaeoclim. Palaeoecol. 411, 79–94.

Röhl, H.-J., Schmid-Röhl, A., Oschmann, W., Frimmel, A., and Schwark, L., 2001, The Posidonia shale (Lower Toarcian) of SW-Germany: An oxygen-depleted ecosystem controlled by sea level and paleoclimate. Palaeogeo. Palaeoclim. Palaeoecol. 169, 273–299.

Rosales, I., Quesada, S., and Robles, S., 2004, Paleotemperature variations of Early Jurassic seawater recorded in the geochemical trends of belemnites from the Basque-Cantabrian basin, northern Spain. Palaeogeo. Palaeoclim. Palaeoecol. 203, 253–275.

Sabatino, N., Neri, R., Bellanca, A., Jenkyns, H.C., Baudin, F., Parisi, G., and Masetti, D., 2009, Carbon-isotope records of the Early Jurassic (Toarcian) oceanic anoxic event from the Valdorbia (Umbria-Marche Apennines) and Monte Margart (Julian Alps) sections: palaeoceanographic and stratigraphic implications. Sedimentology 56, 1307–1328.

Sabatino, N., Vlahović, I., Jenkyns, H.C., Scopelliti, G., Neri, R., Prtoljan, B., and Velić, I., 2013, Carbon-isotope record and palaeoenvironmental changes during the early Toarcian

oceanic anoxic event in shallow-marine carbonates of the Adriatic Carbonate Platform in Croatia. Geol. Mag. 150, 1085-1102.

Suan, G., Mattioli, E., Pittet, B., Mailliot, S., and Lécuyer, C., 2008, Evidence for major environmental perturbation prior to and during the Toarcian (Early Jurassic) oceanic anoxic event from the Lusitanian basin, Portugal. Paleoceanography 23, PA1202.

Suan, G., et al. 2011, Polar record of Early Jurassic massive carbon injection. Earth Planet. Sci. Lett. 312, 102–113.

Suan, G., van de Schootbrugge, B., Adatte, T., Fiebig, J., and Oschmann, W., 2015, Calibrating the magnitude of the Toarcian carbon cycle perturbation. Paleoceanography 30, 495–509.

Trabucho-Alexandre, J., 2014, More gaps than shale: erosion of mud and its effect on preserved geochemical and palaeobiological signals, *in* Smith, D.G., Bailey, R.J., Burgess, P.M., Fraser, and A.J., eds., Strata and Time: Probing the Gaps in Our Understanding. Geol. Soc. Lon. Spec. Pub. 404, 251–270.

van Breugal, Y., Baas, M., Schouten, S., Mattioli, E., and Damsté, J.S.S., 2006, Isorenieratane record in black shales from the Paris Basin, France: Constraints on recycling of respired CO_2 as a mechanism for negative carbon isotope shifts during the Toarcian oceanic anoxic event. Paleoceanography 21, PA4220.

Woodfine, R.G., Jenkyns, H.C., Sarti, M., Baroncini ,F., and Violante, C., 2008, The response of two Tethyan carbonate platforms to the early Toarcian (Jurassic) oceanic anoxic event: environmental change and differential subsidence. Sedimentology 55, 1011–1028.

Chapter 2

Re-Os evidence for increased chemical weathering during the Toarcian Oceanic Anoxic Event

Theodore R. Them II[1*], Benjamin C. Gill[1], Darren R. Gröcke[2], & David Selby[2]

[1]*Department of Geosciences, Virginia Polytechnic Institute and State University, 1405 Perry St., Derring Hall (RM4044), Blacksburg, Virginia 24061, USA*

[2]*Department of Earth Sciences, Durham University, Science Laboratories, South Road, Durham, DH1 3LE, UK*

**Email: theo1085@vt.edu*

Formatted for *Nature*

Abstract

Silicate weathering consumes atmospheric carbon dioxide and is thought to stabilize Earth's long-term climate (Walker et al., 1981; Berner et al., 1983; Kump et al., 2000). However, the potential influence of silicate weathering on atmospheric pCO_2 levels on geologically short timescales ($10^3 – 10^5$ years) remains poorly constrained. Here we use rhenium and osmium geochemistry to reconstruct global paleoenvironmental changes during the Toarcian Oceanic Anoxic Event (T-OAE; ~183.1 Ma and duration of ~300 kyr (Sell et al., 2014)), which is associated with extreme global warming, enhanced precipitation rates, marine anoxia, and extinctions. The osmium isotope data and numerical modeling results suggest that silicate weathering rates may have increased by 240 – 530%, which would have sequestered significant amounts of atmospheric CO_2. These results also suggest that a global drawdown of rhenium from seawater occurred during the T-OAE as a function of the development of widespread bottom water anoxia. These data support the scenario that increased chemical weathering mediated bioproductivity and subsequently shallow-water anoxia through the increased supply of nutrients to the oceans. Further, increased chemical weathering rates can also act as a negative feedback on atmospheric pCO_2 levels on short timescales, thereby triggering several biogeochemical feedbacks that may serve to end an OAE.

1. Introduction

The chemical weathering of silicate rocks, known as silicate weathering, constitutes a negative and stabilizing feedback to Earth's long-term ($10^8 – 10^9$ yr) climate by consuming atmospheric CO_2 and therefore modulates the greenhouse effect and global temperatures (Walker et al., 1981; Berner et al., 1983; Kump et al., 2000). On these timescales, chemical weathering is

dominantly regulated by tectonics, atmospheric pCO_2, temperature, and the strength of the hydrological cycle (Kump et al., 2000). Silicate weathering also releases Ca and Mg to the oceans, resulting in the deposition of $(Ca,Mg)CO_3$ (Walker et al., 1981; Berner et al., 1983; Kump et al., 2000**)**. This overall net reaction, where carbon dioxide (CO_2) is consumed, is described by the following reaction:

$$CaSiO_3 + CO_2 \rightarrow CaCO_3 + SiO_2 \qquad (1)$$

Although the influence of silicate weathering on long-term climate is well studied (e.g., Kump et al., 2000 and references therein), much less is known about how this process potentially operates and influences climatic events on shorter times scales ($<10^6$ yr) (e.g. Foster and Vance, 2006).

The T-OAE of the Jurassic Period was one such interval marked by global warming, perturbations to the global carbon cycle (Jenkyns, 2010), the widespread deposition of organic-rich sediments (Jenkyns, 1988), and elevated marine extinction rates (Harries and Little, 1999). These environmental and ecological changes have been linked to the emplacement of the Karoo-Ferrar Large Igneous Province (Pálfy and Smith, 2000) (Fig. 1 for Toarcian paleogeography and extent of Karoo-Ferrar LIP). The proposed driver(s) of the T-OAE carbon cycle perturbations, recorded as a pronounced negative carbon isotope excursion (CIE), have been hypothesized to be the injection of mantle-derived CO_2 and thermogenic methane (CH_4) from the emplacement of Karoo-Ferrar the Large Igneous Province (McElwain et al., 2005; Beerling and Brentnall, 2007; Svensen et al., 2007) and subsequent releases of methane from clathrates (Hesselbo et al. 2000; Kemp et al., 2005) and wetlands (Chapter 1, Them et al.). Under an enhanced greenhouse effect caused by elevated levels of greenhouse gases, global temperatures would have increased and the hydrological cycle would have strengthened due to the atmosphere's ability to accommodate greater amounts of water at higher temperatures. In this scenario, rising pCO_2, global

temperatures and precipitation rates should have led to enhanced chemical weathering rates (e.g., Kump et al., 2000). Here we investigate the accelerated weathering hypothesis during the T-OAE by utilizing the Re-Os isotope system (see Supporting Information).

Average crustal abundances of Re and Os are 390 parts per trillion (ppt) and 50 ppt, respectively (Esser and Turekian, 2004; Sun et al., 2013) and their abundances in organic-rich sediments and shales may reach 500 parts per billion (ppb) for Re and 4 ppb for Os (Cohen et al., 1999). ^{187}Re decays to ^{187}Os by β-emission with a half-life of c. 41.6 Ga and has a radioactive constant (λ) of 1.666 x 10^{-11} a^{-1} (Smoliar et al., 1996). Average upper crustal $^{187}Os/^{188}Os$ values are 1.4, much higher than the mantle's value of 0.127 (Esser and Turekian, 1993). These end-member values make is possible to differentiate between sources of osmium to the ocean in the geological record.

The $^{187}Os/^{188}Os$ composition of the seawater ($^{187}Os/^{188}Os_{sw}$) reflects the sources of osmium to ocean: rivers that drain continents ($^{187}Os/^{188}Os_{cont} \approx 1.4$) and aeolian dust ($^{187}Os/^{188}Os_{aeol} \approx 1.04$) represent radiogenic end-members, and alteration of juvenile ocean crust or from the mantle ($^{187}Os/^{188}Os_{m} \approx 0.127$) and cosmic dust/bolides ($^{187}Os/^{188}Os_{cos} \approx 0.12$) represent unradiogenic end-members (Peucker-Ehrenbrink and Ravizza, 2000) (Fig. 2). Because the flux of cosmic and aeolian dust represent a small fraction of the global input of osmium to the oceans and do not readily dissolve in seawater, they are thought to not significantly affect the dissolved $^{187}Os/^{188}Os_{sw}$ composition (Peucker-Ehrenbrink, 1996; Peucker-Ehrenbrink and Ravizza, 2000). Thus the relative influence of the radiogenic continental and unradiogenic mantle input may be calculated by using a simple two-component mixing model (see Supplemental Information). Applying this model to the modern osmium isotopic composition of seawater ($^{187}Os/^{188}Os_{sw} = 1.06$) suggests the greater influence of continental inputs (~73%) over

mantle-derived osmium (~27%; see Supplemental Information). Furthermore, due to the short residence time (~10^3 – 10^4 yr) of osmium in the oceans (Peucker-Ehrenbrink and Ravizza, 2000; Oxburgh, 2001), this system has the potential to record relatively abrupt, ephemeral changes in global weathering patterns (on the order of 10^3 to 10^5 years) in the geological record (Cohen et al., 1999).

Additionally, redox-sensitive elements such as rhenium may become enriched in sediments deposited under suboxic to anoxic conditions due to their decreased solubility under these redox conditions (*e.g.*, Crusius et al., 1996; Morford and Emerson, 1999; Tribovillard et al., 2006). However, during an oceanic anoxic event, when the widespread deposition of organic-rich sediments occurs, the marine reservoir of these elements may decline and the enrichment at any given location may also decline (*e.g.*, Algeo, 2004). Here, we also utilize Re abundances as paleo-redox indicator, which may give insight into the extent of marine anoxia during the T-OAE.

The $^{187}Os/^{188}Os$ compositions of organic-rich sediments and mudrocks ("black shales") are known to record the marine $^{187}Os/^{188}Os$ composition of contemporaneous seawater when they were deposited (Cohen et al., 1999), thus are an archive of past changes in the ocean osmium isotope composition. A previous Os isotope study of the T-OAE interval from a sedimentary succession from the Cleveland Basin of Yorkshire, United Kingdom showed that during the CIE, there was a concomitant, transient increase of $^{187}Os/^{188}Os_{sw}$ values (Fig. 3) (Cohen et al., 2004). This record was originally interpreted to be the result of an increase in continental weathering rates of 400 to 800% (Cohen et al., 2004). However, this interpretation has been disputed and these data have been suggested to reflect a local change in the Euro-Boreal Ocean where this succession was deposited (Fig. 1). This reinterpretation suggests that $^{187}Os/^{188}Os_{sw}$ composition

of the Euro-Boreal Ocean was influenced by enhanced local runoff, and thus the Yorkshire $^{187}Os/^{188}Os$ record does not reflect a global weathering signal (McArthur et al., 2008). Key to this dispute is whether the Cleveland Basin was hydrographically restricted enough for local processes to significantly modify the local $^{187}Os/^{188}Os_{sw}$ signal through the drawdown of rhenium (McArthur et al., 2008). To test whether the transient increase in $^{187}Os/^{188}Os$ observed across the T-OAE was a global signal, we investigate the Os isotope record from a different location, which was deposited on the margin of another ocean basin during the Toarcian (Fig. 1).

Here, we present a new geochemical dataset (see SI spreadsheet) from the Early Jurassic Fernie Formation of the Western Canada Sedimentary Basin located in present-day western Alberta (Fig. 1). Ammonite biostratigraphy (Hall, 1984, 1987; Asgar-Deen et al., 2003; Chapter 1, Them et al.) and carbon isotope stratigraphy (Chapter 1, Them et al.) of the Fernie Formation at East Tributary of Bighorn Creek, Ya Ha Tinda, Alberta has identified the late Pliensbachian to middle Toarcian interval and the Toarcian CIE. The East Tributary succession contains organic-rich strata throughout the studied interval (Chapter 1, Them et al.) and was deposited on the eastern margin of Panthalassa (Fig. 1), and thus represents an ideal location to reconstruct the global $^{187}Os/^{188}Os_{sw}$ composition for this time interval ($^{187}Os/^{188}Os_i$; see Supplemental Information).

2. Results

Our new high-resolution $^{187}Os/^{188}Os_i$ record displays extremely unradiogenic values ($^{187}Os/^{188}Os_i \approx 0.25$) during the Pliensbachian and early Toarcian, followed by a prominent radiogenic excursion ($^{187}Os/^{188}Os_i \approx 0.6$) during the Toarcian CIE (Fig. 4). $^{187}Os/^{188}Os_i$ values

decrease after the Toarcian CIE and asymptotically approach $^{187}Os/^{188}Os_i \approx 0.4$ (Fig. 2; see Supplemental Information for calculation). Rhenium abundances are generally high before the CIE (30 – 256 ppb), significantly decrease during the CIE (4 – 17 ppb), and return to higher values after the CIE (34 – 86 ppb) (Fig. 4).

3. Discussion

Other marine $^{187}Os/^{188}Os_i$ records from the Early Jurassic generally show unradiogenic values (Cohen et al., 2004; Cohen and Coe, 2007; Porter et al., 2013) that are likely related to the weathering of the Central Atlantic Magmatic Province (CAMP) and alteration of juvenile oceanic lithosphere created during the initial opening of the North Atlantic (Porter et al., 2013; cf. Cohen and Coe, 2007). The late Pliensbachian portion of our record from the eastern Panthalassa has similar values to the early Pliensbachian record from the Euro-Boreal Ocean (Porter et al., 2013), which suggests they are representative of the global $^{187}Os/^{188}Os_{sw}$ values of the Early Jurassic ocean.

The Yorkshire dataset shows unradiogenic $^{187}Os/^{188}Os_i$ values before and after the Toarcian CIE (0.2 and 0.4 respectively); however, they are significantly more radiogenic ($^{187}Os/^{188}Os_i \approx 1$) during the CIE (Cohen et al., 2004) (Fig. 3). At East Tributary $^{187}Os/^{188}Os_i$ values before and after the Toarcian CIE are the same as those observed at Yorkshire. However, the magnitude of the positive $^{187}Os/^{188}Os_i$ excursion during the CIE is much smaller at only ~0.6. The differences observed between East Tributary $^{187}Os/^{188}Os_i$ values and the extreme values observed during the T-OAE interval at Yorkshire lend support to the suggestion that the Yorkshire T-OAE $^{187}Os/^{188}Os_{sw}$ values were influenced by the local riverine Os input (e.g.,

$^{187}Os/^{188}Os_{cont}$). A fully coupled ocean-atmosphere model suggests that precipitation significantly increased in this region during the T-OAE (Dera and Donnadieu, 2012), and along with local hydrographic restriction due to low salinity surface waters causing stratification (e.g., McArthur et al., 2008), may have resulted in such extreme radiogenic local $^{187}Os/^{188}Os_{sw}$ values. The lithology and age of rocks in the drainage basin impart a substantial control on river $^{187}Os/^{188}Os$ composition (Levasseur et al., 1999; Huh et al., 2004), and must be taken into consideration when utilizing Re-Os system as a paleoceanographic tool. As such, we advocate, when possible, that it is necessary to analyze Os isotopes from coeval stratigraphic succession that were deposited in different sedimentary basins. This is particularly critical for time intervals older than the Early Jurassic where deep-sea sediments from the open ocean are much less common. Otherwise, quantification of these global weathering fluxes could be potentially biased by local changes in marine Re-Os chemistry.

The overall pattern observed in East Tributary (Fig. 4) follows that observed at Yorkshire (Fig. 3) and is consistent with a transient interval of significantly increased delivery of continental materials to the oceans. The observation of a less extreme $^{187}Os/^{188}Os_i$ excursion suggests that the Panthalassa site potentially may have been less influenced by local processes, as compared to Yorkshire, and therefore may be more representative of global osmium seawater chemistry during the T-OAE. Using the reconstructed osmium isotope composition of eastern Panthalassa and a simple two end-member mixing model (described in Supplementary Information), the contribution of continental-derived osmium would have increased from ~11% before the Toarcian CIE to ~40% during the CIE, and decreased to ~21% after the CIE. However, if a more radiogenic $^{187}Os/^{188}Os_{cont}$ end-member is used during the Toarcian CIE (see below), then the contribution of continental-derived osmium would have increased to only

~25%.

Both the Alberta and Yorkshire sections show similar stratigraphic trends in rhenium abundances across the T-OAE: these two sites, located in different paleogeographic settings, show similar magnitudes of Re depletion during the T-OAE. The Yorkshire Re abundances are approximately 8 – 15 ppb during the *Cleviceras exaratum* subzone, before increasing to 16 – 57 ppb in the *Harpoceras falciferum* subzone (Cohen et al., 2004). In East Tributary, Re abundances follow a similar pattern of depletion during the T-OAE and enrichment following it (Fig. 4). Therefore, the suggestion that the local drawdown of Re was the sole cause of the $^{187}Os/^{188}Os$ excursion in Yorkshire (McArthur et al., 2008) is doubtful since both locations record a decline of the Re abundances during the event. The similarity of these two records suggests that the decline in Re abundances during the T-OAE was the result of global drawdown of the marine Re reservoir as the result of the increased geographic extent of marine anoxia (e.g. Algeo, 2004).

To gain a more quantitative measure of the changes in the marine Os cycle during the Toarcian we employed a numerical box model that simulates the osmium inventory of the ocean (see details in Supplemental Information). Specifically, we test whether the osmium isotope excursion associated with the Toarcian OAE can be reproduced by transiently increasing the weathering input of osmium to the ocean. We also explored other potential scenarios that may have driven the osmium isotope record, but are unrealistic (see details in Supplemental Information). The numerical model results show that the osmium isotope excursion can be reproduced by an approximate six-fold increase of continental-derived osmium to the oceans over 100 kyr (Fig. 4), indicating a ~530% increase in weathering rates. However, preferential weathering of lithologies such as organic-rich shales (Peucker-Ehrenbrink and Hannigan, 2000; Jaffe et al., 2002; Pierson-Wickmann et al., 2002) could, potentially, significantly change the

$^{187}Os/^{188}Os_{cont}$ values to a more radiogenic end-member. We investigated this possibility by running simulations and elevating $^{187}Os/^{188}Os_{cont}$ from 1.4 to 2 (see Supplemental Information for explanation of this choice for an end-member value). In these simulations, an approximate three-fold increase of continental-derived osmium to the oceans was necessary to reproduce the excursion (Fig. 5). Therefore, we conservatively suggest that T-OAE weathering rates increased by as much as ~240%, as Re- and Os-rich sedimentary rocks would have weathered preferentially compared to more crystalline rocks. Furthermore, it is also possible that increased global precipitation rates may have released any dissolved Re and Os stored in floodplains and estuaries, and there may have been significant changes in groundwater dynamics (e.g., Peucker-Ehrenbrink, 2002), thus potentially decreasing the calculated increases in chemical weathering rate.

4. Conclusions

Based on our modeling results, the increase in continental weathering rates during the T-OAE may be one of the largest observed during Phanerozoic. Chemical weathering rates are also thought to have significantly increased across the Permian-Triassic boundary (Sheldon, 2006), Triassic-Jurassic boundary (Beerling and Berner, 2002; Kuroda et al., 2010), and the Paleocene-Eocene Thermal Maximum (Ravizza et al., 2001), all of which are associated with environmental deterioration and either a major or mass extinction (e.g., Hönisch et al., 2012). The increases calculated from this study are much greater than those reconstructed during the Pleistocene glacial cycles (e.g., Oxburgh et al., 2007), although some evidence suggests that there was no net change during that time (Foster and Vance, 2006). However, the rapid response of the Os isotope

system during the T-OAE suggests that the silicate weathering feedback may respond to episodes of rapid climatic warming on shorter timescales (10^3 – 10^6 years) than has been previously suggested. In the case of the Toarcian OAE, increased chemical weathering may have played a role in reversing the enhanced greenhouse state induced by Karoo-Ferrar magmatism. As atmospheric CO_2 was consumed through this mechanism and the burial of organic-rich sediments, global temperatures would have decreased (e.g., Cohen et al., 2004; Jenkyns, 2010). As modern atmospheric CO_2 levels continue to increase at rates much higher than any point during the Cenozoic (Zeebe et al. 2016), the response of increased silicate weathering rates may eventually act as a negative feedback to future global warming, although on timescales much longer than what is necessary to mitigate short-term environmental deterioration to this warming.

Methods

See Supplemental Information for methodologies.

Acknowledgements

TRT would like to thank the Virginia Tech College of Science Roundtable grant committee for the Make-a-Difference Scholarship and the Geological Society of America, American Association of Petroleum Geologists, and International Association of Sedimentologists graduate student grant programs for funding (IAS grant funded the pilot study). A grant to BCG from the NSF (EAR-1324752) helped fund this work. Thanks to Dr. Joanna Hesselink for laboratory assistance. Thanks to Angela Gerhardt, Emma Tulsky, and Selva Marroquín for their help in collecting samples. Sample collections were authorized by the following permits: Parks Canada, Permit No: YHTR-2014-16156; RTMP, Permit No: 13-058, 14-009, 15-019.

Author Contributions

TRT, BCG, DG, and DS designed the study. TRT and BCG collected samples. TRT and DS conducted the Re-Os geochemical analyses. TRT and BCG conducted the numerical modeling. All authors analyzed the data. TRT and BCG wrote the paper with contributions from all the authors.

5. References

Algeo, T.J. Can marine anoxic events draw down the trace element inventory of seawater? Geology 32, 1057–1060 (2004).

Asgar–Deen, M., Hall, R., Craig, J. & Riediger, C. New biostratigraphic data from the Lower Jurassic Fernie Formation in the subsurface of west-central Alberta and their stratigraphic implications. Can. J. Earth Sci. 40, 45–63 (2003).

Beerling, D.J. & Berner, R.A. Biogeochemical constraints on the Triassic-Jurassic boundary carbon cycle event. Glob. Biogeo. Cycles 16, GB001637 (2002).

Beerling, D.J. & Brentnall S.J. Numerical evaluation of mechanisms driving Early Jurassic changes in global carbon cycling. Geology 35, 247–250 (2007).

Berner, R.A., Lasaga, A.C. & Garrels, R.M. The carbonate-silicate geochemical cycle and its effect on atmospheric carbon dioxide over the past 100 million years. Am. J. Sci. 283, 641–683 (1983).

Cohen, A.S. The rhenium-osmium isotope system: applications to palaeoenvironmental problems. J. Geol. Soc. Lon. 161, 729–734 (2004).

Cohen, A.S. & Coe, A.L., New geochemical evidence for the onset of volcanism in the Central Atlantic magmatic province and environmental change at the Triassic-Jurassic boundary. Geology 30, 267–270 (2002).

Cohen, A.S., Coe, A.L., Bartlett, J.M. & Hawkesworth, C.J. Precise Re—Os ages of organic-rich mudrocks and the Os isotope composition of Jurassic seawater. Earth Plan. Sci. Lett. 167, 159–173 (1999).

Cohen, A.S., Coe, A.L., Harding, S.M. & Schwark, L. Osmium isotope evidence for the regulation of atmospheric CO_2 by continental weathering. Geology 32, 157– 160 (2004).

Crusius, J., Calvert, S., Pedersen, T. & Sage, D. Rhenium and molybdenum enrichments in sediments as indicators of oxic, suboxic and sulfidic conditions of deposition. Earth Plan. Sci. Lett. 145, 65–78 (1996).

Esser, B.K. & Turekian, K.K. The osmium isotopic composition of the continental crust. Geochim. Cosmochim. Acta 57, 3093–3104 (1993).

Hall, R.L. Lithostratigraphy and biostratigraphy of the Fernie Formation (Jurassic) in the southern Canadian Rocky Mountains, in Stott, D.F. & Glass, D.J., eds., The Mesozoic of Middle North America. Can. Soc. Petr. Geol. Mem. 9, 233–247 (1984).

Hall, R.L. New Lower Jurassic ammonite faunas from the Fernie Formation, southern Canadian Rocky Mountains. Can. J. Earth Sci. 24, 1688–1704 (1987).

Harries, P.J. & Little, C.T.S. The early Toarcian (Early Jurassic) and the Cenomanian-Turonian (Late Cretaceous) mass extinctions: similarities and contrasts. Palaeogeo. Palaeoclim. Palaeoecol. 154, 39–66 (1999).

Hesselbo, S.P. et al. Massive dissociation of gas hydrate during a Jurassic oceanic anoxic event. Nature 406, 392–395 (2000).

Hönisch et al., B. The Geological Record of Ocean Acidification. Science 335, 1058–1063 (2012).

Huh, Y., Birck, J.-L. & Allègre, C.J. Osmium isotope geochemistry in the Mackenzie River basin. Earth Plan. Sci. Lett. 222, 115–29 (2004).

Jaffe, L.A., Peucker-Ehrenbrink, B. & Petsch S.T. Mobility of rhenium, platinum group elements and organic carbon during black shale weathering. Earth Plan. Sci. Lett. 198, 339–353 (2002).

Jenkyns, H.C. The Early Toarcian (Jurassic) Anoxic Event: Stratigraphic, Sedimentary, and

Geochemical Evidence. Am. J. Sci. 288, 101–151 (1988).

Jenknys, H.C. Geochemistry of oceanic anoxic events: G^3 11, Q03004 (2010).

Kemp, D.B., Coe A.L., Cohen A.S. & Schwark L. Astronomical pacing of methane release in the Early Jurassic period. Nature 437, 396–399 (2005).

Korte, C. et al. Jurassic climate mode governed by ocean gateway. Nature Comm. 6:10015 (2015).

Kump, L.R., Brantley, S.L. & Arthur, M.A. Chemical Weathering, Atmospheric CO2, and Climate. Ann. Rev. Earth Plan. Sci. 28, 611–667 (2000).

Kuroda, J., Hori, R.S., Suzuki, K., Gröcke, D.R. & Ohkouchi, N. Marine osmium isotope record across the Triassic-Jurassic boundary from a Pacific pelagic site. Geology 38, 1095–9098 (2010).

Levasseur, S., Birck, J.-L. & Allègre, C.J. The osmium river flux and the oceanic mass balance of osmium. Earth Plan. Sci. Lett. 174, 7–23 (1999).

McArthur, J.M., Algeo, T.J., van de Schootbrugge, B., Li, Q. & Howarth, R.J. Basinal restriction, black shales, Re-Os dating, and the Early Toarcian (Jurassic) oceanic anoxic event. Paleoceanography 23, PA4217 (2008).

McElwain J.C., Wade-Murphy J. & Hesselbo S.P. Changes in carbon dioxide during an oceanic anoxic event linked to intrusion into Gondwana coals. Nature 435, 479–482 (2005).

Morford, J.L. & Emerson, S. The geochemistry of redox sensitive trace metals in sediments. Geochim. Cosmochim. Acta 63, 1735–1750 (1999).

Oxburgh, R., Pierson-Wickmann, A.-C., Reisberg, L. & Hemming, S. Climate-correlated variations in seawater $^{187}Os/^{188}Os$ over the past 200,000 years: Evidence from the Cariaco Basin, Venezuela. Earth Plan. Sci. Lett. 263, 246–258 (2007).

Pálfy, J. & Smith P.L. Synchrony between Early Jurassic extinction, oceanic anoxic event, and the Karoo-Ferrar flood basalt volcanism. Geology 28, 747–750 (2000).

Peucker-Ehrenbrink, B. Accretion of extraterrestrial matter during the last 80 million years and its effect on the marine osmium isotope record. Geochim. Cosmochim. Acta 60, 3187–3196 (1996).

Peucker-Ehrenbrink, B. Comment on "Residence time of osmium in the oceans" by Rachel Oxburgh. G^3 3, 1–4 (2002).

Peucker-Ehrenbrink, B. & Hannigan, R.E. Effect of black shale weathering on the mobility of rhenium and platinum group elements. Geology 28, 475–478 (2000).

Peucker-Ehrenbrink, B. & Ravizza, G. The marine osmium isotope record. Terra Nova 12, 205–219 (2000).

Pierson-Wickmann, A.-C., Reisberg, L. & France-Lanord, C. Behavior of Re and Os during low-temperature alteration: Results from Himalayan soils and altered black shales. Geochim. Cosmochim. Acta 66, 1539–1548 (2002).

Porter, S.J., Selby, D., Suzuki, K. & Gröcke, D. Opening of a trans-Pangaean marine corridor during the Early Jurassic: Insights from osmium isotopes across the Sinemurian-Pliensbachian GSSP, Robin Hood's Bay, UK. Palaeogeo. Palaeoclim. Palaeoecol. 375, 50–58 (2013).

Ravizza, G., Norris, R.N. & Blusztajn, J. An osmium isotope excursion associated with the late Paleocene thermal maximum: Evidence of intensified chemical weathering. Paleocean. 16, 155–163 (2001).

Scotese, C.R., 2001, Atlas of Earth History. PALEOMAP Project, Arlington, Texas.

Sell, B. et al. Evaluating the temporal link between the Karoo LIP and climatic—biologic events of the Toarcian Stage with high-precision U-Pb geochronology. Earth Plan. Sci. Lett. 408, 48–56 (2014).

Sheldon, N.D. Abrupt chemical weathering increase across the Permian-Triassic boundary. Palaeogeo. Palaeoclim. Palaeoecol. 231, 315–321 (2006).

Svensen, H. et al. Hydrothermal venting of greenhouse gases triggering Early Jurassic global warming. Earth Plan. Sci. Lett. 256, 554–566 (2007).

Tribovillard, N., Algeo, T.J., Lyons, T. & Riboulleau, A. Trace metals as paleoredox and paleoproductivity proxies: An update. Chem. Geol. 232, 12–32 (2006).

Walker, J.C.G., Hays, P.B. & Kasting, J.F. A negative feedback mechanism for the long-term stabilization of Earth's surface temperature. J. Geophys. Res. 86, 9776–9782 (1981).

Zeebe, R.E., Ridgwell, A. & Zachos, J.C. Anthropogenic carbon release rate unprecedented during the past 66 million years. Nature 9, 325–329 (2016).

6. Figures

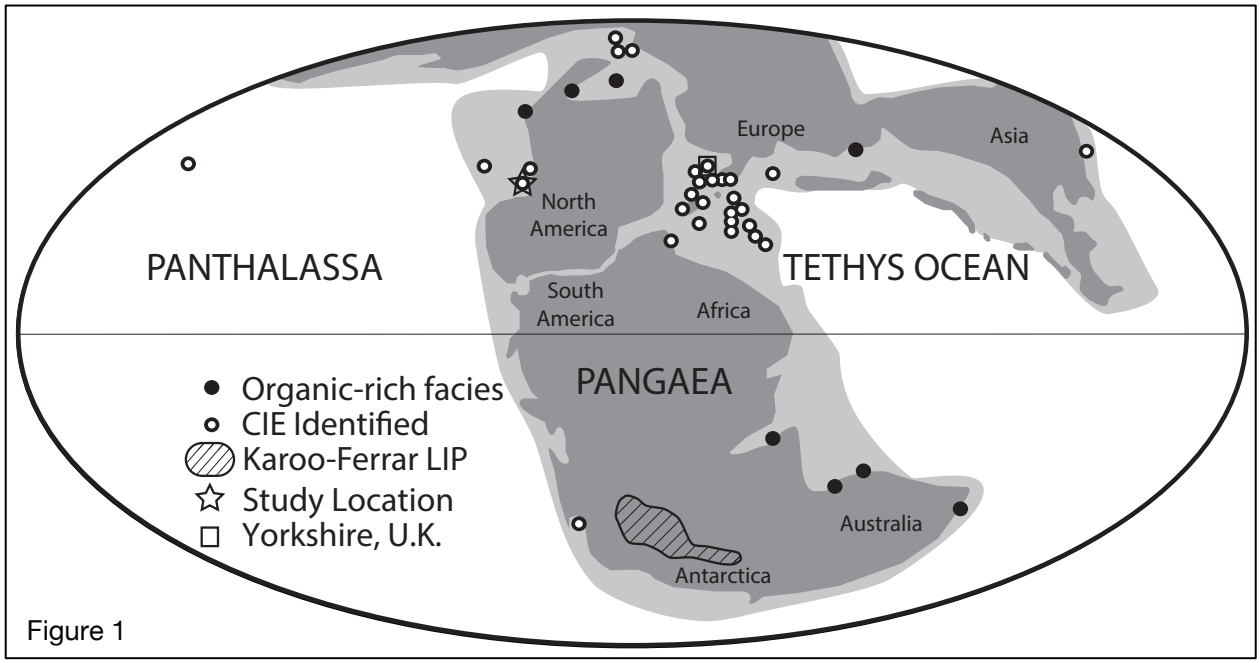

Figure 1. Global paleogeography of the Early Toarcian (modified from Scotese, 2001). Star represents this study's location. Square represents the Yorkshire study location of Cohen et al. (2004). Hatched outline in southern Africa and Antarctica represents location and known extent of Karoo-Ferrar Large Igneous Province. Dark grey represents landmasses, light grey represents shallow seas, and white represents open oceans.

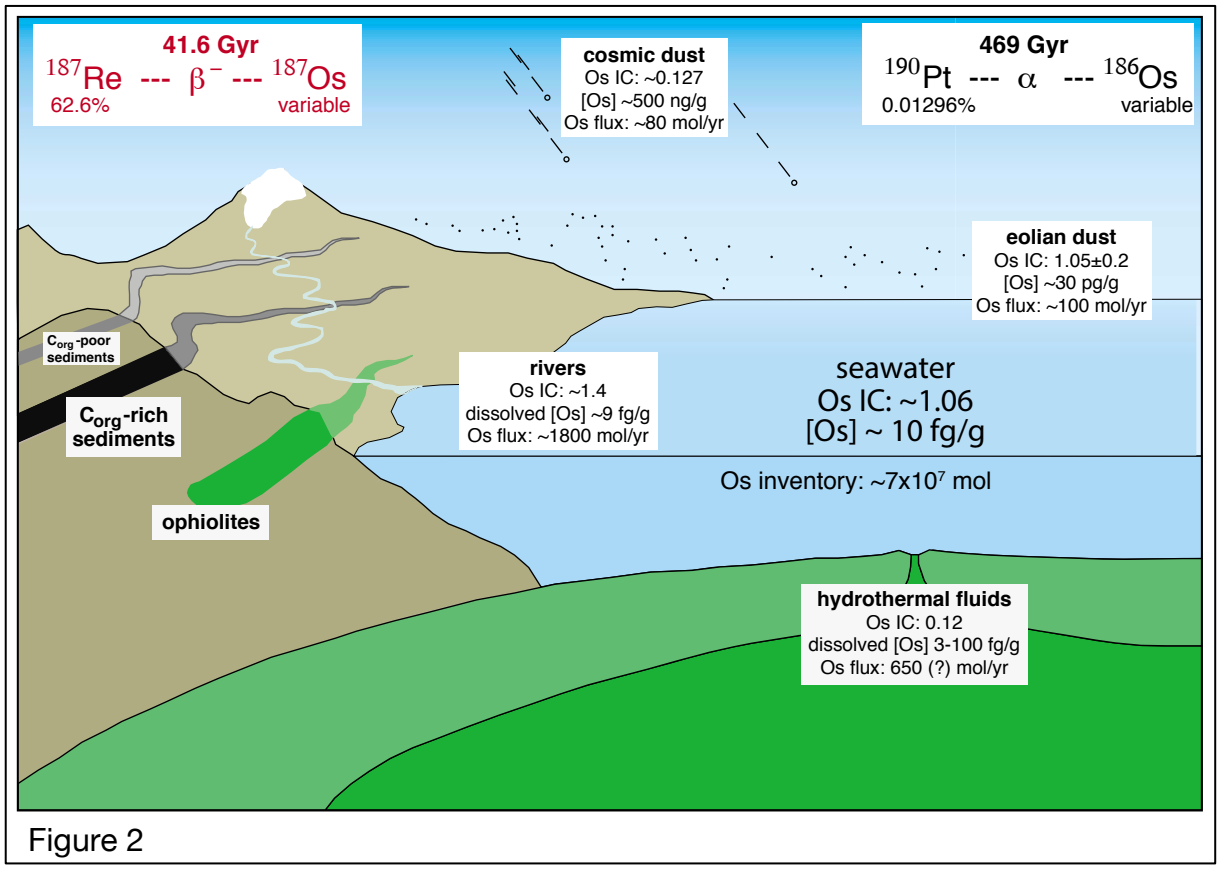

Figure 2

Figure 2: The exogenic osmium cycle (modified from Peucker-Ehrenbrink and Ravizza, 2000). The major inputs of osmium to oceans are from the weathering of materials from the continents ($^{187}Os/^{188}Os_{cont} \approx 1.4$) and the alteration of juvenile oceanic crust ($^{187}Os/^{188}Os_{m} \approx 0.127$). Sequestration of the seawater inventory of osmium occurs during precipitation of iron-manganese crusts on the ocean bottom and through biological uptake associated with primary productivity and burial in sediments.

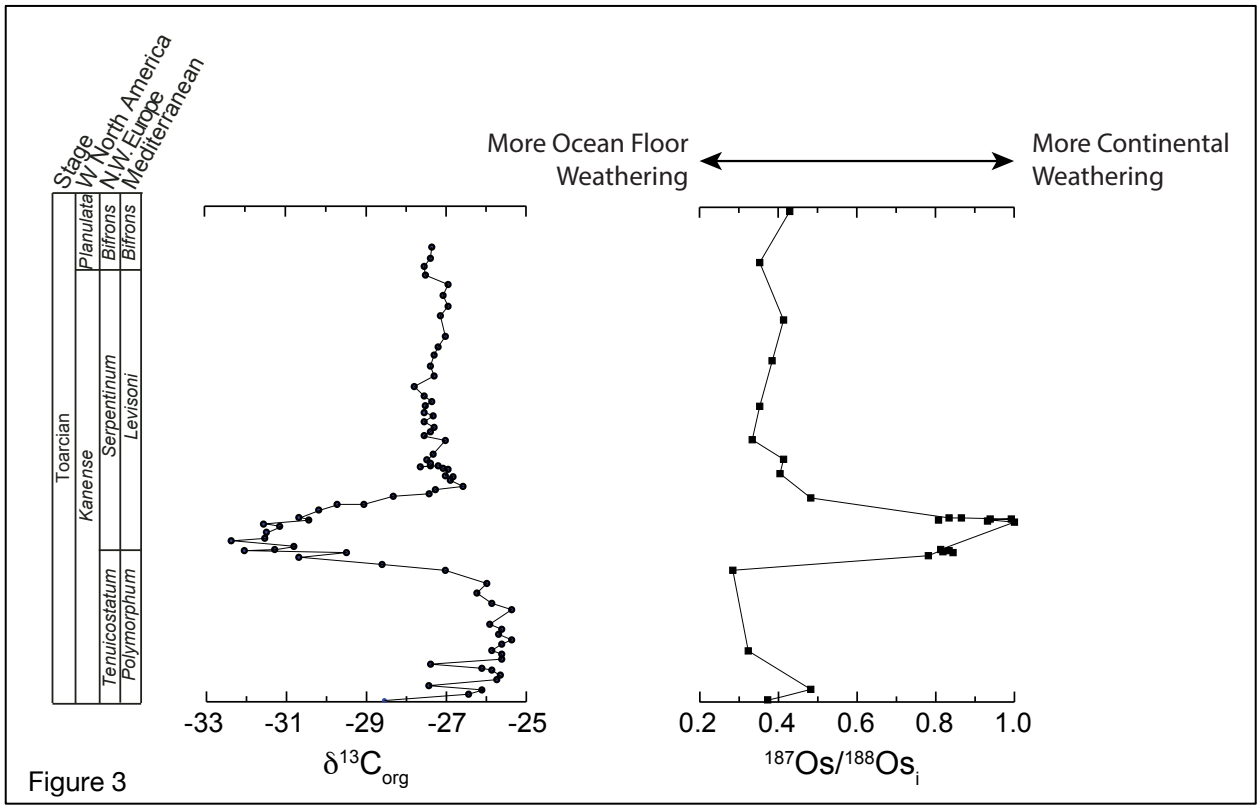

Figure 3: Record of the osmium isotope excursion across the T-OAE CIE from Yorkshire, United Kingdom. This dataset was originally interpreted to represent a 400 – 800% increase in continental weathering rates (Cohen et al., 2004), however another interpretation suggests that the radiogenic values during the *Cleviceras exaratum* ammonite subzone were caused by hydrographic restriction (McArthur et al., 2008).

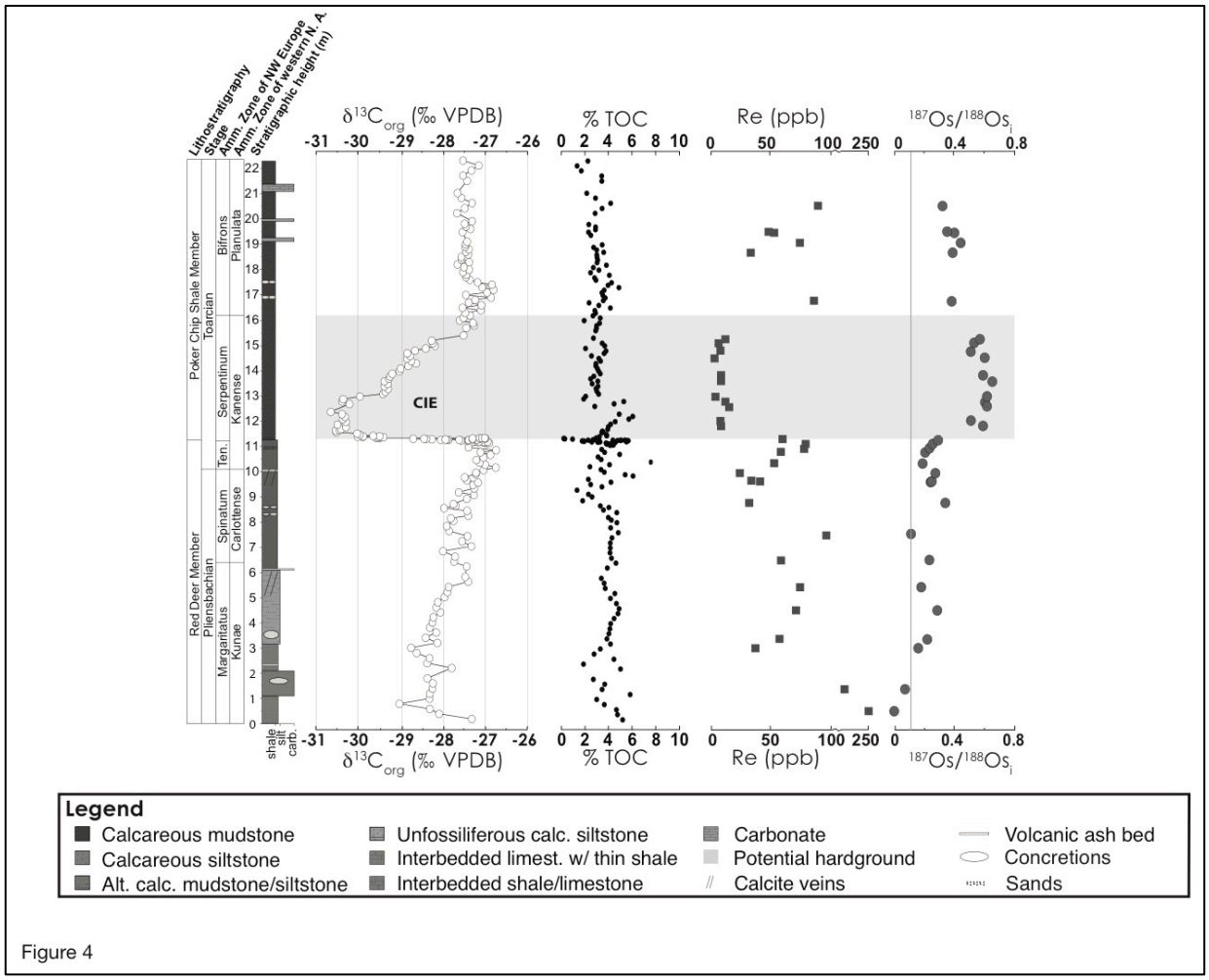

Figure 4

Figure 4: Chemostratigraphy of the Early Jurassic Fernie Formation from East Tributary of Bighorn Creek Alberta. $d^{13}C_{org}$ = organic carbon isotopic compositions. $^{187}Os/^{188}Os_i$ = initial osmium isotopic composition of organic-rich deposits. Lithostratigraphic members of the Fernie Formation, Stages of the Jurassic, and ammonite zonations for both northwestern Europe and western North American shown to the left of the stratigraphic column (refer to Them et al. (in review) for the details of their placements). Shaded gray box represents Toarcian CIE. Vertical gray line in $^{187}Os/^{188}Os_i$ record is the end-member $^{187}Os/^{188}Os_m$ value of ~0.127 (see Supplemental Information for explanation as to why the lowest two samples plot to the left of this line).

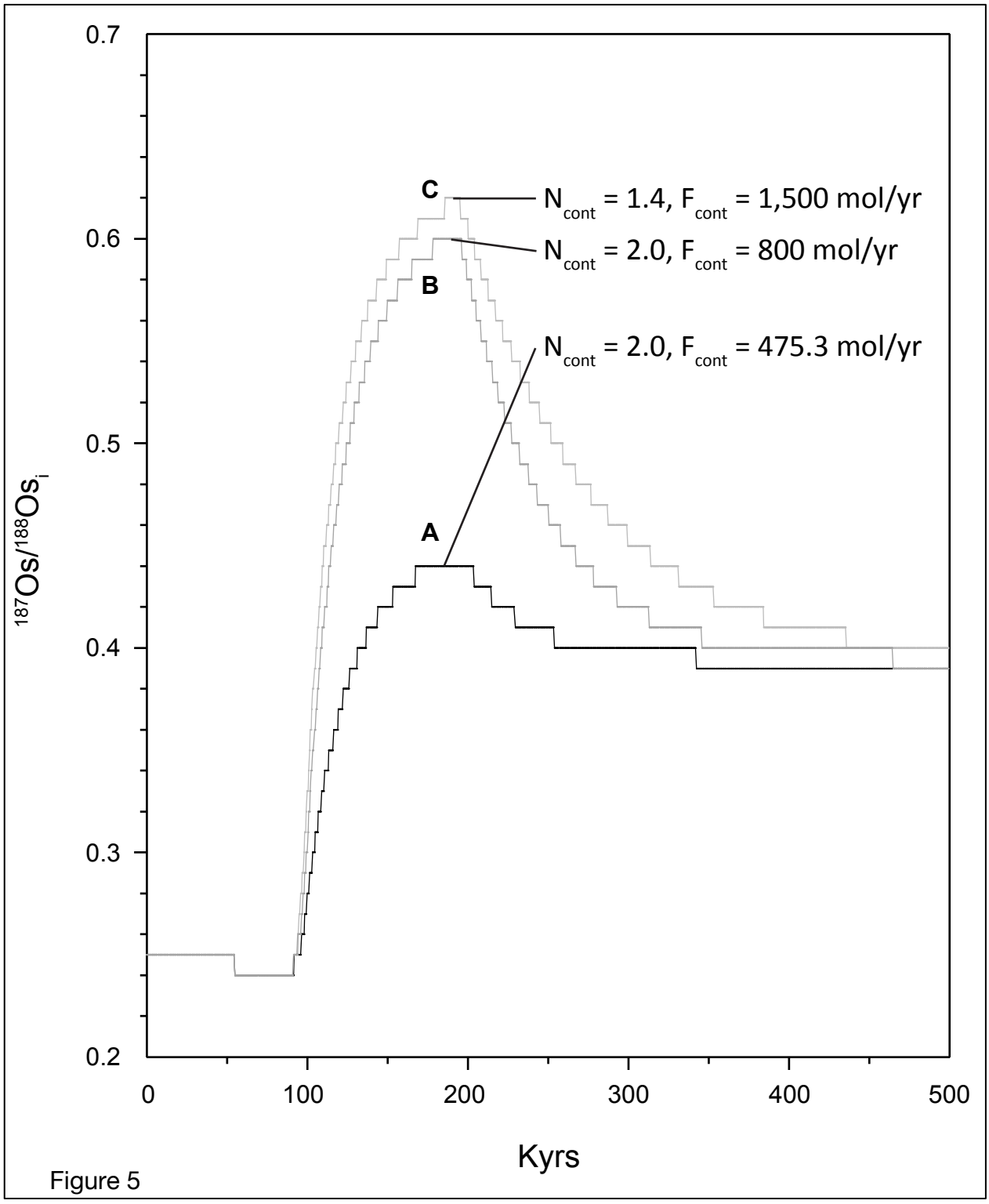
0.7
0.6
0.5
0.4
0.3
0.2
$^{187}Os/^{188}Os_i$
0
100
200
300
400
500
Kyrs
C
B
A
N_{cont} = 1.4, F_{cont} = 1,500 mol/yr
N_{cont} = 2.0, F_{cont} = 800 mol/yr
N_{cont} = 2.0, F_{cont} = 475.3 mol/yr

Figure 5

Figure 5: Examples of the modeled osmium isotopic composition of the ocean over the T-OAE. The pre-event steady state conditions, F_{cont} = 237.65 moles/year, F_m = 2,212.35 moles/year, F_{sed} = 2,450 moles/year and M_{ocean} = $7x10^7$ moles. F_{cont} represents the flux of osmium to the oceans from rivers draining continents, F_m represents the flux of osmium to the oceans from the alteration of juvenile oceanic crust or hydrothermal vent systems, and F_{sed} represents the amount of osmium being sequestered. N_{cont} represents the osmium isotopic composition of river water draining continents. **A)** For this model run, the Os isotopic composition of river water was increased to 2.0 and the flux of osmium from continents was increased two-fold during the Toarcian OAE. This resulted in the seawater Os isotope values to increase to 0.44, which does not reproduce the observed geochemical data. **B)** Model run where the Os isotopic composition of river water was increased to 2.0 during the Toarcian OAE, and the flux of osmium from continents was increased by ~3.4x. This reproduced the osmium isotope excursion from eastern Panthalassa. **C)** The osmium isotope composition of river water was kept at 1.4 during the Toarcian OAE, and the flux of osmium from continents was increased by ~6.3x in order to reproduce the osmium isotope excursion from eastern Panthalassa.

7. Supplemental Information:

Re-Os evidence for increased chemical weathering during the Toarcian Oceanic Anoxic Event

(T.R. Them II, B.C. Gill, D.R. Gröcke, D. Selby)

SUPPLEMENTAL INFORMATION

$\delta^{13}C$ & TOC analysis

Procedures outlined in Chapter 1, Them et al.

Rhenium and osmium isotopic analysis

In order to isolate primarily the hydrogenous rhenium and osmium from our samples, and minimize the removal of detrital rhenium and osmium, we followed the procedures of Selby and Creaser (2003) and Cumming et al. (2013) were followed. Between ~0.25 and 1 g of sample powder (dependent upon previously measured rhenium abundances via inductively-coupled plasma mass spectrometry) were digested with a known amount of ^{185}Re and ^{190}Os tracer (spike) solutions in 8 mL of a CrO_3-H_2SO_4 solution; this reaction occurred in sealed Carius tubes, which were heated incrementally to 220 °C for 48 hours. The tubes were allowed to cool before opening. The osmium was immediately isolated and purified from the acid medium by solvent extraction using chloroform (ensures no osmium loss in vapor phase). This step was followed by back reduction into HBr, and finally by micro-distillation. Rhenium was purified from the remaining solution by a NaOH-Acetone solvent extraction and further purified using anion exchange chromatography. The extracted Re and Os were then loaded onto Ni and Pt filaments, respectively, and analyzed for their isotopic composition using negative thermal-ionization mass spectrometry (NTIMS) (Creaser et al., 1991). The Re and Os isotope ratios were corrected for instrumental mass fractionation, as well as spike ($^{185}Re/^{187}Re$ standard values corrected to the accpeted $^{185}Re/^{187}Re$ value of 0.5974 (Gramlich et al., 1974)) and blank contributions. Procedural blanks for Re and Os in this study were 12 ± 3 pg/g and 0.07 ± 0.05 fg/g, respectively, with an $^{187}Os/^{188}Os$ value of 0.25 ± 0.15 (n = 4). The $^{187}Re/^{188}Os$ and $^{187}Os/^{188}Os$ uncertainties are

determined through full propagation of uncertainties, including those in weighing, mass spectrometer measurements, spike calibrations, blank abundances and reproducibility of standard values.

Age model and calculation of $^{187}Os/^{188}Os_i$

The age model (see below) is constructed using a previously published multigrain U-Pb age of 188.3 +1.5/-1 Ma (Hall et al., 1998) from approximately two meters below the lowest interval with carbon isotope data in the East Tributary section (Them et al., in review). The onset of the CIE is placed at 183.1 Ma, with a total duration of 300 kyr (Sell et al., 2014). Linear interpolation was used to calculate ages between the bentonites layers and also between the ages assigned for the Toarcian CIE. Sedimentation rates are also assumed to remain constant after the Toarcian CIE. The initial osmium isotopic composition of the oceans ($^{187}Os/^{188}Os_i$) was calculated using the following equation:

$$\frac{^{187}Os}{^{188}Os_i} = \frac{^{187}Os}{^{188}Os} - \left(\frac{^{187}Re}{^{188}Os} \times \left(e^{\left(1.666\times10^{-11}.a^{-1}\times age\times1000000\right)} - 1\right)\right) \quad (1)$$

This equation accounts for any ^{187}Os produced after deposition by the decay of ^{187}Re. As stated above, the age component was derived from U-Pb ages from this succession (Hall et al., 2004) and previously published dates for the age and duration of the Toarcian CIE (Sell et al., 2014).

The lowest two samples show values that are too unradiogenic to be primary (see Figure 4 in main text). The low calculated $^{187}Os/^{188}Os_i$ most likely is related to errors in the calculated age model. Very low sedimentation rates and the high error on the U-Pb multigrain age dates could produce erroneously low calculated $^{187}Os/^{188}Os_i$ and younger ages would result in more radiogenic $^{187}Os/^{188}Os_i$ values. Regardless, these two values do not change the robustness of the

whole dataset or our interpretations.

Estimating continental and oceanic contributions of osmium to the global oceans

The relative proportion of radiogenic continental and unradiogenic mantle input to the ocean may be calculated by using a simple two-component mixing model:

$$\left(\frac{^{187}Os}{^{188}Os}\right)_{sw} = \left(\frac{^{187}Os}{^{188}Os}\right)_{m} f + \left(\frac{^{187}Os}{^{188}Os}\right)_{rw} (1-f) \quad (2)$$

$$1.06 = 0.127\, f + 1.4(1-f)$$

$$f = 0.27$$

where $^{187}Os/^{188}Os_{sw}$ represents the osmium isotopic composition of sea water, $^{187}Os/^{188}Os_{m}$ represents the isotopic composition of mantle-derived osmium, $^{187}Os/^{188}Os_{rw}$ represents the isotopic composition of river water, and *f* represents the fraction of Os from the mantle source.

The modern seawater $^{187}Os/^{188}Os$ value of ~1.06 is a result of the greater influence from continental inputs ($^{187}Os/^{188}Os \approx 1.4$) of osmium over the other sources. This suggests that in the modern ocean, ~73% of $^{187}Os/^{188}Os_{sw}$ is derived from the input of osmium from rivers ($^{187}Os/^{188}Os_{rw}$) draining continental lithologies and ~27% is from alteration of oceanic crust and rivers draining mafic lithologies ($^{187}Os/^{188}Os_{m}$), with minor contributions from aeolian and cosmic dust that have not been considered here.

In order to better determine what processes could result in an osmium isotope excursion within the marine osmium inventory, we build a forward box model of the osmium cycle. We first determined the steady-state flux of osmium to the modern oceans using an estimate for the riverine input of 1800 moles of osmium per year and an ocean inventory of $7x10^7$ moles

(Peucker-Ehrenbrink & Ravizza, 2000 and references therein), which required the flux of osmium from the mantle of 650 moles per year. To maintain a mass balance, the flux of osmium being sequestered via sedimentation is 2450 moles per year. The change in the Os isotope composition of the ocean was calculated using the following equation:

$$\frac{\partial_N}{\partial_t} = \frac{F_{cont}(N_{SW} - N_{cont}) + F_m(N_{SW} - N_m)}{M_{SW}} \quad (3)$$

where ∂_N/∂_t represents the change in osmium isotopic composition with time, F_{cont} represents the flux in moles of osmium from rivers, N_{SW} represents the osmium isotopic composition of seawater, N_{cont} represents the osmium isotopic composition of rivers, F_m represents the flux in moles of osmium from the alteration of juvenile oceanic crust or hydrothermal input, N_m represents the osmium isotopic composition of this hydrothermal input, and M_{SW} represents the global inventory of oceanic osmium in moles.

Estimating continental and oceanic contributions of osmium to the Jurassic global oceans

In the following calculations, we set the overall Jurassic input of osmium to the oceans at the modern estimate of 2,450 moles per year (previously calculated using values from Peucker-Ehrenbrink and Ravizza, 2000 and the steady state model above). In order to reach the pre-Toarcian OAE steady-state $^{187}Os/^{188}Os_{sw}$ value of ~0.25, the continental and mantle inputs of osmium to the ocean had to be set at 237.65 moles per year ($^{187}Os/^{188}Os_{cont}$ = 1.4) and 2,212.35 moles per year ($^{187}Os/^{188}Os_m$ = 0.127), respectively. If the global input of osmium to the Jurassic oceans was much higher or lower than today, these fluxes can be scaled accordingly, in order to maintain isotopic steady state. Therefore, using these isotopic compositions, the mantle contribution of osmium was ~90% and the continental contribution was only ~10% before the

Toarcian OAE. As stated above, we are not including the flux of osmium from cosmic dust or aeolian dust since these are thought to be minor inputs to the ocean, and the cosmic flux is generally assumed constant (Peucker-Ehrenbrink, 1996).

We found several scenarios that can reproduce the Toarcian osmium isotope excursion recorded at the East Tributary study location. These included 1) transiently increasing the continental weathering flux, 2) transiently increasing the isotopic composition and magnitude of the continental weathering flux, 3) transiently decreasing the oceanic weathering flux. For all these solutions the transient change in osmium cycle was set at 100 kyrs, the approximate duration of the falling limb of the Os excursion (Sell et al., 2014). Additional sensitivity tests of the model were performed on scenarios that produced acceptable results (i.e. reproduced the magnitude and timing of the observed isotope excursion). For example, with scenario 1, increasing the flux of osmium from continents for 100 kyr from 237.65 moles/year to 1,500 moles/year reproduced the magnitude and timing of the observed isotope excursion. For scenario 2, changing the Os isotopic composition of the continental end-member from 1.4 to 2.0, and increasing the flux of continental-derived osmium from 237.65 moles/year to 800 moles/year for 100 kyr, also resulted in an acceptable solution (see discussion below about only changing the isotopic composition of the riverine flux). In scenario 3, we changed only the flux osmium being weathered from mantle materials from 2,212.35 moles per year to 0 moles per year, which resulted in a seawater $^{187}Os/^{188}Os$ value of 0.55. This scenario is unrealistic: the Os isotope values never reached the $^{187}Os/^{188}Os_i$ values of ~0.6, but more importantly, there is no reasonable explanation as to why the weathering of highly weatherable unradiogenic mafic materials (CAMP basalts, Karoo-Ferrar basalts, juvenile oceanic crust, etc.) would cease during the event.

It is also important to note that decreasing the M_{SW} inventory does not significantly change the increase in F_R that is necessary to cause the osmium isotope excursion.

Other scenarios produced acceptable numerical solutions, however these represent unlikely scenarios. For example, it is possible to reproduce the isotope excursion by changing only the isotopic composition of osmium entering the oceans from continents. However, this requires $^{187}Os/^{188}Os_r$ values to transiently increase from 1.4 to 5. The highest recorded modern riverine $^{187}Os/^{188}Os$ values were found within Mackenzie River basin at 3 – 4.5 and these compositions were isolated to only a few tributaries within the watershed (Huh et al., 2004). However, these values cause the Mackenzie River to be more radiogenic than the world river average $^{187}Os/^{188}Os$ of 1.4 (Huh et al., 2004). Therefore, it is highly unlikely that global $^{187}Os/^{188}Os_{cont}$ values increased to values over 2 during the T-OAE (Cohen et al., 2004).

With our model we also attempted to reproduce the osmium isotope excursion from Yorkshire to test whether plausible scenarios could result in that Os isotope record (SI Fig. 1) (Cohen et al., 2004). For example increasing the flux of osmium from continents from 237.65 moles/year to 5,500 moles/year for 100 kyr reproduces the magnitude and timing of the observed Yorkshire isotope excursion (increase of ~2,200%). Also, changing the Os isotopic composition of the continental end-member from 1.4 to 2.0, and increased the flux of continental-derived osmium from 237.65 moles/year to 2,100 moles/year for 100 kyr resulted in an acceptable solution (increase of ~800%). However, both of these values require an extremely large increase in the riverine flux to the ocean if the Yorkshire dataset is indicative of a global signal. Therefore, it is unlikely that this record reflects the global ocean $^{187}Os/^{188}Os$ and was probably modified by local/regional riverine inputs (McArthur et al. 2008).

References Cited for Supplementary Information

Cohen, A.S., Coe, A.L., Harding, S.M. & Schwark, L. Osmium isotope evidence for the regulation of atmospheric CO_2 by continental weathering. *Geology* **32**, 157– 160 (2004).

Cumming, V.M., Poulton, S.W., Rooney, A.D. & Selby, D. Anoxia in the terrestrial environment during the late Mesoproterozoic. *Geology* **41**, 583–586 (2013).

Esser, B.K. & Turekian, K.K. The osmium isotopic composition of the continental crust. *Geochim. Cosmochim. Acta* **57**, 3093–3104 (1993).

Gramlich, J.W., Murphy, T.J., Garner, E.L. & Shields, W.R. Absolute isotopic abundance ratio and atomic weight of a reference sample of rhenium. *J. Res. Nat. Bur. Stds.* **77A**, 691–698 (1973).

Hall, R., McNicoll, V., Gröcke, D., Craig, J. & Johnston, K. Integrated stratigraphy of the lower and middle Fernie Formation in Alberta and British Columbia, western Canada. *Riv. Ital. Paleon. Strat* **110**, 61– 68 (2004).

Huh, Y., Birck, J.-L. & Allègre, C.J. Osmium isotope geochemistry in the Mackenzie River basin. *Earth Plan. Sci. Lett.* **222**, 115–29 (2004).

McArthur, J.M., Algeo, T.J., van de Schootbrugge, B., Li, Q. & Howarth, R.J. Basinal restriction, black shales, Re-Os dating, and the Early Toarcian (Jurassic) oceanic anoxic event. *Paleoceanography* **23**, PA4217 (2008).

Peucker-Ehrenbrink, B. Accretion of extraterrestrial matter during the last 80 million years and its effect on the marine osmium isotope record. *Geochim. Cosmochim. Acta* **60**, 3187–3196 (1996).

Peucker-Ehrenbrink, B. & Ravizza, G. The marine osmium isotope record. *Terra Nova* **12**, 205–219 (2000).

Selby, D. & Creaser, R.A. Re-Os geochronology of organic rich sediments: an evaluation of organic matter analysis methods. *Chem. Geol.* **200**, 225–240 (2003).

Sell, B. *et al.* Evaluating the temporal link between the Karoo LIP and climatic—biologic events of the Toarcian Stage with high-precision U-Pb geochronology. *Earth Plan. Sci. Lett.* **408**, 48–56 (2014).

Smoliar, M.I., Walker, R.J. & Morgan, J.W. Re-Os ages of Group IIA, IIIA, IVA and IVB iron meteorites. *Science* **271**, 1099–1102 (1996).

Figure

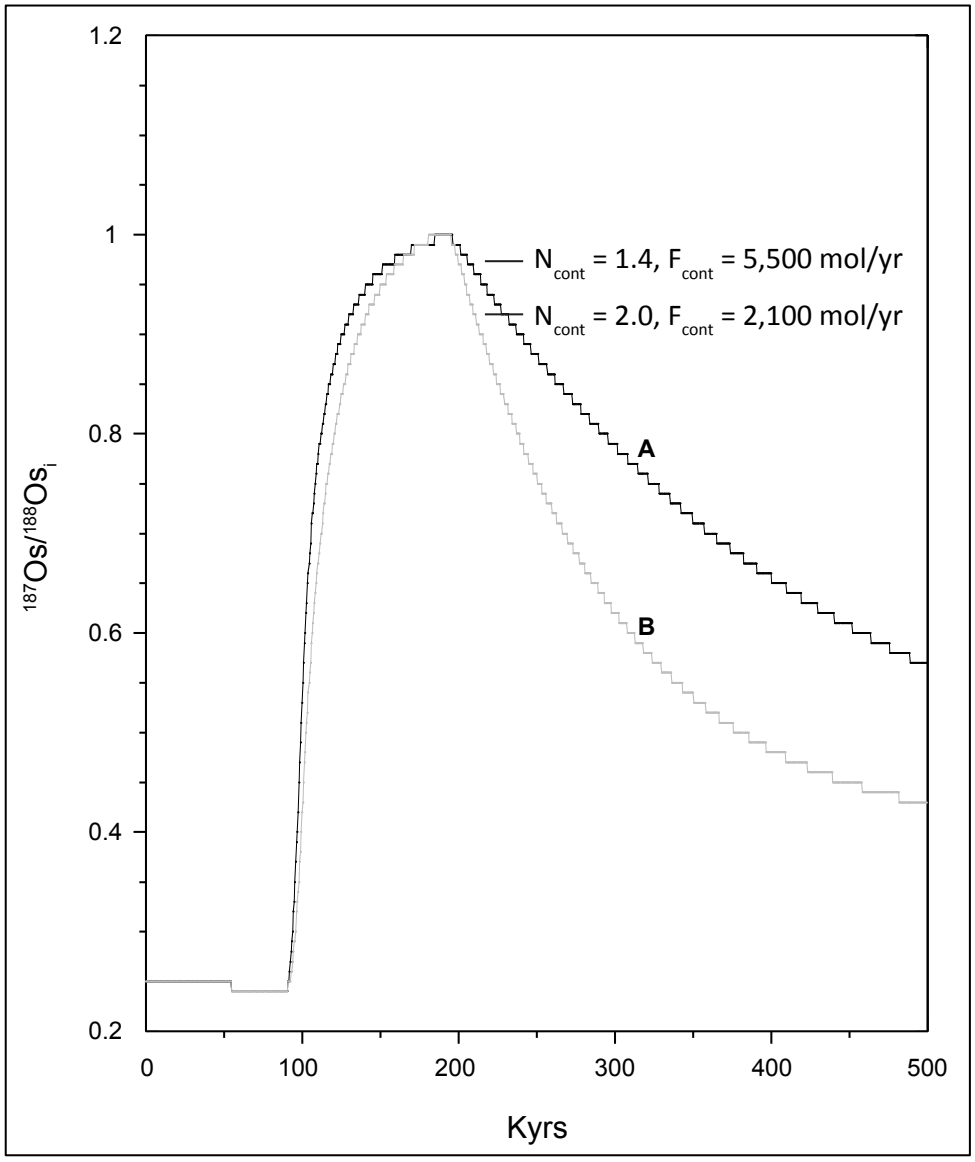
1.2
1
0.8
0.6
0.4
0.2
0
100
200
300
400
500
Kyrs
$^{187}Os/^{188}Os_i$
N_{cont} = 1.4, F_{cont} = 5,500 mol/yr
N_{cont} = 2.0, F_{cont} = 2,100 mol/yr
A
B

SI Figure 1: Examples of the modeled osmium isotopic composition of the ocean over the T-OAE using the Yorkshire dataset (Cohen et al., 2004) **A)** For this model run, the Os isotopic composition of river water was kept at 1.4 during the Toarcian OAE, and The flux of osmium from continents was increased by ~23x. This resulted in the seawater Os isotope values to increase to 1.0, which reproduces the observed geochemical data. **B)** Model run where the Os isotopic composition of river water was increased to 2.0 during the Toarcian OAE, and the flux of osmium from continents was increased by ~9x. This also reproduced the osmium isotope excursion from Yorkshire, UK. Both of these values represent unrealistic increases in continental weathering rates, if in fact the Yorkshire dataset represented global osmium isotopic signature.

Chapter 3.

Geochemical evidence for basin-wide carbon cycle and redox changes in eastern Panthalassa during the Toarcian Oceanic Anoxic Event

T.R. Them II [a, *], B.C. Gill [a], Darren R. Gröcke [b]

[a] Department of Geosciences, Virginia Polytechnic Institute and State University, Blacksburg, Virginia 24061, USA

[b] Department of Earth Sciences, Durham University, Science Laboratories, South Road, Durham, DH1 3LE, UK

[*] Corresponding author. Tel.: + 1-607-725-1208.
E-mail address: theo1085@vt.edu (T.R. Them II).

Formatted for *Earth and Planetary Science Letters*

Abstract

The Mesozoic oceanic anoxic events (OAEs) are defined by the stratigraphic appearance of organic-rich facies and their associated carbon isotope excursions (CIEs). In many instances, the stratigraphic and geochemical changes across OAEs suggest oxic conditions before the event, anoxia during, followed by oxic conditions. However, this binary progression of redox changes during these events is not universal; recent stratigraphic and geochemical evidence supports the view that marine redox conditions were very dynamic, both spatially and temporally, across the OAEs. In this study, we reconstruct the redox conditions of the Western Canada Sedimentary Basin (WCSB) during the Pliensbachian and Toarcian stages of the Early Jurassic including the Toarcian OAE (T-OAE). $\delta^{13}C_{org}$ values are used to correlate three sites representing a basin transect, and iron speciation, a local redox proxy, is used to assess water column redox dynamics. The WCSB was persistently anoxic during the entire study interval, and fluctuated between ferruginous and euxinic water column conditions. During the onset of the T-OAE, the two distal sites became ferruginous, whereas the proximal location remained euxinic. These distal sites became euxinic during the rising $\delta^{13}C_{org}$ limb of the negative Toarcian CIE. The WCSB remained euxinic for the remainder of the study interval (possibly late Toarcian to early Aalenian). These data suggest sulfate limitation during the early stages of the T-OAE, possibly a function of globally enhanced burial of pyrite. Furthermore, this dataset in the context of others supports the redefinition of the stratigraphic limits of the oceanic anoxic event.

1. Introduction

Oceanic anoxic events (OAEs) are intervals of widespread deposition of organic-rich facies, and are generally associated with carbon isotope excursions (CIEs) (Schlanger and

Jenkyns, 1976; Schlanger et al., 1987; Arthur et al., 1988; Jenkyns, 2010). The development of pervasive marine anoxia is thought to be a major driver of the enhanced burial and preservation of organic carbon across these intervals (Arthur et al., 1987). Also associated with these time intervals are environmental and biotic crises, which culminated in major extinction events (e.g., Erba, 2004; Takashima et al., 2006; Jenkyns, 2010). There were several OAEs during the Mesozoic Era, specifically in the Jurassic and Cretaceous (Takashima et al., 2006). To date, three global-scale OAEs have been described from Cretaceous sedimentary successions and one from the Jurassic, along with several regional-scale "OAEs" (e.g., Takashima et al., 2006) (Fig. 1).

Paleoclimate and paleoceanographic reconstructions of OAEs suggest rapid intervals of global warming followed by intervals of global cooling (Jenkyns, 2010 and references therein). Internal, geologically controlled mechanisms have been hypothesized to initiate the warming intervals and resultant biogeochemical feedbacks as the main driver of the cooling episodes (e.g., Jenkyns, 2010). The onset of OAEs is linked in time to the emplacement of large igneous provinces and release of massive amounts of greenhouse gases such as carbon dioxide (CO_2) and methane (CH_4) (Fig. 1; Takashima et al., 2006; Jenkyns, 2010). Increased global temperatures are thought to enhance the hydrologic cycle and together cause chemical weathering rates to increase, a process that consumes CO_2 (e.g. Kump et al., 2000; Jenkyns, 2010). Higher weathering and runoff also increases primary productivity in marine and terrestrial environments through the delivery of nutrients to nearshore environments (e.g., Tyrrell, 1999; Jenkyns, 2010). This leads to the development of anoxia and the burial of significant amounts of organic matter, which also consumes CO_2 (e.g., Jenknyns, 2010). Thus, both enhanced silicate weathering and organic matter burial lead to the sequestration of CO_2, a diminishing of the greenhouse effect and over time, and the demise of the OAE (e.g., Cohen et al., 2004; Jenkyns, 2010).

One of the defining features of OAEs is they have associated carbon isotope excursions (e.g., Arthur et al., 1987; Schlanger et al., 1987; Jenkyns, 2010). The negative CIE associated with the Toarcian OAE has been identified in all exogenic carbon reservoirs including organic carbon, carbonate carbon, and terrestrial materials such as fossil wood (Hesselbo et al., 2000) and is therefore thought to represent a global perturbation to the carbon cycle. Although early studies suggested a regional processes resulted in this CIE (Bailey et al., 2003; van de Schootbrugge et al., 2005; Wignall et al., 2006), the identification of the CIE in stratigraphic sections globally has shown that this was a global phenomenon (Al-Suwaidi et al., 2011; Caruthers et al., 2011; Gröcke et al., 2011; Izumi et al., 2012; Kemp and Izumi, 2014; Chapter 1, Them et al.). However, a recent study has casted doubt on the utility of the Toarcian CIE as a global chemostratigraphic marker because it was not identified in a stratigraphic section from Austria, which represents a distal environment in semi-restricted basin in Austria (Neumeister et al., 2015).

Carbon isotope excursions are commonly used to define and correlate OAEs as they represent a global summation of changes in the carbon cycle (e.g., Arthur et al., 1987; Schlanger et al., 1987; Tsikos et al, 2004; Jenkyns, 2010; Phelps et al., 2015 and references therein). However, this may not be an accurate measure of the timing of the development and demise of anoxia locally. For example, several relationships are observed in the Cretaceous OAEs between stratigraphic intervals containing the CIEs and deposition of organic-rich facies (see Phelps et al., 2015 and references therein for a detailed analysis of the Texas Comanche Platform and its environmental responses to the Cretaceous OAEs). The simple binary pattern of oxic to anoxic back to oxic conditions may not accurately describe the local and regional redox conditions

across the associated carbon isotope excursion(s) (e.g., Phelps et al., 2015; this study), and it is necessary to development a more holistic way of defining such events.

Qualitative evidence for the development of ocean anoxia during OAEs is the stratigraphic appearance of laminated (non-bioturbated), organic-rich facies (e.g., Savrda and Bottjer, 1987). In many locations, organic-lean strata above and below these OAE black shales contain sedimentary structures and levels of bioturbation that suggest deposition under oxygenated conditions (i.e., Bonarelli, OAE 2). Quantitative evidence for the oxygenation state of the local water column and potential global oceans can be tracked by specific redox-sensitive elements and their isotopic systems, such as iron, sulfur, molybdenum, rhenium, uranium, thallium, vanadium, and nitrogen (e.g., Tribovillard et al., 2006; Anbar and Rouxel, 2007; Jenkyns, 2010). It is also possible to detect organic compounds that were generated in the photic zone and under anoxic or euxinic conditions by certain microorganisms (e.g., green and purple sulfur bacteria) (Koopmans et al., 1996; Pancost et al., 2004; Bowden et al., 2006; French et al., 2014). Chlorobiaceae, which are anaerobic photoautrophic bacteria (a type of green sulfur bacteria), are known to produce isorenieratene, an easily identifiable biomarker. Another widely used biomarker for euxinia, okenone, is produced solely by photoautrophic purple sulfur bacteria of the Proteobacteria group. For example, both isorenieratene and okenone (or their degradation products) have been found in T-OAE strata in England, and therefore indicate the presence of photic zone euxinia (Bowden et al., 2006; French et al., 2014). However, utility of some of these proxies to detect past water column redox conditions can be limited as many of these geochemical systems and markers only reflect local redox conditions, and therefore extrapolation to global environmental change is not possible without investigating them in many different locations.

Sedimentary redox changes in time and space during the younger Cretaceous OAEs are generally better studied than during the Toarcian OAE. Ocean drilling has provided high-resolution deep-water records of these events, and combined with shallow-water records of epicontinental locations, has resulted in a better understanding the environmental controls and feedbacks associated with these OAEs. For example, during OAE 2 (~ 93.5 Ma), organic geochemical evidence suggests that the southern proto-North Atlantic was continuously euxinic (Damsté and Köster, 1998). A more recent, in-depth analysis of OAE 2 redox condition in the proto-North Atlantic basin noted significant variation in the oxygen state of the ocean both temporally and spatially (Owens et al., 2012). In their study, Owens et al. (2012) found that although the southern proto-North Atlantic remained euxinic, the redox state may have been heavily influenced by hydrothermal vent systems that supplied significant amounts of nutrients for bioproductivity (e.g., Jenkyns, 2010). On the other hand, the northern proto-North Atlantic fluctuated between oxic and anoxic intervals and the redox state was probably controlled by the input of materials from continental sources (Owens et al., 2012). Furthermore, at some locations there is evidence that marine anoxia was prevalent before the initiation of OAE 2 (e.g., Schlanger et al., 1987; van Bentum et al., 2009; Montoya-Pino et al., 2010), and euxinia was persistent well after the event (Owens et al., 2013). Another recent study suggests that continental weathering inputs of iron controlled the redox state of the water column in offshore Morocco during OAE 2, which fluctuated between ferruginous and euxinic conditions before and during the OAE (Poulton et al., 2015). Further, modeling evidence suggested that approximately 50% of the global oceans were anoxic during OAE 2 (Monteiro et al., 2012), but a more recent sulfur isotope study suggests that potentially only 5% was euxinic (Owens et al., 2013). Despite these

differing scenarios, a broad understanding of the redox dynamics of Cretaceous OAEs is apparent.

Geochemical records of redox changes across the T-OAE are almost entirely limited to successions deposited in the European Boreal-Tethyan region, with a notable exception of a succession from Japan. Molybdenum, rhenium, and thallium geochemical evidence from the Cleveland Basin in the United Kingdom suggest anoxic conditions during the T-OAE (Pearce et al., 2008; Nielsen et al., 2011). The presence of isorenieratene in this succession also suggests persistent euxinia within the photic zone (anoxic and sulfidic) in this basin (Pancost et al., 2004; French et al., 2014). Organic geochemical evidence from the Posidonia Black Shale in Germany and Italian successions also suggests anoxic and euxinic conditions during deposition (Farrimond et al., 1988; Schouten, et al., 2000; Frimmel et al., 2004; Pancost et al., 2004; Schwark and Frimmel, 2004; van Breugal et al., 2006). The sulfur isotopic composition of carbonate-associated sulfate (CAS) from multiple Boreal-Tethyan sections records a positive isotope excursion, suggesting the sulfur cycle was significantly perturbed during T-OAE as the lighter ^{32}S isotope was preferentially used during microbial sulfate reduction (MSR) (Gill et al., 2011). Modeling of these data suggests that the increased burial of pyrite sulfur occurred globally during the T-OAE as a function of the increased geographic extent of bottom water anoxia (Gill et al., 2011). Thallium isotopic evidence from Portugal suggests that the Lusitanian Basin remained oxic throughout the T-OAE (Nielsen et al., 2011). Multiproxy trace metal data from Japan suggests ephemeral episodes of anoxia during the T-OAE interval (Kemp and Izumi, 2014), but not as pervasive as demonstrated in the UK and Germany. Therefore, similar to the Cretaceous OAEs, there appear to be temporal and spatial differences in ocean oxygenation

across the T-OAE, with some regions experiencing pervasive euxinia and others remaining oxygenated, while still others experiencing ephemeral episodes of anoxia across the event.

In order to better assess the global and regional redox dynamics during the T-OAE is necessary to generate records from successions deposited in other oceans outside of the European Boreal-Tethyan seaway. Here, we present new carbon-isotope and iron speciation datasets from three sites that represent a basin transect in the Western Canada Sedimentary Basin (WCSB) that were deposited in northeastern Panthalassa (Fig. 2). Our geochemical record from a more marginal location indicates pervasive euxinia across the Toarcian OAE. However, the two deeper-water sections suggest ferruginous conditions during the onset of the Toarcian negative CIE, before eventually becoming euxinic.

2. Geological Setting

The Early Jurassic stratigraphy of the WCSB is composed of the mixed carbonate-siliciclastic units of the Fernie Formation. The Fernie Formation rests unconformably upon Triassic strata and represents pre-orogenic facies of the Canadian passive margin receiving sediment sourced from the east (Poulton et al., 1989, 1994; Price, 1994). During the Middle to Late Jurassic, the margin became active as allochthonous terranes collided with western North America, creating a foreland basin, and resulting in a dominant sediment source from the west (Poulton et al., 1989). However, some suggest that this transition occurred during the Early Jurassic, and it is purported that the Fernie Formation was deposited in the backbulge depozone related to the retro-arc foreland basin (McCartney et al., 2010 a,b; McCartney and Leier, 2011, 2012); another group suggests a fore-arc setting (Rohais et al., 2016).

The Early Jurassic Fernie Formation is comprised of several members: the more marginal carbonate-dominated Nordegg Member and the more basinal Gordondale, Red Deer, and Poker Chip Shale (PCS) members. The Nordegg Member crops out in the Rocky Mountain foothills and sparse ammonite biostratigraphy indicates it is Pliensbachian in age (e.g. Frebold, 1966; Poulton et al., 1989; Asgar-Deen et al., 2003). The Red Deer and PCS are also located in the outcrop belt along the Rocky Mountain foothills, and contain an abundant ammonite fauna that indicates Pliensbachian to earliest Toarcian in age (Frebold, 1957; Hall 1984, 1987; Hall et al., 1998; Them et al. in review). The Gordondale Member was proposed to formally represent the subsurface strata correlative to the exposed Nordegg and Red Deer members (Asgar-Deen et al., 2004), as there has been difficulty in correlating these units with one another (e.g., Riediger et al., 1990; Poulton et al., 1990). However, using a suite of techniques (gamma-ray log response, lithostratigraphy, biostratigraphy), Asgar-Deen et al. (2003, 2004) correlated subsurface wells with outcrop sections representing the Pliensbachian and Toarcian (Fig. 2). Finally, the PCS can be found in outcrops and in the subsurface and overlies all of the other members mention here and ammonite faunas from this unit indicate a Toarcian age (Asgar-Deen et al., 2003, Chapter 1, Them et al.).

In this study we present geochemical data from the drill cores of the Gordondale and Poker Chip members that cover the Pliensbachian-Toarcian interval (Asgar-Deen et al., 2003) and compare their geochemistry to that of an outcrop section of the Red Deer and Poker Chip members (Chapter 1, Them et al.). The East Tributary section of the Fernie Formation has been previously studied for it litho-, bio-, and chemostratigraphy (Hall et al., 1998; Asgar-Deen et al., 2003; Chapter 1, Them et al.). At this site, organic-rich carbonates and siltstones of the Pliensbachian to Toarcian Red Deer Member are overlain by the organic-rich mudstones of the

Toarcian PCS (Fig. 3). Stratigraphic ages were determined by high-resolution biostratigraphy of ammonites within this section (Hall et al., 1998; Chapter 1, Them et al.). At the base of this section, a multi-grain U-Pb age from a bentonite yielded an age of 188.3 +1.5/-1 Ma (Hall et al., 2004). The Toarcian CIE begins at the transition between the Red Deer and Poker Chip Shale members, representing both lithological and chemostratigraphic boundary (Chapter 1, Them et al.).

Drill cores 1-35-62-20W5 and 6-32-78-5W6 contain the Pliensbachian to lower Toarcian Gordondale Member, and have been correlated to outcrops of Red Deer and PCS (Asgar-Deen et al., 2004), including East Tributary. Each core contains mixed organic-rich calcareous mudstones and siltstones in the Gordondale Member, which are overlain by organic-rich calcareous mudstones of the PCS (Asgar-Deen et al., 2003), similar to the lithologic succession at East Tributary (Chapter 1, Them et al.).

In core 1-35-62-20W5, the dominant lithologies are also alternating organic-rich calcareous siltstones and mudstones (Fig. 4). The Gordondale Member ranges from the base of the core to 2029 m (Asgar-Deen et al., 2003); several bivalve beds are present (Asgar-Deen et al., 2003), along with two newly identified Pliensbachian ammonites (*Amaltheus* sp.) at 2033.1 and 2031.8 m. The PCS comprises 2029 m to the top (Asgar-Deen et al., 2003). This unit contains organic-rich calcareous mudstones, displacive and diagenetic carbonate cements, bivalves, an *Actractites* (a cephalopod fossil similar to a belemnite, but with an aragonitic rostrum), and an ammonite at 2027.1 m (Dactylioceratid) (Fig. 4; Asgar-Deen et al., 2003). In core 6-32-78-5W6, the dominant lithologies from the base of the core to 1221 meters are alternating organic-rich calcareous siltstones and mudstones (Fig. 5). From 1221 to 1219 m, the dominant lithology is an organic-rich mudstone, with a thin, organic-rich, silty mudstone capped

by a displacive carbonate fan around 1220.25 m. From 1219 to 1214.6 m, the dominant lithology is an organic-rich, laminated, calcareous siltstone. From 1214.6 to 1207 m, the dominant lithology is an organic-rich mudstone unit, representative of the PCS (e.g., Asgar-Deen et al., 2003), often with laminations present. Two ammonite-bearing and one *Actractites*-bearing horizons are present above 1219 m. At 1218 m and 1217.5 m the Early Toarcian ammonites *Harpoceras* cf. sp. *subplantanum* and *Orthodactylites* sp. have been identified, respectively (Asgar-Deen et al., 2003).

These sections represent an excellent chance to use the Toarcian CIE as an intra-basinal and a global chemostratigraphic marker; since these cores represent time-correlative, deeper-water facies to the East Tributary section, it is possible to reconstruct paleoceanographic dynamics across the T-OAE. Specifically, if redox variations change with paleo-water depth, and potentially temporally, then it should be possible to reconstruct the temporal and spatial extent of oxygenation within the basin.

3. Materials and Methods

3.1. Total organic carbon contents (TOC) and isotope compositions ($\delta^{13}C_{org}$)

Drill cores 6-32-78-5W6 and 1-35-62-20W5 of the Fernie Formation were described and sampled for geochemical analyses at the Core Research Centre in Calgary, Alberta, Canada. Sampling of the drill cores was conducted using a handheld Dremel tool with a diamond tip drill bit or a ball mill. Both hand samples and drill cores of the East Tributary site were collected (Them et al. in review for description of outcrop coring) and sampled with either a handheld Dremel tool with a diamond tip drill bit or a ball mill. To remove the carbonate fraction, several

milliliters of 2N HCl were added to ~0.1 g of powder and allowed to react for ~24 hours. The solution was rinsed until a neutral pH was obtained, and then the samples were dried in an oven.

$\delta^{13}C_{org}$ and total organic carbon (TOC) values of the carbonate-free sample residues were conducted on an Isotope Cube elemental analyzer connected to an Isoprime 100 gas source isotope-ratio mass spectrometer (IRMS) in the Sedimentary Geochemistry Isotope Laboratory in the Department of Geosciences at Virginia Tech. The isotope compositions of the samples were expressed in the standard delta (δ) notation as per mil deviations (‰) from Vienna Pee Dee Belemnite (VPDB) using the following equation:

$$\delta^{13}C = \left[\frac{\left[\frac{^{13}C}{^{12}C}\right]_{sample} - \left[\frac{^{13}C}{^{12}C}\right]_{standard}}{\left[\frac{^{13}C}{^{12}C}\right]_{standard}} \right] \times 1000 \qquad [1]$$

Samples were calibrated to the VPDB scale using international (IAEA-CH-6 and IAEA-CH-7) and commercial standards (Elemental Microanalysis wheat flour, sorghum flour, low organic soil, and urea). Long-term analytical precision for the $\delta^{13}C$ measurements is <0.1‰ based on replicated analyses on isotope standards: this provided a linear range in $\delta^{13}C$ between -48.66‰ and -10.42‰. Total organic carbon was obtained as part of the isotopic analysis using elemental standards (i.e., Acetanilide, 71.09% C). Approximately 66% of total samples (n = 86) from core 6-32-78-5W6 were replicated at least once. Approximately 98% of total samples (n = 57) from core 1-35-62-20W5 were replicated at least once. Average analytical uncertainty for replicated analyses (n = 113) was 0.07‰.

3.2. Iron Speciation Analyses

The relative amount of iron in each iron-bearing mineral phases (iron speciation) of fine-grained siliciclastic units can be used to indentify different redox conditions that were present within the water column of modern and ancient sediments (e.g., Poulton and Raiswell, 2002; Lyons and Severmann, 2006; Canfield et al., 2007; Poulton and Canfield, 2011). Specifically, the amount of iron found in highly reactive iron-bearing phases (Fe_{HR}; see Equation 2) can be quantified in order to determine redox conditions during deposition (e.g., Poulton and Canfield, 2011). The Fe_{HR} pool represents the iron available in phases that react with aqueous sulfide, which results in the formation of pyrite (e.g., Berner, 1984). The highly reactive iron pool (e.g., Poulton and Canfield, 2005) is defined as:

$$Fe_{HR} = Fe_{py} + Fe_{carb} + Fe_{ox} + Fe_{mag} \qquad [2]$$

where Fe_{py} represents iron hosted in the pyrite fraction; Fe_{carb} represents iron hosted in the calcite, siderite, and ankerite fractions; Fe_{ox} represents iron hosted in the ferrihydrite, lepidocrocite, goethite; and hematite fractions; and Fe_{mag} represents iron hosted in the magnetite fraction.

Modern and ancient marine siliciclastic sediments deposited under water column anoxia have a Fe_{HR}/Fe_T (Fe_T represents total iron in the sample and include both highly reactive and unreactive iron) value of >0.38, whereas sediments deposited under oxic conditions are generally below 0.22 (Raiswell et al., 2001; Poulton and Raiswell, 2002; Poulton and Canfield, 2011). This threshold is also true for carbonate-rich marine sediments; however, the utility of this proxy is most reliable when Fe_T values are > 0.5 wt. % (Clarkson et al., 2014). As Fe_T values often decrease basinward, the relative amount of Fe_{HR} may increase due to 1) a decrease in the iron

which is tied to clastic deposition from the margin 2) the scavenging of iron from the water column along the transit (Fig. 6; e.g., Raiswell and Canfield, 1998; Anderson and Raiswell, 2004; Lyons and Severmann, 2006; Severmann et al., 2008; Lyons et al., 2009). In this scenario, Fe(III) is reduced to Fe(II) in shallow marginal sediments, and this dissolved Fe(II) is transported within the chemocline to distal locations within the basin and reacts to form Fe(II) minerals phases in a process referred to as the iron shuttle (Fig. 6). Because the amount of pyrite that can be deposited in anoxic environments during the microbial reduction of sulfate (e.g., Berner, 1984) can vary, the amount of Fe_{py} to Fe_{HR} in each sample can help discern whether or not the water column was ferruginous (pyrite formation limited by available sulfides) or euxinic. Fe_{py}/Fe_{HR} values > 0.8 are indicative of euxinia, whereas Fe_{py}/Fe_{HR} values < 0.8 are indicative of ferruginous conditions (März et al., 2008; Poulton and Canfield, 2011).

In order to determine the relative amount of iron in each iron-bearing phase, the sequential extraction method of Poulton and Canfield (2005) was utilized. First, Fe_{carb} was liberated by the addition of a 10mL solution of sodium acetate and acetic acid, buffered to pH of 4. These samples were placed on a shaking table for 48 hours at 50° C and then centrifuged. Next, Fe_{ox} was liberated from the samples by the addition of a 10mL solution of sodium dithionite and sodium citrate, buffered to pH of 4. These samples were placed on a shaking table for two hours, and then centrifuged. Finally, Fe_{mag} was liberated by the addition of a 10mL solution of ammonium oxalate. These samples were placed on a shaking table for six hours, and then centrifuged. After each extraction, 100 μL of the supernatant was transferred to a new tube, followed by the addition of 4 mL of HEPES, ferrozine, and hydroxylamine HCl solution (i.e., Stookey, 1970) and allowed to react overnight. The supernatant was removed in the original

sample tubes before the next iron extraction. Iron concentrations were measured in a spectrophotometer and calculated by a matrix-matched standard curve.

Fe_{py} values were determined by chromium reduction methods of Canfield et al. (1986). For this procedure approximately 0.1 grams of powder was added to a three-neck flask, which was placed on a specialty distillation line. Following the purging of headspace with nitrogen gas a solution of 40 mL of 1M chromous chloride and 20 mL of 6N HCl was added to the flask, and then allowed to react for two hours while heating under the nitrogen atmosphere. Any volatized sulfide quantitatively reacted with a zinc acetate solution to form zinc sulfide. Later, silver nitrate was added to this solution, which converted the zinc sulfide to silver sulfide. The amount of sulfide in the sample was then determined by gravimetry after filtration and drying of the silver sulfide. The amount of pyrite iron hosted in the original sample was then stoichiometrically calculated from the amount of extracted sulfide.

For the determination of Fe_T approximately 0.2 grams of powder was ashed at 900° C for 6-8 hours to remove any organic matter and other volatile phases. Approximately 0.06-0.1 grams of powder was then reacted with 4 mL of 12N HCl, and then placed in sealed Savillex digestion vessels on a hot plate and boiled for 36-48 hours (Aller et al., 1986). The sample and solution were added to centrifuge tubes and centrifuged. After centrifugation, 100 μL of the supernatant was transferred to a new tube and the same technique was used to measure iron concentrations using a spectrophotometer as stated previously.

4. Results

4.1. Total organic carbon contents (TOC) and isotope compositions ($\delta^{13}C_{org}$)

The Toarcian CIE has previously been identified at the East Tributary section (Fig. 3; Chapter 1, Them et al.). There is a long-term $\delta^{13}C_{org}$ increase from -28.5 to -27.0‰ (representing the Pliensbachian Margaritatus and Spinatum zones and Toarcian Tenuicostatum Zone) at the base to 11.26 m, followed by an abrupt 3‰ decrease at the Serpentinum Zone (Them et al.). $\delta^{13}C_{org}$ values approach -30.5‰ over the next ~1.6 m, before returning the ~ -27.0‰ over the next 3.5 meters. This represents the Toarcian CIE, as basal Toarcian ammonites occur more than a meter below this interval (Chapter 1, Them et al.). $\delta^{13}C_{org}$ values approach -27.5‰ until the top of the section, and the boundary between the Serpentinum and Bifrons zones occurs at 16.2 m (Chapter 1, Them et al.). TOC values in the Red Deer Member range from ~1.4 – 7.6% (average of 4.0%) and the PCS values range from 0.3 – 6.1% (average TOC of 3.2%) (Fig. 3).

The $\delta^{13}C_{org}$ values in core 1-35-62-20W5 (Fig. 4) display a long-term increase from -30.5 to -27.4‰, at the base to ~2029 m. Within this section, short-term $\delta^{13}C_{org}$ increases occur from 2037 – 2036 m and 2031.5 – 2030.5 m. This long-term increase is followed by a 3‰ decrease to -30.6‰ over a few decimeters (most negative value at 2028.5 m), before increasing to -26.5‰ to the top of the core. This upper interval represents the Toarcian CIE. TOC values range from 1 – 15% (Fig. 4). However, TOC values increase at the Gordondale-PCS boundary, which is approximately 0.5 m below the onset of the Toarcian CIE.

Several $\delta^{13}C_{org}$ trends are prominent in core 6-32-78-5W6 (see Fig. 5). $\delta^{13}C_{org}$ values decrease from -28 to ~ -30‰ from the base of the core to ~1223.5 m, followed by a positive $\delta^{13}C_{org}$ trend back to - 28‰ until 1220 m. $\delta^{13}C_{org}$ values decrease then decrease to -30‰, over

the next meter, before a larger decrease to -32‰. $\delta^{13}C_{org}$ values then increase before reaching -28‰ at ~1218 m. This large negative CIE represents the Toarcian CIE. A long-term $\delta^{13}C_{org}$ decrease occurs from 1218 m to the top of the core. TOC values range from 1 – 18% during the study interval (Fig. 5). This range is also observed from the base of the core to the Toarcian CIE, before staying between 5 – 10% during the CIE. TOC values slowly increase from the end of the CIE until the top of the core. There are two ammonites that were previously identified in this core (Asgar-Deen et al., 2003). *Orthodacylites* sp. is assigned to the Kanense Zone of western North America, and *Harpoceras* sp. cf. *subplanatum* is known to only occur in the Bifrons Zone of Europe and Russia or Plantula Zone of western North America (Howarth, 1978; Jakobs, 1997). However, the second ammonite, *Harpoceras* sp. cf. *subplanatum*, may have been misidentified, and is instead *Cleviceras exaratum* (A. Caruthers, pers. comm.) If this is the case, the Planulata Zone may be located higher in the core, as *C. exaratum* is found only within the Kanense Zone in British Columbia (Jakobs et al., 1994; Caruthers et al., 2011) and at East Tributary in Alberta (Chapter 1, Them et al.).

An interesting feature regarding the $\delta^{13}C_{org}$ records in this basin is their absolute magnitudes. In the most proximal location (East Tributary), $\delta^{13}C_{org}$ values before and after the Toarcian CIE are ~ -27.0‰ (Fig. 3). The most negative $\delta^{13}C_{org}$ values during the OAE approach -31‰, but generally stay at ~ -30.5‰. In core 1-35-62-20W5, $\delta^{13}C_{org}$ values before the CIE are -27.5‰, -30.6‰ during the CIE, and rise to -26.5‰ at the end (Fig. 4). In core 6-32-78-5W6, pre-CIE $\delta^{13}C_{org}$ values are either -28‰ or -29.2‰, which is dependent upon where the initiation of the CIE is placed, and $\delta^{13}C_{org}$ values are ~ -32‰ during the most extreme part of the CIE before rising to -28‰ at the end of the CIE (Fig. 5).

4.2. Iron Speciation

At the East Tributary section, Fe_{HR} values are dominated by pyrite and are ~ 1 wt. % before the CIE, before increasing to 1.5 – 2% at the onset of the CIE, and then increasing to 2 – 3.5% until the top of the section (Fig. 7). The Fe_T wt. % follows the same pattern as Fe_{HR}, but have a maximum of 4 wt % (Fig. 7). Fe_{HR}/Fe_T values are all above 0.4, with most data points between 0.7 and 0.8 (Fig. 3). Fe_{py}/Fe_{HR} values are generally above 0.8, with the only two values less than 0.8 in the Red Deer Member. Fe_{py}/Fe_{HR} values stay near 0.8 at the onset of the Toarcian CIE, then increase to ~0.9 during the remainder of the CIE, before decreasing slowly to ~0.8 near the top of the section (Fig. 3).

Similar to East Tributary, core 1-35-62-20W5 Fe_{HR} values are dominated by pyrite and are ~ 1 wt. % before the CIE, before increasing to ~ 2% at the onset of the CIE (Fig. 8). The Fe_T wt. % follows the same pattern as Fe_{HR}, but have a maximum wt. of ~ 3.5% (Fig. 8). Fe_{HR}/Fe_T values are all above 0.4, with the Gordondale values mostly near 1 and the PCS values between 0.45 and 1 (Fig. 4). The Gordondale Fe_{py}/Fe_{HR} values range from 0.6 – 0.9, and generally increase upward. The PCS Fe_{py}/Fe_{HR} values increase from 0.65 to 0.9 across the CIE and do not go below 0.8 once they cross this threshold (Fig. 4).

In core 6-32-78-5W6, Fe_{HR} values are also dominated by pyrite and range from ~ 0.5 – 1.5% before the CIE, and do not change during the CIE (Fig. 9). Like the two previous sites, Fe_T wt. % follows the same pattern as Fe_{HR}, have a maximum wt. of ~ 3.5 %, but are highest near the top of the core (Fig. 9). Fe_{HR}/Fe_T values are all above 0.4, with most data points near 0.8 (Fig. 5). The Toarcian CIE values stay consistently around 0.7. The Gordondale Fe_{py}/Fe_{HR} values remain around 0.8, before decreasing to ~0.7 at the onset of the Toarcian CIE. These values increase to

0.85 during the return to more positive $\delta^{13}C_{org}$ values at the end of the CIE, followed by Fe_{py}/Fe_{HR} values that stay around 0.8 until the top of the core (Fig. 5).

5. Discussion

5.1. Early Jurassic carbon isotope variations in the WCSB

The Toarcian CIE has now been identified in proximal and distal settings in Panthalassa, and this represents one the first carbon-isotope basin transect records of this interval (Fig. 10), and the only outside of Europe. This new $\delta^{13}C_{org}$ correlation between drill core sections adjusts one derived from well logs (Fig 10; Asgar-Deen et al., 2003). A recent carbon isotope study of distal Toarcian unit in Austria questioned the utility of the Toarcian CIE as a global marker because it was not identified (Neumeister et al., 2015). At this section, $\delta^{13}C_{org}$ values decrease during what is interpreted as late Pliensbachian *A. margaritatus* ammonite subzone before returning to more positive values during the *H. falciferum* subzone. However, the findings from the WCSB and elsewhere (e.g., Hesselbo et al., 2000; Al-Suwaidi et al., 2011; Caruthers et al., 2011; Hesselbo and Pieńkowski, 2011; Chapter 1, Them et al.) suggest that the CIE was ubiquitous, and the Toarcian CIE is a robust chemostratigraphic marker. Potential reasons that the CIE was not identified at the Austrian site could be related to the incompleteness of the geological record (i.e., the Toarcian CIE interval was not preserved), the interpreted ages of the sampled strata are not correct (the age estimates were based off of a lithostratigraphic correlation and a single ammonite find in that section), the sampling resolution was too low (i.e., the Toarcian CIE interval occurred between samples) or that local oceanographic processes overprinted the global $\delta^{13}C$ signal. However, this last scenario is highly unlikely, considering

that local carbon cycling would have to have been vigorous enough to modify the global signal for several hundred thousand years.

It is evident that the morphology of the WCSB $\delta^{13}C_{org}$ records is different at each site (Fig. 10), which was likely driven by variations in sedimentation rates and erosional hiatuses within each section (e.g., Trabucho-Alexandre, 2014). However, at each site, the onset of the negative CIE is very condensed relative to many of the Boreal-Tethyan records (e.g., Kemp et al., 2005; Hesselbo et al., 2007; Bodin et al., 2011; Hermoso et al., 2012). The mean TOC values during the Toarcian CIE from the most proximal to the most distal location are 3.2%, 5.3%, and 7.2%, respectively (Figs. 3-5). The greater thicknesses of the most proximal East Tributary section and intermediate depth core 1-35-62-20W5 are most likely indicative of higher sedimentation rates, relative to the thinner distal core 6-32-78-5W6, and not necessarily caused by erosional hiatuses (e.g., Trabucho-Alexandre). On another note, the long-term negative $\delta^{13}C_{org}$ trend after the CIE seen in core 6-32-78-5W6 is broadly similar to that observed from the Mochras Borehole in Wales (Jenkyns et al., 2001) but is not observed at East Tributary (Fig. 3).

Overall our data show that there was a 1‰ gradient across our depositional transect in the WCSB. This gradient between the most proximal and most distal (and probably deeper) sections may have been controlled by several different factors (e.g., Hayes et al., 1999; Freeman, 2001 and references therein). These factors may be related to changing organic matter sources, local hydrology, primary productivity, and temperature (Hayes et al., 1999). If there was prominent upwelling within this basin, then the dissolved inorganic carbon (DIC) pool of the cool, upwelling water mass would have been relatively depleted in ^{13}C, which could have resulted in intrabasinal $\delta^{13}C_{DIC}$ differences. Any primary production in this water mass would have resulted in slightly more negative $\delta^{13}C_{org}$ values relative to non-upwelling sites. Changes in organic

matter composition (ratio of bacteria vs. eukaryotes; marine vs. terrestrial organic matter) can also result in intrabasinal $\delta^{13}C_{org}$ differences (e.g., Freeman, 2001; Hayes, 2001 and references therein). Regardless, whatever controlled the absolute $\delta^{13}C_{org}$ differences in the WCSB, the magnitude of the Toarcian CIE was similar at each site (Figs. 3-5, 10), suggesting a similar control on the WCSB (and global) $\delta^{13}C_{DIC}$ pool. The absolute magnitude of change in the WCSB bulk $\delta^{13}C_{org}$ samples is smaller than what has been observed in most other locations (up to -8‰; e.g., Hesselbo et al., 2000; Kemp et al., 2005; Caruthers et al., 2011; Hermoso et al., 2012, Suan et al., 2011). Compound-specific $\delta^{13}C_{org}$ records suggest the absolute global magnitude of the Toarcian CIE was only -3‰ to -4‰ (Schouten et al., 2000; van Breugal et al., 2006; French et al., 2014; Suan et al., 2015). Considering these Alberta $\delta^{13}C_{org}$ values vary from -3‰ to -4‰ relative to the pre-CIE values, this suggests minimal changes in organic matter sources that might alter the magnitude of the bulk $\delta^{13}C_{org}$ composition.

5.2. Early Jurassic redox changes in the WCSB

The Fe_{HR}/Fe_T values at each site suggest that during the study interval (Pliensbachian to Toarcian), anoxia was pervasive within the WCSB (Figs. 3-5). Pre-OAE samples, Pliensbachian to earliest Toarcian suggest variable ferruginous ($Fe_{py}/Fe_{HR} < 0.8$) to euxinic ($Fe_{py}/Fe_{HR} > 0.8$) conditions (Figs. 3-5). The Fe_{py}/Fe_{HR} values at East Tributary range from 0.74 – 0.92, suggesting euxinic conditions during the T-OAE and afterwards (Fig. 3). In fact, euxinia remains pervasive into the middle Toarcian Bifrons Ammonite Zone. In both drill cores, the iron speciation data suggest that distal (deeper) regions became ferruginous just before and during the onset of the Toarcian CIE. In core 1-35-62-20W5, the water column was ferruginous during the deposition of the PCS, slightly before the onset of the Toarcian OAE. At these two locations, there is a transition back to euxinic conditions when $\delta^{13}C_{org}$ values reach -29.5‰ on the rising limb. In

core 6-32-78-5W6, the Fe_{py}/Fe_{HR} values remain around 0.8 well after the Toarcian CIE (the top of core 1-35-62-20W5 is unfortunately at the end of the Toarcian CIE).

Another notable trend in the iron dataset is that Fe_T values decrease from proximal (Fig. 7) to distal (Figs. 8-9) areas of the WCSB during the T-OAE, which is expected, as the siliciclastic flux should be highest in nearshore environments. The mean Fe_T value at East Tributary during the T-OAE is 3.47, and decreases in distal locations core 1-35-61-20W5 (Fe_T = 2.38) to core 6-32-78-5W6 (Fe_T = 1.61). Furthermore, from proximal to distal locations, there is enrichment in Fe_{HR} relative to Fe_T, which may point to the iron shuttle as previously discussed (e.g., Raiswell and Canfield, 1998; Anderson and Raiswell, 2004; Lyons and Severmann, 2006; Severmann et al., 2008; Lyons et al., 2009). The mean Fe_{HR}/Fe_T value at East Tributary during the T-OAE is 0.74, is approximately the same in core 1-35-61-20W5 (Fe_{HR}/Fe_T = 0.73), and much higher in core 6-32-78-5W6 (Fe_{HR}/Fe_T = 0.82) (Figs 7-9).

Overall these data offer new insights into redox conditions on the eastern Panthalassa Ocean margin during the Early Jurassic. During the entire study interval in the WCSB, the iron speciation data suggest pervasive anoxia. Thus, the T-OAE interval is not unique relative to pre- and post-OAE redox conditions. However, the most proximal location (East Tributary) remained euxinic across the T-OAE and the two distal locations suggest ferruginous conditions during the onset, before becoming euxinic towards the end of the T-OAE. Again, the major controls on pyrite formation are the abundance of labile organic matter and sulfate available for MSR (Berner, 1984). In each site, high TOC values suggest that organic matter abundances were not the limiting factor with regards to pyrite formation, although if sedimentation rates were extremely low then this remains a possibility.

The sulfur isotopic composition of CAS, a proxy for seawater sulfate, suggests that the sulfate concentrations of the oceans were significantly reduced during the T-OAE due to increased pyrite burial (Gill et al., 2011). A numerical model estimates that the Toarcian marine sulfate concentrations were 4 to 8 mM, which could be decreased if pyrite burial enhanced on a global scale (Gill et al., 2011). As the European CAS data suggest a major decline in marine sulfate concentrations, it is quite likely that high pyrite burial rates within the WCSB exasperated this decline locally. Sulfate concentrations less than 5mM begin to affect MSR rates and subsequently rates of pyrite formation and burial (Berner, 1984). If upwelling waters in the WCSB caused higher productivity in these more distal locations, then it is possible that MSR rates were also much higher and resulted in sulfate limitation and ferruginous conditions. Alternatively, if the Panthalassa water mass was sources from the south, then the supply of sulfate to the potentially shallower location (East Tributary) was great enough to sustain euxinic conditions. However, in the northern locations within the basin, the supply of sulfate may not have been high enough to sustain enhanced burial of pyrite, so the water column became ferruginous. This may have been caused by the semi-restricted nature of the basin, as East Tributary may have been closer to the connections with the open Panthalassa.

Pyrite formation is limited in euxinic conditions due to iron limitation (i.e., aqueous sulfide is in excess to iron). As the vast majority of samples were deposited in euxinic conditions ($Fe_{py}/Fe_{HR} > 0.8$), the WCSB was generally iron-limited during the Pliensbachian and Toarcian. This suggests relatively low siliciclastic input to the WCSB, which is expected as the updip, time-equivalent facies represents the carbonate platform of the Nordegg Member (Poulton et al., 1989; Asgar-Deen et al., 2003; 2004). During ferruginous conditions, either sulfate or organic carbon limits pyrite formation (Berner, 1984). For reasons stated above, TOC values were

elevated during the study interval as this basin was very productive, and any ferruginous conditions were most likely controlled by the availability of sulfate. In general, before the Toarcian CIE, the WCSB fluctuated between intervals of iron and sulfate limitation. At the onset of the CIE, more distal locations became sulfate limited, before the whole basin became iron limited towards the end and after the CIE.

Another iron speciation study from the Yorkshire Coast also suggests that at the onset of the T-OAE, ferruginous conditions were present in the Cleveland Basin (Salem, 2013, PhD thesis). In the *C. exaratum* subzone, euxinic conditions were noted, and Fe_{py}/Fe_{HR} values stayed around 0.8, suggesting variability between ferruginous and euxinic conditions (Salem, 2013). A wide spread of $\delta^{34}S$ values of sedimentary sulfides may also be a function of sulfate limitation during the T-OAE, perhaps a consequence of increased global pyrite burial during this interval (Gill et al., 2011). However, this basin may have also been restricted (e.g., McArthur et al., 2008), which may have aided in sulfate limitation due to poor connections with the open ocean (Gill et al., 2011)

Based on our data, water masses within the WCSB were oxygen-poor during the Pliensbachian and Toarcian, and not confined to the interval defined by the CIE. As noted before, the records of other OAEs have been shown to display a variety of local redox changes over the interval that contains these events as defined by the CIE. For example, the record of OAE 2 shows a variety of local redox changes before and after the associated CIE (van Bentum et al., 2009; Montoya-Pino et al., 2010; Owens et al., 2013; Poulton et al., 2015), with some evidence suggesting astronomical pacing of water column redox changes (Poulton et al., 2015). Furthermore, the WCSB is not the only basin during the Toarcian where organic-rich deposition

and anoxic conditions persisted after the CIE interval (e.g., Brumsack, 1991; Jenkyns and Clayton, 1997; Schouten et al., 2000).

There are several implications from this new WCSB dataset and previous work (see above). The dynamism of redox changes, both spatially and temporally, before, during, and after an OAE shows no particular pattern. Some locations remain oxygenated throughout the entire interval (e.g., T-OAE, Nielsen et al., 2011), whereas others were anoxic (e.g., van Bentum et al., 2009; Montoya-Pino et al., 2010; Owens et al., 2013; Poulton et al., 2015; this study). The accompanied carbon isotope excursion may in fact be a useful indicator of an OAE, but it does not define when anoxia occurred. As such, it might be possible to determine the OAE interval using geochemical systems that can only be perturbed through global processes, although proving that such system(s) exist is difficult. Interestingly, at the East Tributary site, rhenium abundances decrease drastically during the CIE, relative to pre- and post-CIE values. This was interpreted to represent the global drawdown of the seawater rhenium inventory during the T-OAE interval, with localized drawdown being the mechanism behind the enrichments (Chapter 2, Them et al.). Furthermore, osmium isotope data from this section suggest an increase in continental-derived materials to the global ocean during the T-OAE (Chapter 2, Them et al., in prep). Also, the $^{187}Os/^{188}Os$ values suggest greater amounts of continental weathering after the T-OAE relative to before the T-OAE (Chapter 2, Them et al., in prep), which may have sustained high productivity in the WCSB, as observed in the high TOC values (Figs. 3-5). Geochemical system such as these may help to define what processes are causing organic productivity within a basin, and also why some basins may remain organic-rich after an OAE.

6. Conclusions

Here we show that the CIE associated with the T-OAE can be found in stratigraphic sections across the WCSB, making it the first high-resolution carbon-isotope basin transect outside of Europe. These findings add more evidence that the Toarcian CIE was in fact a global ocean phenomenon, and a robust chemostratigraphic marker. The new iron speciation data presented here represent one of the first redox proxy studies outside of the European Boreal-Tethyan region and the first from Eastern Panthalassa. These data suggest that more proximal locations were euxinic during and after the T-OAE, whereas the distal locations became ferruginous during the onset of the OAE, before transitioning to euxinic conditions during the rising limb of the CIE. The global drawdown of sulfate during the onset of the event may have caused sulfate limitation within the WCSB, which may have also have also been related to less vigorous ocean circulation and mixing with open Panthalassa during the event. Notably, water column anoxia was pervasive before and after the Toarcian CIE in the WCSB. As observed for other OAEs, the record of the T-OAE shows the more dynamic nature of marine oxygenation than previously considered. As our understanding of the redox history during these events is refined it may be necessary to eventually redefine what constitutes an "oceanic anoxic event."

Acknowledgements

We thank the National Science Foundation (grant EAR-1324752 to B.C.G.) for supporting this research. T.R.T. would also like to thank the Geological Society of America, Society for Sedimentary Geology, and Virginia Tech Department of Geosciences graduate student grant programs for funding. Thanks to Hannah Grove, Paige Bamonto, Emma Tulsky, Selva Marroquín, and Angela Gerhardt for their help in the lab work and field work portions of the study.

7. References

Aller, R.C., Mackin, J.E., and Cox, R.T. Jr, 1986, Diagenesis of Fe and S in Amazon inner shelf muds: apparent dominance of Fe reduction and implications for the genesis of ironstones. Cont. Shelf Res. 6, 263–289.

Al-Suwaidi, A.H., Angelozzi, G.N., Baudin, F., Damborenea, S.E. Hesselbo, S.P., Jenkyns, H.C., Manceñido, M.O., and Riccardi, A.C., 2010, First record of the Early Toarcian Oceanic Anoxic Event from the Southern Hemisphere, Neuquén Basin. Arg. J. Geol. Soc. [Lon.] 167, 633–636.

Al-Suwaidi, A.H., Angelozzi, G.N., Baudin, F., Damborenea, S.E. Hesselbo, S.P., Jenkyns, H.C., Manceñido, M.O., and Riccardi, A.C., 2010, First record of the Early Toarcian Oceanic Anoxic Event from the Southern Hemisphere, Neuquén Basin. Arg. J. Geol. Soc. [Lon.] 167, 633–636.

Anbar, A.D., and Rouxel, O., 2007, Metal Stable Isotopes in Paleoceanography. Ann. Rev. Earth Plan. Sci. 35, 717–746.

Anderson, T.F., and Raiswell, R., 2004, Sources and mechanisms for the enrichment of highly reactive iron in euxinic Black Sea sediments. Am. J. Sci. 304, 203–233.

Arthur, M.A., Schlanger, S.O., and Jenkyns, H.C., 1987, The Cenomanian-Turonian Oceanic Anoxic Event, II. Paleoceanographic controls on organic-matter production and preservation. Geol. Soc. Lon. Spec. Pub. 26, 401–420.

Arthur, M.A., Dean, W.E., and Pratt, L.M., 1988, Geochemical and climatic effects of increased

marine organic carbon burial at the Cenomanian/Turonian boundary. Nature 335, 714–717.

Asgar–Deen, M., Hall, R., Craig, J., and Riediger, C., 2003, New biostratigraphic data from the Lower Jurassic Fernie Formation in the subsurface of west-central Alberta and their stratigraphic implications. Can. J. Earth Sci. 40, 45–63.

Asgar-Deen, M., Riediger, C., and Hall, R., 2004, The Gordondale Member: designation of a new member in the Fernie Formation to replace the informal "Nordegg Member" nomenclature of the subsurface of west-central Alberta. Bull. Can. Petr. Geol. 52, 201–214.

Bailey, T.R., Rosenthal, Y., McArthur, JM, van de Schootbrugge, B., and Thirlwall M.F., 2003, Paleoceanographic changes of the Late Pliensbachian-Early Toarcian interval, a possible link to the genesis of an Oceanic Anoxic Event. Earth Planet. Sci. Lett. 212, 307–320.

Berner, R.A., 1984, Sedimentary pyrite: An update*. Geochim. Cosmochim. Acta 48, 605–615.

Berner, R.A., and Raiswell, R., 1983, Burial of organic carbon and pyrite sulfur in sediments over Phanerozoic time: a new theory. Geochim. Cosmochim. Acta 47, 855–862.

Berner, R.A., and Raiswell, R., 1984, C/S method for distinguishing freshwater from marine sedimentary rocks. Geology 12, 365–368.

Bowden, S.A. *et al.* Compositional differences in biomarker constituents of the hydrocarbon, resin, asphaltene and kerogen fractions: An example from the Jet Rock (Yorkshire, UK). Org. Geoch. **37**, 369-383 (2006).

Brumsack, H.-J., 1991, Inorganic geochemistry of the German 'Posidonia Shale': palaeoenvironmental consequences. Geol. Soc. Lon. Spec. Pub. 58, 353–362.

Canfield, D.E., Raiswell, R., Westrich, J.T., Reaves, C.M., and Berner, R.A., 1986, The use of chromium reduction in the analysis of reduced inorganic sulfur in sediments and shales. Chem. Geol. 54, 149–155.

Caruthers, A.H., Gröcke, D.R., and Smith, P.L., 2011, The significance of an Early Jurassic (Toarcian), carbon-isotope excursion in Haida Gwaii (Queen Charlotte Islands), British Columbia, Canada. Earth Planet. Sci. Lett. 307, 19–26.

Damsté, J.S.S., and Köster, J., 1998, A euxinic southern North Atlantic Ocean during the Cenomanian/Turonian oceanic anoxic event. Earth Planet. Sci. Lett. 3-4, 165–173.

Erba, E., 2004, Calcareous nannofossils and Mesozoic oceanic anoxic events. Mar. Micro. 52, 85–106.

Farrimond, P., Eglington, G., Brassell, S.C., and Jenkyns, H.C., 1988, The Toarcian black shale event in northern Italy. Org. Geochem. 13, 823–832.

Freeman, K.H., 2001, Isotopic Biogeochemistry of Marine Organic Carbon, Rev. Min. Geochem. 43, 579–605.

Frebold, H., 1957, The Jurassic Fernie Group in the Canadian Rocky Mountains and Foothills. Geol. Sur. Can. Mem. 287.

Frebold. H, 1966, Upper Pliensbachian beds in the Fernie Group of Alberta. Geol. Sur. Can. 66-

27.

French, K.L., Sepúlveda, J., Trabucho-Alexandre, J., Gröcke, D.R., and Summons, R.E., 2014, Organic geochemistry of the early Toarcian oceanic anoxic event in Hawsker Bottoms, Yorkshire, England. Earth Planet. Sci. Lett. 390, 116–127.

Frimmel, A., Oschmann, W., and Schwark, L., 2004, Chemostratigraphy of the Posidonia Black Shale, SW Germany: II. Assessment of extent and persistence of photic-zone anoxia using aryl isoprenoid distributions. Chem. Geol. 206, 231–248.

Gill, B.C., Lyons, T.W., and Jenkyns, H.C., 2011, A global perturbation to the sulfur cycle during the Toarcian Oceanic Anoxic Event. Earth Planet. Sci. Lett. 312, 484–496.

Gröcke, D.R., Hori, R.S., Trabucho-Alexandre, J., Kemp, D.B., and Schwark, L., 2011, An open record of the Toarcian oceanic anoxic event. Sol. Earth Discuss. 2, 245–257.

Hall R.L., Poulton, T.P., and Monger, J.W.H., 1998, Chapter 2 Field Trip A1: Calgary-Vancouver, *in* Smith, P.L., ed., Field Guide for the Fifth International Symposium on the Jurassic System, Vancouver, Jurassic Subcommission of the Stratigraphic Commission of the International Union of Geological Sciences, Vancouver, 29–61.

Hall, R.L., McNicoll, V., Gröcke, D., Craig, J., and Johnston, K., 2004, Integrated stratigraphy of the lower and middle Fernie Formation in Alberta and British Columbia, Western Canada. Riv. Ital. Pal. Strat. 110, 61–68.

Harries, P., and Little, C.T.S., 1999, The early Toarcian (Early Jurassic) and Cenomanian-Turonian Late Cretaceous, mass extinctions, similarities and contrasts. Palaeogeo. Palaeoclim. Palaeoecol. 154, 39–66.

Hayes, J.M., 2001, Fractionation of Carbon and Hydrogen Isotopes in Biosynthetic Processes, Rev. Min. Geochem. 43, 225–277.

Hayes, J.M., Strauss, H., and Kaurman, A.J., 1999, The abundance of ^{13}C in marine organic matter and isotopic fractionation in the global biogeochemical cycle of carbon during the past 800 Ma. Chem Geol. 161, 103–125.

Hermoso, M., Minoletti, F., Rickaby, R.E.M., Hesselbo, S.P., Baudin, F., and Jenkyns, H.C., 2012, Dynamics of a stepped carbon-isotope excursion: Ultra high-resolution study of Early Toarcian environmental change. Earth Planet. Sci. Lett. 319-320, 45–54.

Hesselbo, S.P., Gröcke, D.R., Jenkyns, H.C., Bjerrum, C.J., Farrimond, P., Morgans Bell, H.S., and Green, O.R., 2000, Massive dissociation of gas hydrate during a Jurassic oceanic anoxic event. Nature 406, 392–395.

Hesselbo, S.P., Jenkyns, H.C., Duarte, L.V., and Oliveira, L.C.V., 2007, Carbon-isotope record of the Early Jurassic (Toarcian) Oceanic Anoxic Event from fossil wood and marine carbonate Lusitanian Basin, Portugal. Earth Planet. Sci. Lett. 253, 455–470.

Hesselbo, S.P., and Pieńkowski, G., 2011, Stepwise atmospheric carbon-isotope excursion during the Toarcian Oceanic Anoxic Event (Early Jurassic, Polish Basin). Earth Planet. Sci. Lett. 301, 365–372.

Howarth, M.K., 1978, The stratigraphy and ammonite fauna of the Upper Lias of Northamptonshire. Bull. Brit. Mus. (Nat. Hist.) 29, 235–288.

Izumi, K., Miyaji, T., and Tanabe, K., 2012, Early Toarcian (Early Jurassic) oceanic anoxic event recorded in the shelf deposits in the northwestern Panthalassa: Evidence from the

Nishinakayama Formation in the Toyora area, west Japan. Palaeogeo. Palaeoclim. Palaeoecol. 315-316, 100–108.

Jakobs, G.K., 1997, Toarcian (Early Jurassic) Ammonoids from Western North America. Geol. Surv. Can. Bull. 428, 1–137.

Jenkyns, H.C., 1988, The early Toarcian (Jurassic) anoxic event: Stratigraphic, sedimentary, and geochemical evidence. Am. J. Sci. 288, 101–151.

Jenkyns, H.C., 2010, Geochemistry of oceanic anoxic events. G^3 11, Q03004.

Jenkyns, H.C., Gröcke, D.R., and Hesselbo, S.P., 2001, Nitrogen isotope evidence for water mass denitrification during the early Toarcian (Jurassic) oceanic anoxic event. Paleoceanography 16, 593–603.

Kemp D.B., Coe, A.L., Cohen, A.S., and Schwark, L., 2005, Astronomical pacing of methane release in the Early Jurassic period. Nature 437, 396–399.

Kemp, D.B., and Izumi, K., 2014, Multiproxy geochemical analysis of a Panthalassic margin record of the Early Toarcian oceanic anoxic event (Toyora area, Japan). Palaeogeo. Palaeoclim. Palaeoecol. 414, 332–341.

Koopmans, M.P., et al., 1996, Diagenetic and catagenetic products of isorenieratene: Molecular indicators for photic zone euxinia. Geochim. Cosmochim. Acta 60, 4467–4496.

Lyons, T.W., and Severmann, S., 2006, A critical look at iron paleoredox proxies: New insights from modern euxinic marine basins. Geochim. Cosmochim. Acta 70, 5698–5722.

Lyons, T.W., Anbar, A.D., Severmann, S., Scott, C., and Gill, B.C., 2009, Tracking Euxinia in

the Ancient Ocean: A Multiproxy Perspective and Proterozoic Case Study. Ann. Rev. Earth Plan. Sci 37, 507–534.

März, C., Poulton, S.W., Beckmann, B., Küster, K., Wagner, T., and Kasten, S., 2008, Redox sensitivity of P cycling during marine black shale formation: Dynamics of sulfidic and anoxic, non-sulfidic bottom waters. Geochim. Cosmochim. Acta 72, 3703–3717.

McCartney, T., Leier, A., Asgar-Deen, M., and Raines, K., 2010a, A New Interpretation of Early Jurassic Basin History in Western Canada. GeoCanada 2010, Calgary Canada.

McCartney, T., Leier, A., Raines, K., and Kukuluski, R., 2010b, Lower Jurassic Foreland Basin in Western Canada. Geol. Soc. Am. Ab. Pr., Denver, Colorado, 272-8.

McCartney, T., and Leier, A., 2011, Tectonic Subsidence Variations in the Jurassic of West-central Alberta, Recovery - CSPG CSEG SWLS Convention.

McCartney, T., and Leier, A., 2012, Tectonic setting of the lower Fernie Formation: insights from subsidence analysis, GeoConvention 2012: Vision.

Montoya-Pino, C., Weyer, S., Anbar, A.D., Pross, J., Oschmann, W., van de Schootbrugge, B., and Arz, H.W., 2010, Global enhancement of ocean anoxia during Oceanic Anoxic Event 2: A quantitative approach using U isotopes. Geology 38, 315–318.

Nielsen, S.G., Goff, M., Hesselbo, S.P., Jenkyns, H.C., LaRowe, D.E., and Lee, C.-T.A., 2011, Thallium isotopes in early diagenetic pyrite – A paleoredox proxy? Geochim. Cosmochim. Acta 75, 6690–6704.

Owens, J.D., et al., 2012, Iron isotope trace metal records of iron cycling in the proto-North Atlantic during the Cenomanian-Turonian oceanic anoxic event (OAE-2). Paleoceanography 27, PA3223.

Owens, J.D., et al., 2013, Sulfur isotopes track the global extent and dynamics of euxinia during Cretaceous Oceanic Anoxic Event 2. Proc. Nat. Acad. Sci. 110, 18407–18412.

Pálfy, J., and Smith, P.L., 2000, Synchrony between Early Jurassic extinction, oceanic anoxic event, and the Karoo-Ferrar flood basalt volcanism. Geology 28, 747–750.

Pancost, R.D., Crawford, N., Magness, S., Turner, A., Jenkyns, H.C., and Maxwell, J.R., 2004, Further evidence for the development of photic-zone euxinic conditions during Mesozoic oceanic anoxic events. J. Geol. Soc. Lon. 161, 353–364.

Phelps, R.M., Kerans, C., Da-Gama, R.O.B.P., Jeremiah, J., Hull, D., and Louks, R.G., 2015, Response and recovery of the Comanche carbonate platform surrounding multiple Cretaceous oceanic anoxic events, northern Gulf of Mexico. Cretac. Res. 54, 117–144.

Poulton, S.W., and Canfield, D.E., 2005, Development of a sequential extraction procedure for iron: implications for iron partitioning in continentally derived particulates. Chem. Geol. 214, 209–221.

Poulton, S.W., and Canfield, D.E., 2011, Ferruginous conditions: A dominant feature of the ocean through Earth's history. Elements 7, 107–112.

Poulton, S.W., and Raiswell, R., 2002, The low-temperature geochemical cycle of iron: From continental fluxes to marine sediment deposition. Amer. J. Sci. 302, 774–805.

Poulton, S.W., et al., 2015, A continental-weathering control on orbitally driven redox-nutrient cycling during Cretaceous Oceanic Anoxic Event 2. Geology 43, 963–966.

Poulton, T.P., 1989, Upper Absaroka to Lower Zuni: the transition to the foreland basin in Western Canada sedimentary basin: A case history, B.D. Ricketts, ed.: Can. Soc. Petr. Geol., 233–247.

Poulton, T.P., Tittemore, J., and Dolby, G., 1990, Jurassic strata of northwestern (and west-central) Alberta and northeastern British Columbia. Geology of the Peace River Arch. *in* O'Connell, S.C., and Bell, J.S., eds., Can. Soc. Petr. Geol. Albert. Res. Council 38A, 236–249.

Poulton, T.P., Christopher, J.E., Hayes, B.J.R., Losert, J., Tittemore, J., and Gilchrist, R.D., 1994, Cordilleran tectonics and the evolution of the Western Canada Sedimentary Basin. Chapter 2 – Jurassic and Lowermost Cretaceous Strata of the Western Canada Sedimentary Basin, *in* Mossop, G. D. and Shetsen, I., eds., Can. Soc. Petr. Geol., 297–316.

Price, R. A., 1994, Cordilleran tectonics and the evolution of the Western Canada Sedimentary Basin. Chapter 18 – Geological Atlas of the Western Canada Sedimentary Basin, *in* Mossop, G. D. and Shetsen, I., eds., Can. Soc. Petr. Geol., 15–24.

Raiswell, R., Newton, R., and Wignall, P.B., 2001, An Indicator of Water-Column Anoxia: Resolution of Biofacies Variations in the Kimmeridge Clay (Upper Jurassic, U.K.), J. Sed. Res. 71, 286–294.

Raiswell, R., and Canfield, D.E., 1998, Sources of iron for pyrite formation in marine sediments. Am. J. Sci. 298, 219–245.

Riediger, C.L., Fowler, M.G., Snowdon, L.R., Goodarzi, F., and Brooks, P.W., 1990, Source

rock analysis of the Lower Jurassic "Nordegg Member" and oil – source rock correlations in northwestern Alberta and northeastern British Columbia. Geology of the Peace River Arch. *in* O'Connell, S.C., and Bell, J.S., eds., Can. Soc. Petr. Geol. Albert. Res. Council 38A, 159–175.

Rohais, S., Crombez, V., Euzen, T., and Baudin, F., 2016, The Lower and Middle Triassic of Western Canada: Passive marine, Back-Arc or Fore-Arc geodynamic setting? GeoConvention 2012: Optimizing Resources.

Salem, N.-E., 2013, Geochemical characterization of the Pliensbachian-Toarcian boundary during the onset of the Toarcian Oceanic Anoxic Event. North Yorkshire, UK, PhD thesis, University of Newcastle, 296 pp.

Savrda, C.E., and Bottjer, D.J., 1987, The exaerobic zone, a new oxygen-deficient marine biofacies. Nautre 327, 54–56.

Schlanger, S.O., and Jenkyns, H.C., 1976, Cretaceous Oceanic Anoxic Events: Causes and Consequences. Geologie en Mijnbouw 55, 179–184.

Schlanger, S.O., Arthur, M.A., Jenkyns, H.C., and Scholle, P.A., 1987, The Cenomanian-Turonian Oceanic Anoxic Event, I. Stratigraphy and distribution of organic-rich beds and the marine $\delta^{13}C$ excursion. Geol. Soc. Lon. Spec. Pub. 26, 371–399.

Schouten, S., van Kaam-Peters, H.M.E., Rijpstra, W.I.C., Schoell, M., and Damsté, J.S.S., 2000, Effects of an oceanic anoxic event on the stable carbon isotopic composition of early Toarcian carbon. Am. J. Sci. 300, 1–22.

Schwark, L., and Frimmel, A., 2004, Chemostratigraphy of the Posidonia Black Shale, SW Germany: I. Influence of sea-level variation on organic facies evolution. Chem. Geol. 206, 199–230.

Scotese, C.R., 2001, Atlas of Earth History. PALEOMAP Project, Arlington, Texas.

Severmann, S., Lyons, T.W., Anbar, A., McManus, J., and Gordon, J., 2008, Modern iron isotope perspective on the benthic iron shuttle and the redox evolution of ancient oceans. Geology 36, 487–490.

Stookey, L.L., 1970, Ferrozine – A New Spectrophotometric Reagent for Iron. Analy. Chem. 42, 779–781.

Suan, G., et al. 2011, Polar record of Early Jurassic massive carbon injection. Earth Planet. Sci. Lett. 312, 102–113.

Suan, G., van de Schootbrugge, B., Adatte, T., Fiebig, J., and Oschmann, W., 2015, Calibrating the magnitude of the Toarcian carbon cycle perturbation. Paleoceanography 30, 495–509.

Tribovillard, N., Algeo, T.J., Lyons, T., and Riboulleau, A., 2006, Trace metals as paleoredox and paleoproductivity proxies: An update. Chem. Geol. 232, 12–32.

Tsikos, H., et al., 2004, Carbon-isotope stratigraphy recorded by the Cenomanian-Turonian Oceanic Anoxic Event: correlation and implications based on three key localities. J. Geol. Soc. Lon. 161, 711–719.

Tyrrell, T, 1999, The relative influence of nitrogen and phosphorus on oceanic primary productivity. Nature 400, 525–531.

van Bentum, E.C, Hetzel, A., Brumsack, H.-J., Forster, A., Reichart, G.-J., and Damsté, J.S.S., 2009, Reconstruction of water column anoxia in the equatorial Atlantic during the Cenomanian-Turonian oceanic anoxic event using biomarker and trace metal proxies. Palaeogeo. Palaeoclim. Palaeoecol. 280, 489–498.

van Breugal, Y., Baas, M., Schouten, S., Mattioli, E., and Damsté, J.S.S., 2006, Isorenieratane record in black shales from the Paris Basin, France: Constraints on recycling of respired

CO_2 as a mechanism for negative carbon isotope shifts during the Toarcian oceanic anoxic event. Paleoceanography 21, PA4220.

van de Schootbrugge, B., McArthur, J.M., Bailey, T.R., Rosenthal, Y., Wright, J.D., and Miller, K.G., 2005, Toarcian oceanic anoxic event: An assessment of global causes using belemnite C isotope records, Paleoceanography 20, PA3008.

Wignall, P.B., McArthur, J.M., Little, C.T.S., and Hallam, A., 2006, Methane release in the Early Jurassic period: Comment. Nature 442, 441.

8. Figures

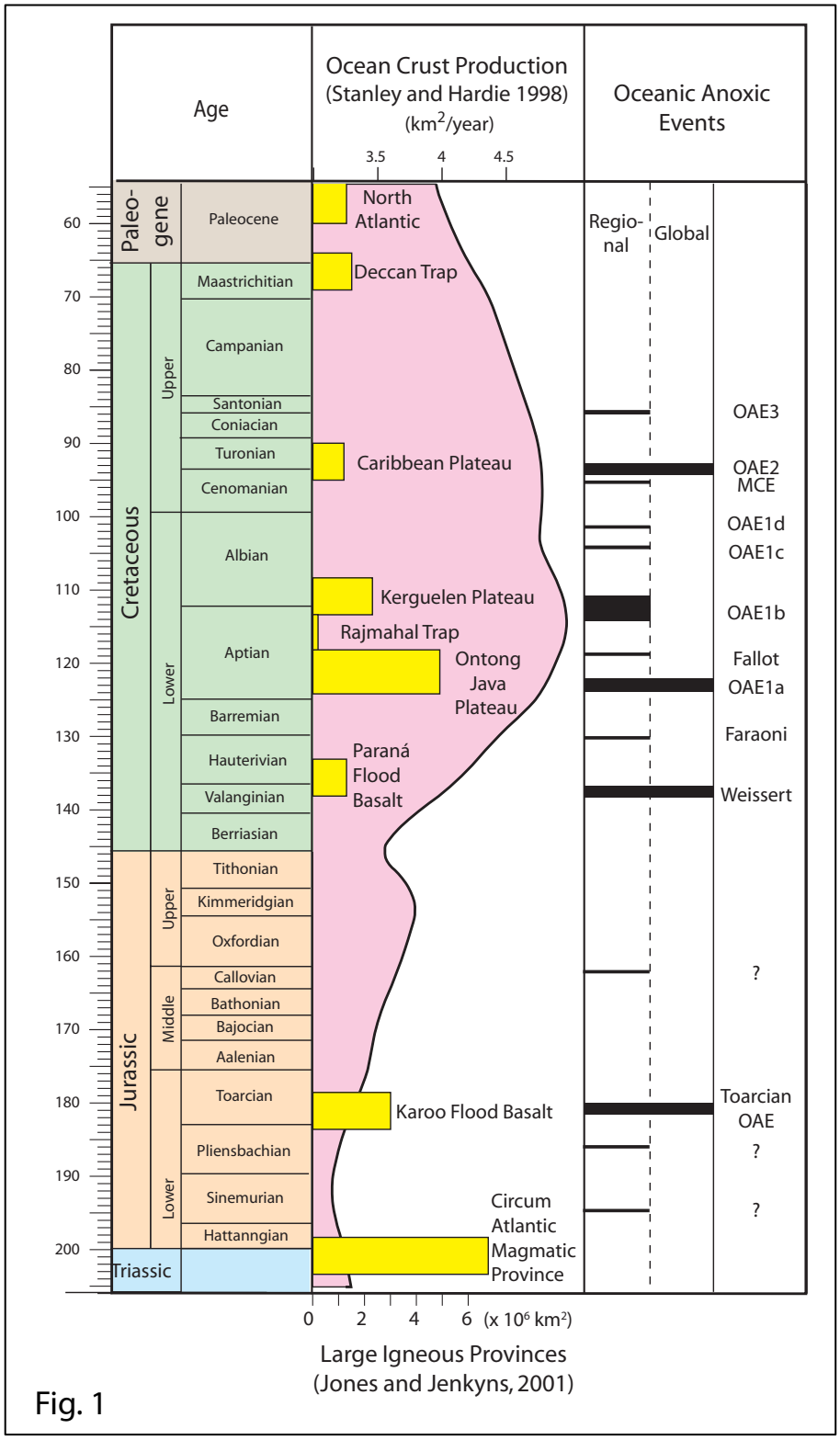

Fig. 1

Figure 1. Incidences of large igneous provinces (LIPs) and oceanic anoxic events (OAEs) during the Mesozoic. The deposition of organic-rich shales is correlated to the emplacement of LIPs, such as flood basalts and ocean plateaus. The Toarcian OAE occurred during the emplacement of the Karoo-Ferrar LIP (modified from Takashima et al., 2006).

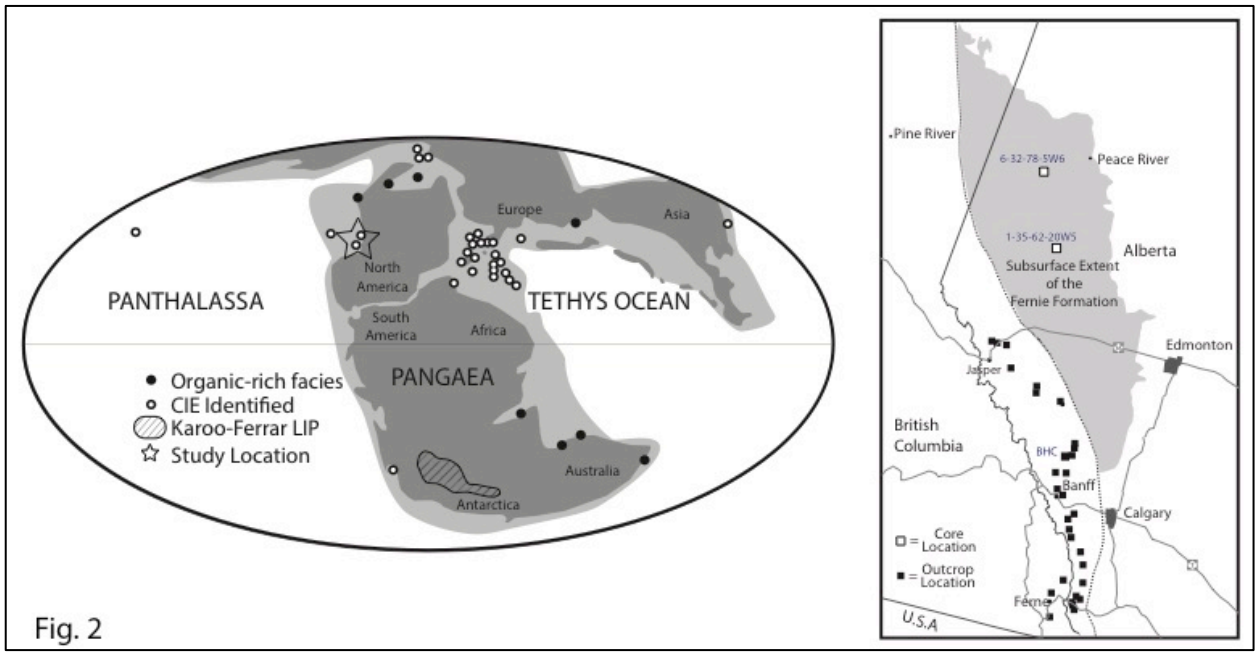

Figure 2. Global paleogeography of the Toarcian and study locations. Black circles represent presence of Toarcian organic-rich facies (updated from Jenkyns, 1988; references in Them et al., (in review)). Open circles represent locations where Toarcian OAE metal data have been published. Hatched outline in southern Africa and Antarctica represents location and extent of Karoo-Ferrar large igneous province. Dark grey represents landmasses, light grey represents shallow seas, and white represents open oceans. Note some circles represent multiple localities in close proximity. Paleogeographic map modified from Scotese (2001). Outcrop and drill core locations in map to right (blue).

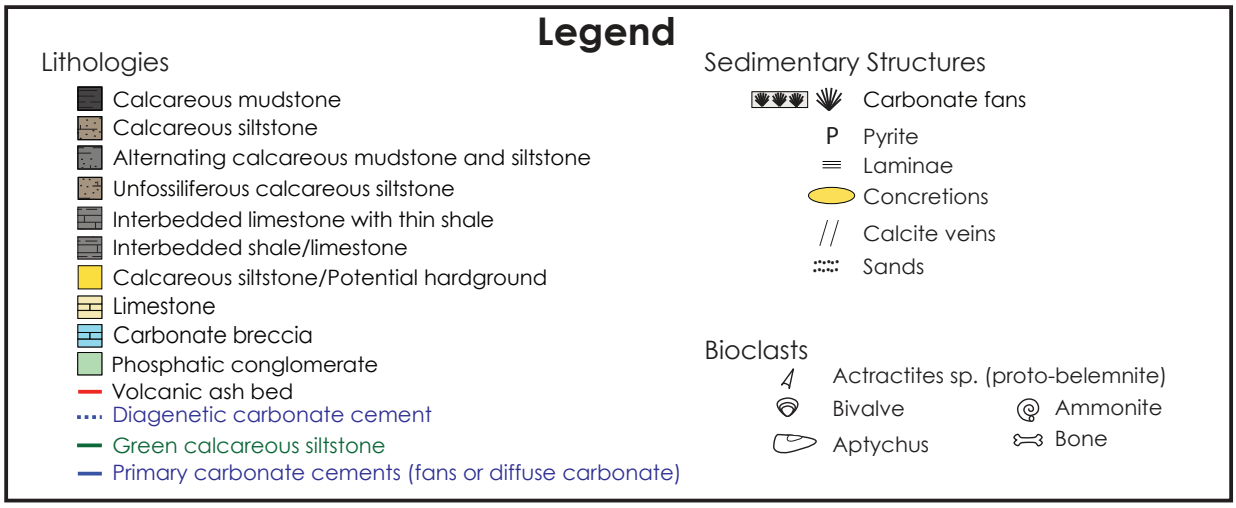
Legend
Lithologies
Calcareous mudstone
Calcareous siltstone
Alternating calcareous mudstone and siltstone
Unfossiliferous calcareous siltstone
Interbedded limestone with thin shale
Interbedded shale/limestone
Calcareous siltstone/Potential hardground
Limestone
Carbonate breccia
Phosphatic conglomerate
Volcanic ash bed
Diagenetic carbonate cement
Green calcareous siltstone
Primary carbonate cements (fans or diffuse carbonate)
Sedimentary Structures
Carbonate fans
P
Pyrite
Laminae
Concretions
Calcite veins
Sands
Bioclasts
Actractites sp. (proto-belemnite)
Bivalve
Ammonite
Aptychus
Bone

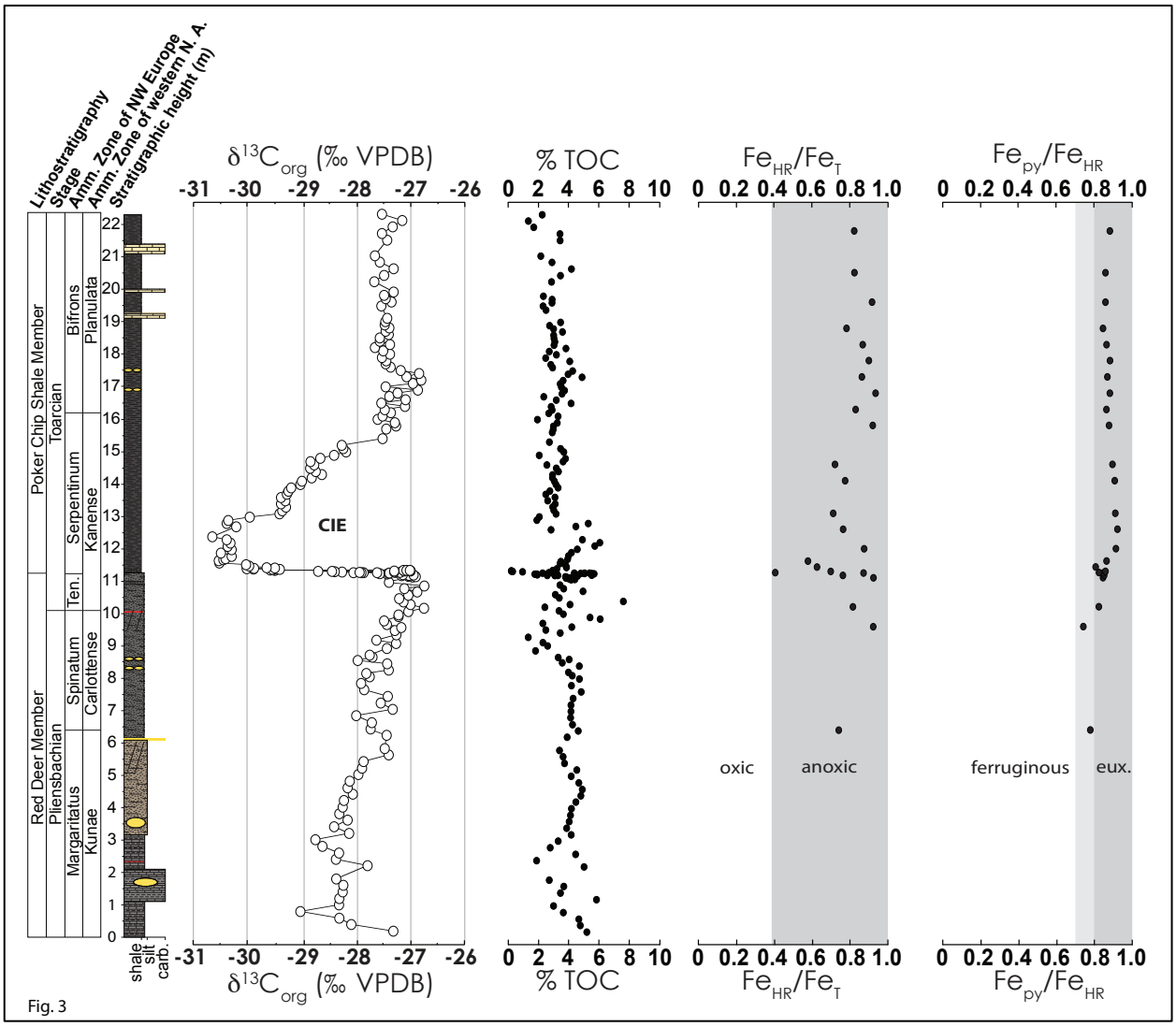
Lithostratigraphy
Stage
Amm. Zone of NW Europe
Amm. Zone of western N. A.
Stratigraphic height (m)
Poker Chip Shale Member
Red Deer Member
Toarcian
Pliensbachian
Ten.
Serpentinum
Spinatum
Margaritatus
Kanense
Carlottense
Kunae
Bifrons
Planulata
CIE
shale
silt
carb.
δ13Corg (‰ VPDB)
% TOC
FeHR/FeT
Fepy/FeHR
oxic
anoxic
ferruginous
eux.

Fig. 3

Figure 3. Carbon isotope and redox proxy data from East Tributary of Bighorn Creek, Alberta. $\delta^{13}C_{org}$ = organic carbon isotopic compositions; TOC = total organic carbon. Fe_T represents total iron, Fe_{HR} represents highly reactive iron-bearing phases, and Fe_{py} represents pyrite iron. Lithostratigraphic members of the Fernie Formation, stages of the Jurassic, and ammonite zonations for both northwestern Europe and western North American shown to the left of the stratigraphic column (refer to Them et al. (in review) for details of the placement of these zonations). Ten. = Tenuicostatum. At this site, Fe_{HR}/Fe_T values suggest anoxic conditions during the whole study interval. Further, Fe_{py}/Fe_{HR} values suggest ferruginous conditions during the Pliensbachian and euxinic conditions during the Toarcian, including the Toarcian OAE.

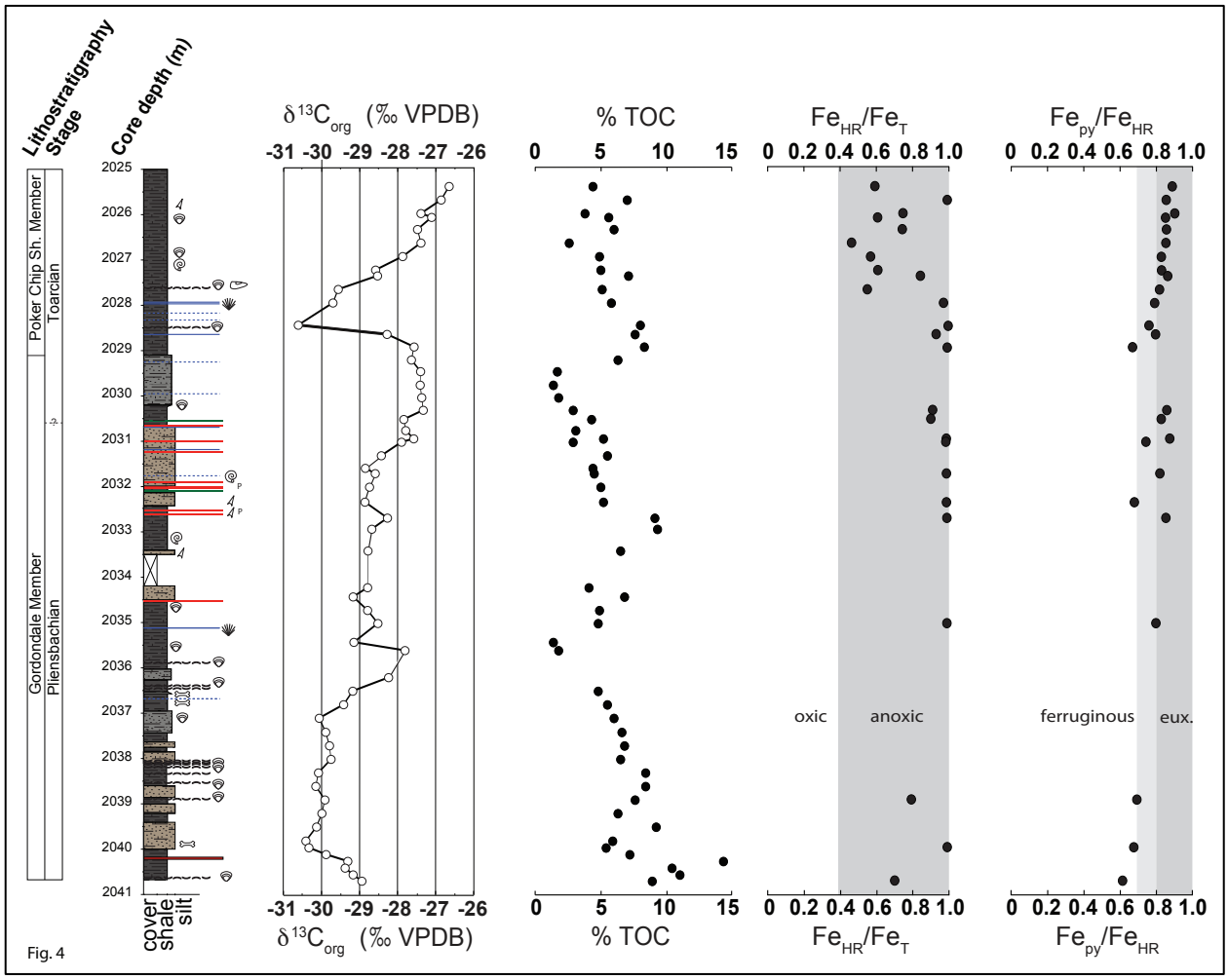

Figure 4. Carbon isotope and redox proxy data from core 1-35-62-20W5. $\delta^{13}C_{org}$ = organic carbon isotopic compositions; TOC = total organic carbon. Fe_T represents total iron, Fe_{HR} represents highly reactive iron-bearing phases, and Fe_{py} represents pyrite iron. Lithostratigraphic members of the Fernie Formation and stages of the Jurassic. At this site, Fe_{HR}/Fe_T values suggest anoxic conditions during the whole study interval. Further, Fe_{py}/Fe_{HR} values suggest ferruginous conditions during the early Pliensbachian and variable ferruginous/euxinic conditions in the later Pliensbachian. During the Toarcian, ferruginous conditions transition to euxinic during the rising $\delta^{13}C$ limb of the Toarcian OAE.

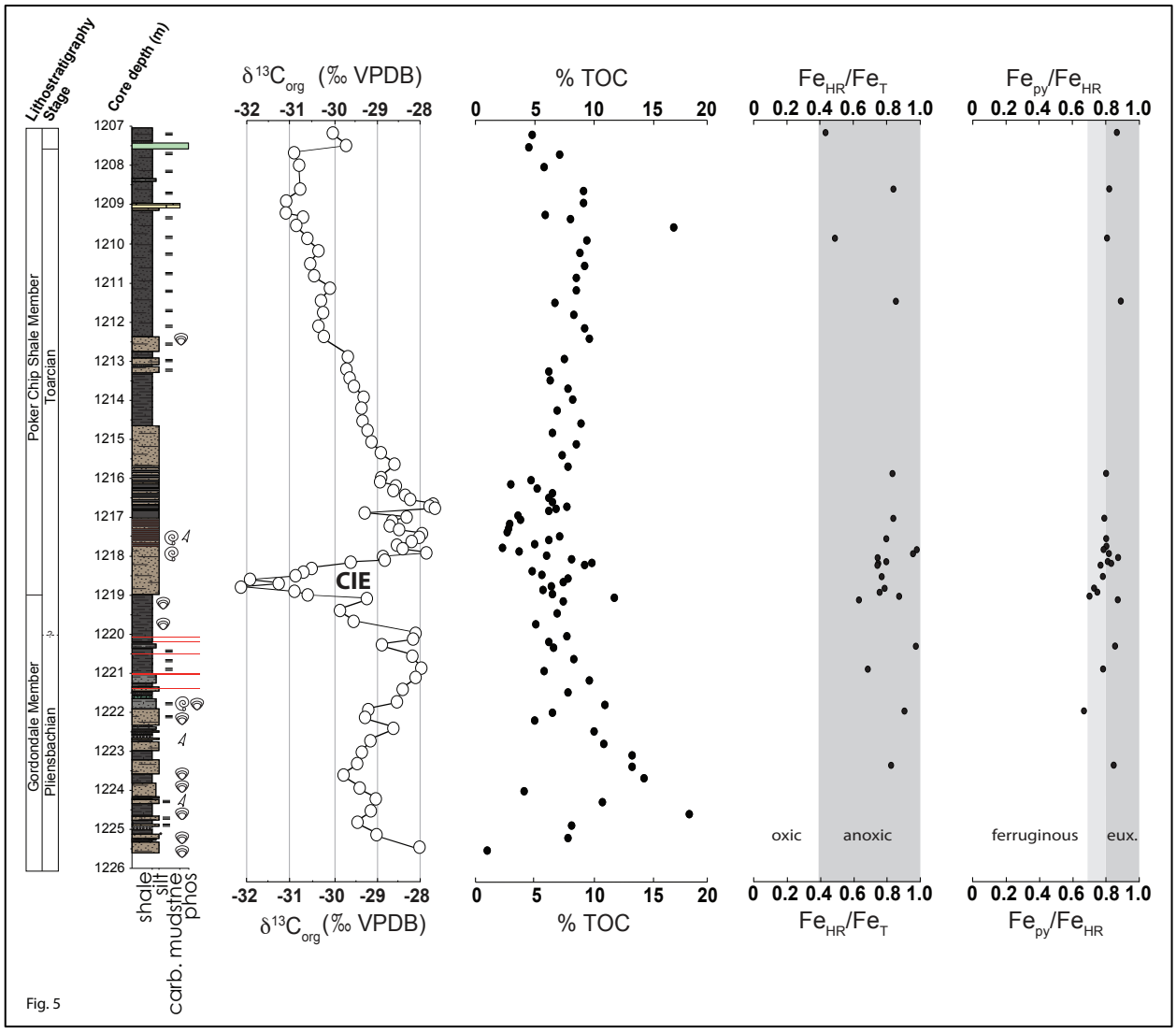

Figure 5. Carbon isotope and redox proxy data from core 6-32-78-5W6. $\delta^{13}C_{org}$ = organic carbon isotopic compositions; TOC = total organic carbon. Fe_T represents total iron, Fe_{HR} represents highly reactive iron-bearing phases, and Fe_{py} represents pyrite iron. Lithostratigraphic members of the Fernie Formation and stages of the Jurassic. At this site, Fe_{HR}/Fe_T values suggest alternating ferruginous and anoxic conditions during the Pliensbachian. At the onset of the Toarcian OAE, Fe_{py}/Fe_{HR} values suggest ferruginous conditions, followed by euxina during the rising $\delta^{13}C$ limb. This site continues to be euxinic well after the end of the Toarcian OAE.

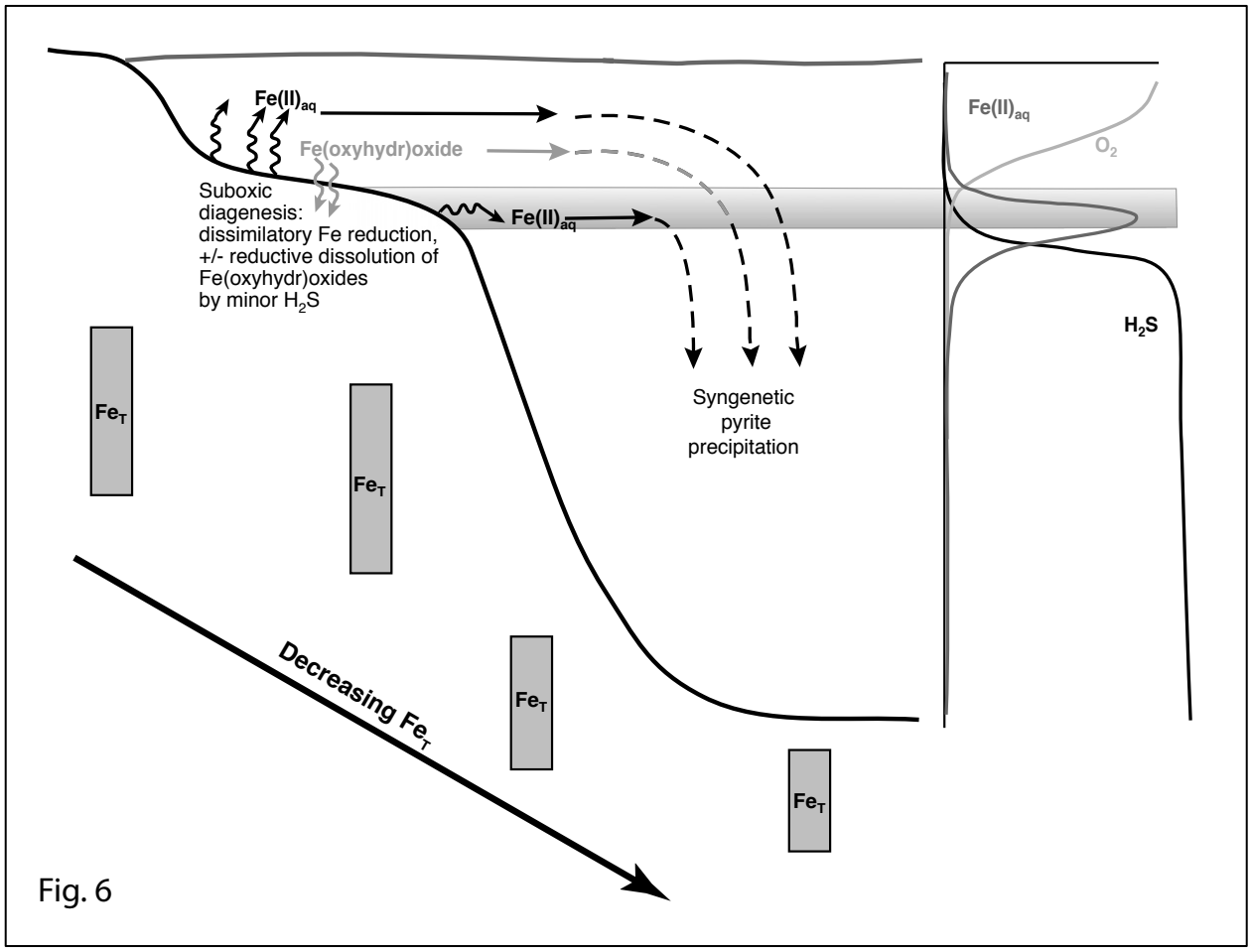

Figure 6. The benthic iron shuttle model. In this scenario, Fe_T values decrease away from land, whereas relative Fe_{HR} values increase. Fe(II) is transported downslope via advection through the water mass and gravity-driven sedimentation (e.g., Raiswell and Canfield, 1998; Anderson and Raiswell, 2004; Lyons and Severmann, 2006; Severmann et al., 2008; Lyons et al., 2009). This scenario is observed in these new iron speciation datasets.

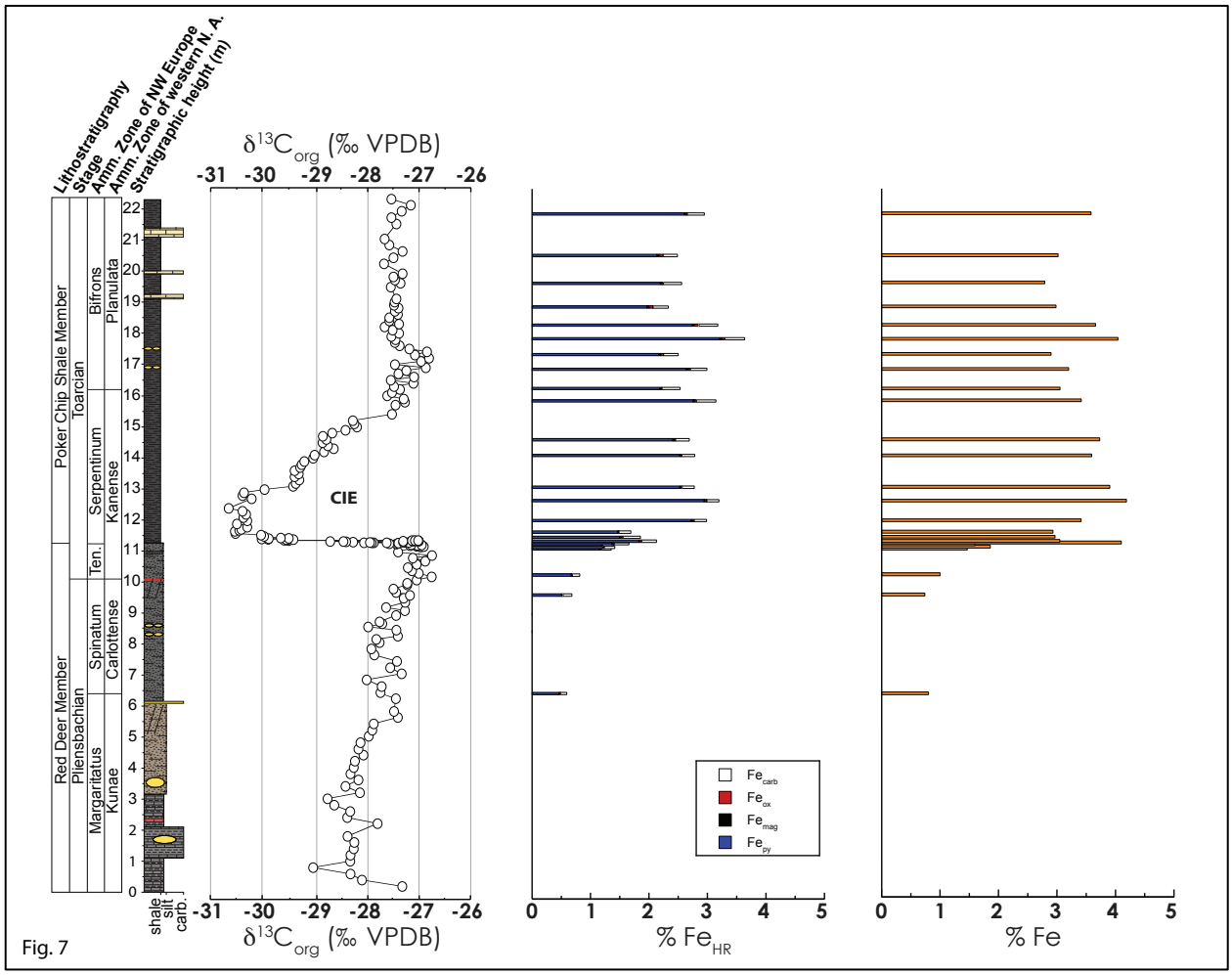

Fig. 7

Figure 7. Iron speciation data from East Tributary of Bighorn Creek, Alberta. $\delta^{13}C_{org}$ = organic carbon isotopic compositions; TOC = total organic carbon. Fe_{HR} represents highly reactive iron-bearing phases, which is the summation of Fe_{carb} (iron hosted in carbonate minerals), Fe_{ox} (iron hosted in oxy-hydroxides), Fe_{mag} (iron hosted in magnetite), and Fe_{py} (pyrite iron). At this site, Fe_{HR} is dominated by Fe_{py}. Furthermore, Fe_T (total iron) values increase during the Toarcian OAE and remain elevated.

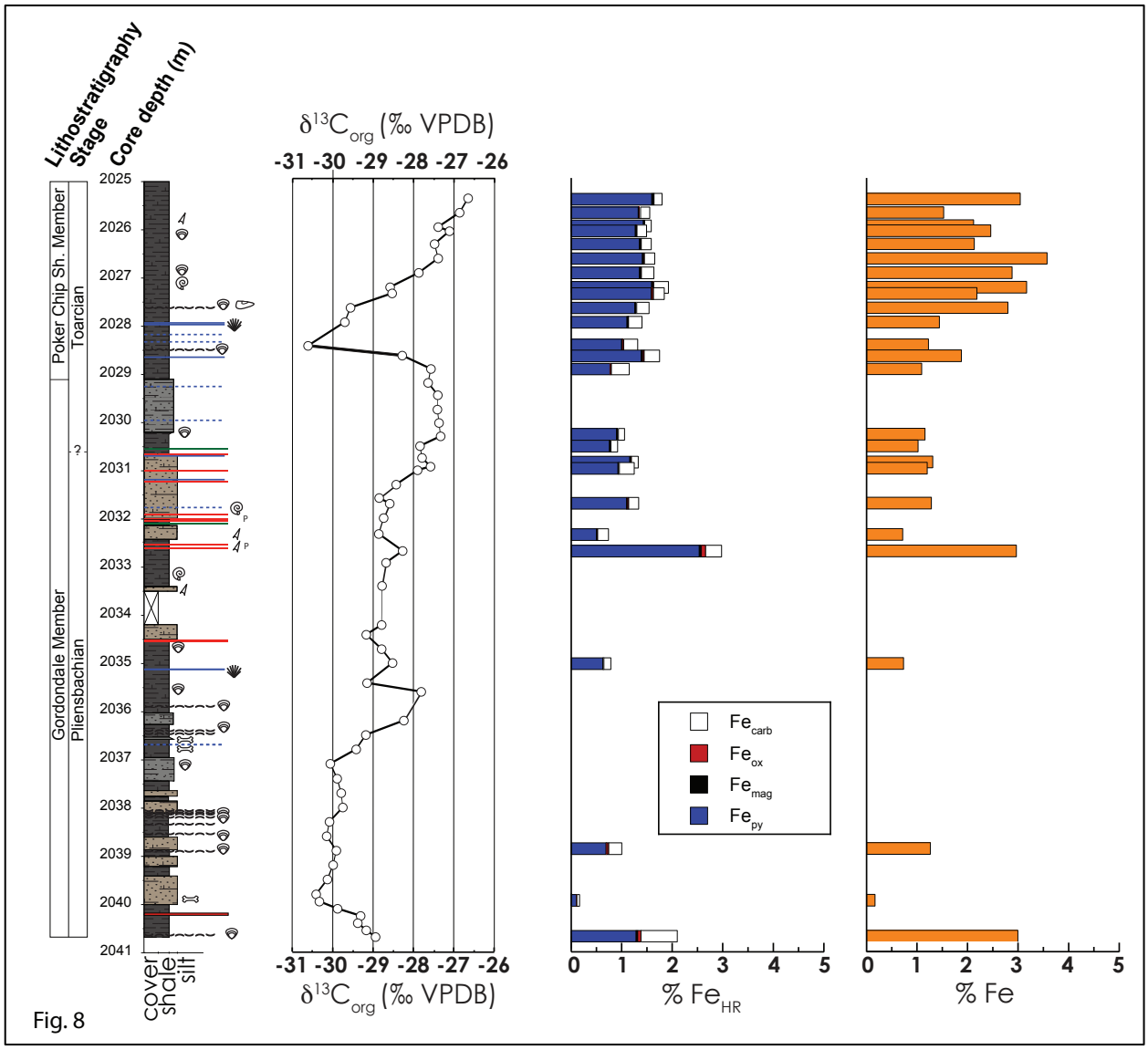

Fig. 8

Figure 8. Iron speciation data from core 1-35-62-20W5. At this site, Fe_{HR} is dominated by Fe_{py}. Fe_T values increase during the Toarcian OAE and remain elevated.

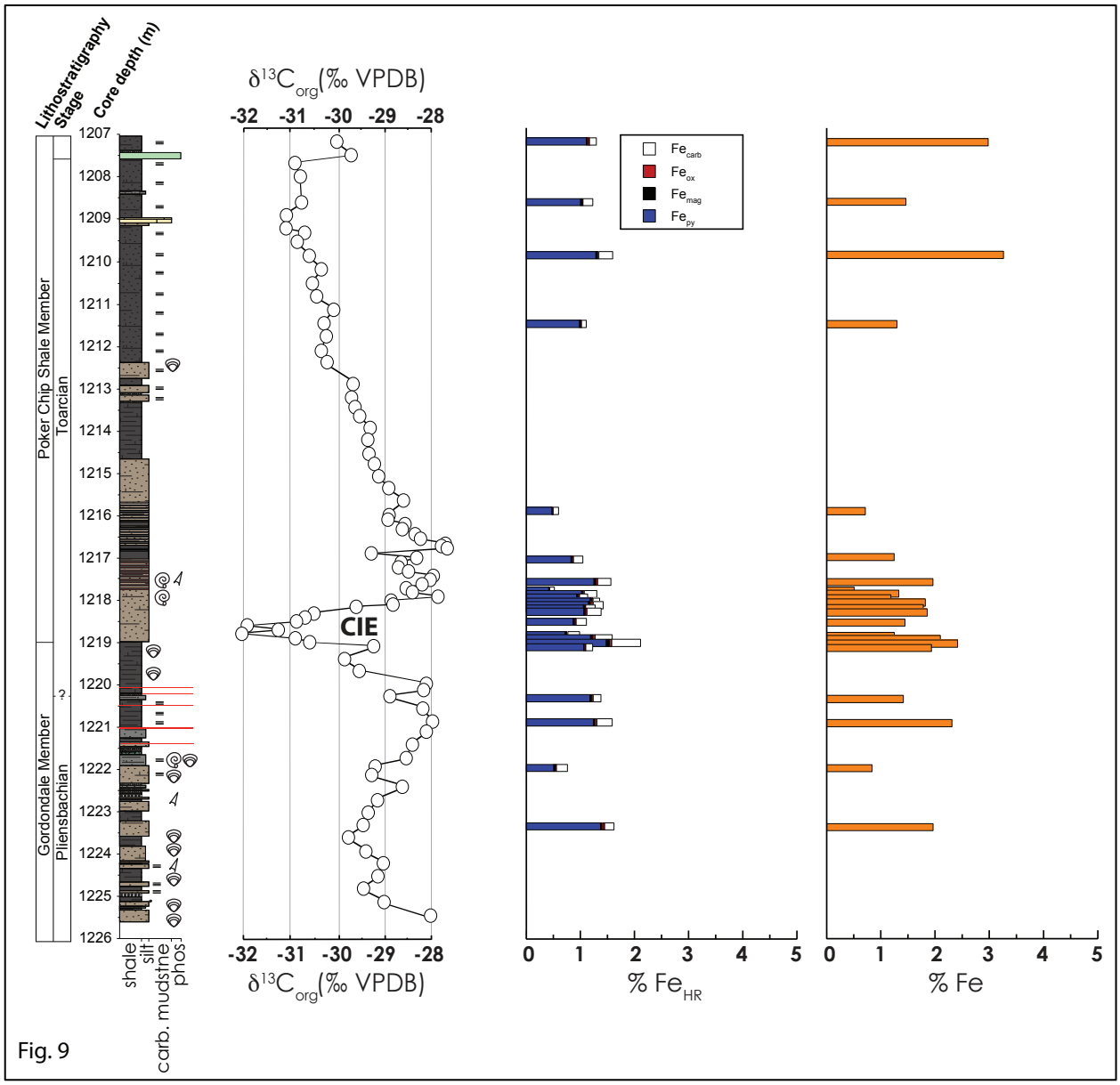

Figure 9. Iron speciation data from core 6-32-78-5W6. At this site, Fe_{HR} is dominated by Fe_{py}. Fe_T values in the Pliensbachian are similar to Toarcian OAE values. The highest values are near the upper portion of the section, reasons for which are discussed in the main text.

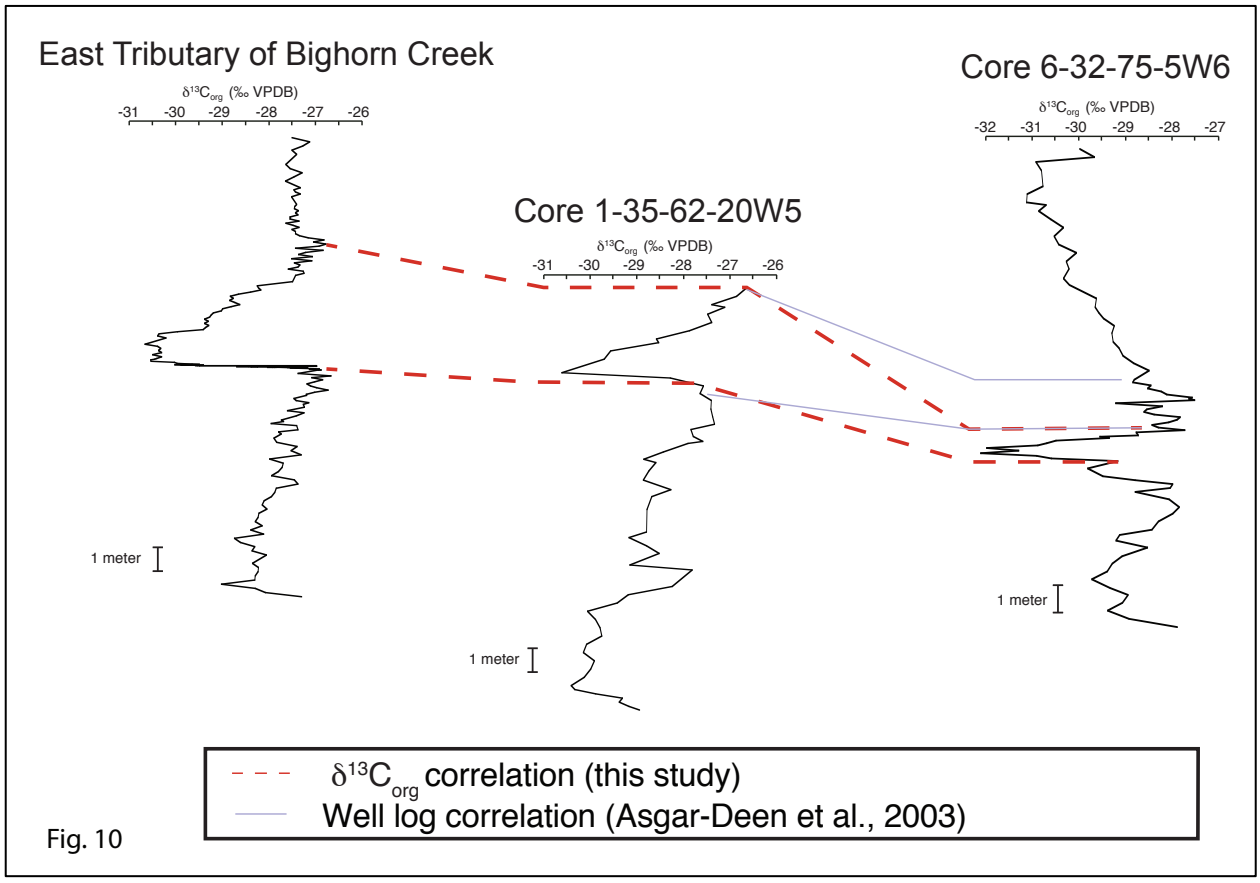

Figure 10. Chemostratigraphic correlation of all three eastern Western Canada Sedimentary Basin sites. The three sites (from proximal to distal) are correlated with their respective $\delta^{13}C_{org}$ values (red dashed line). This provides an update to the well log correlation previously attempted in the two drill cores (solid gray line) (Asgar-Deen et al., 2003).

Conclusions and Future Work

The Toarcian Oceanic Anoxic Event (T-OAE) represents one of the most severe environmental perturbations of the Phanerozoic. In this dissertation, I documented biogeochemical and paleoenvironmental changes associated with the T-OAE from the Western Canada Sedimentary Basin (WCSB). Some of the environmental responses in this region during the Early Jurassic are broadly similar to those in heavily studied sections in Europe, whereas others are very different. The Fernie Formation represents what may be one of the most complete Pliensbachian to Toarcian successions outside of Europe, and future studies on the Fernie will complement the research conducted for this dissertation. Organic geochemical analyses, paired with other elemental and isotopic proxy studies (e.g., trace metals, vanadium, thallium, molybdenum) will result in an even more refined understanding of biogeochemical and paleoenvironmental changes across the T-OAE in eastern Panthalassa. Furthermore, the need remains to locate and conduct similar research on other Toarcian locations from outside of Europe, which will result in a more holistic view of the causes and consequences of the Toarcian Oceanic Anoxic Event.

Appendix A. Chapter 1: East Tributary $\delta^{13}C_{org}$ and TOC.

Height (m)	$\delta^{13}C_{org}$	TOC
0.2	-27.29	5.21
0.4	-28.07	4.78
0.6	-28.29	4.68
0.8	-29.02	3.67
1	-28.3	3.03
1.2	-28.29	5.84
1.4	-28.23	3.48
1.6	-28.22	3.7
1.8	-28.35	2.75
2.2	-28.05	4.96
2.4	-28.36	1.93
2.6	-28.3	4.47
2.8	-28.61	2.81
3	-28.74	3.34
3.2	-28.11	4.19
3.4	-28.39	3.89
3.6	-28.14	4.05
3.8	-28.29	4.14
4	-28.23	4.2
4.2	-28.21	4.49
4.4	-28.04	4.82
4.6	-28.14	4.91
4.8	-28.1	4.68
5	-27.94	4.19
5.2	-27.87	4.55
5.4	-27.84	3.75
5.6	-27.37	3.65
5.8	-27.45	3.42
6	-27.94	1.38
6.2	-27.79	4.52
6.4	-27.71	4.65
6.6	-27.69	4.27
6.8	-27.98	4.15
7	-27.3	4.17
7.2	-27.52	4.17
7.4	-27.39	4.31
7.6	-27.83	4.84
7.8	-27.89	4.2
8	-27.73	4.72

8.1	-27.79	4.25
8.2	-27.37	4.01
8.4	-27.4	4.71
8.5	-27.95	3.6
8.6	-27.68	4.05
8.6625	-27.73	3.34
8.8695	-27.41	1.86
9.0275	-27.24	2.64
9.1225	-27.6	2.34
9.2905	-27.23	1.38
9.4135	-27.26	3.47
9.5135	-27.14	2.53
9.6	-27.41	4.23
9.7075	-27.46	2.33
9.8475	-27.19	6.08
9.9	-27.19	5.42
10	-27.01	3.67
10.1	-26.72	3.39
10.215	-26.97	2.46
10.3	-27.1	4.11
10.4	-27.18	7.57
10.5	-27.01	3.41
10.6	-26.84	3.15
10.7	-27.08	4.96
10.79	-26.66	3.70
10.9	-27.37	3.32
11.066	-26.93	4.19
11.071	-26.87	4.42
11.081	-27.01	4.41
11.091	-26.98	4.04
11.101	-26.98	4.13
11.111	-27	3.86
11.121	-26.91	4
11.131	-27.11	3.87
11.156	-27.4	3.81
11.166	-27.54	4.32
11.176	-27.37	4.59
11.186	-27.36	4.5
11.191	-27.59	3.31
11.194	-27.84	3.14
11.196	-27.88	2.62
11.2	-28.03	3.11
11.203	-27.92	3.18

11.206	-27.25	4.58
11.209	-27.16	5.52
11.212	-27.27	5.53
11.216	-28.24	1.97
11.226	-28.38	3.27
11.236	-28.43	1.95
11.24	-28.69	1.81
11.243	-27.27	5.68
11.246	-26.97	5.55
11.25	-27.08	5.52
11.256	-27.04	4.8
11.259	-26.97	5.05
11.26	-27.1	5.39
11.262	-27.04	5.07
11.264	-26.98	4.39
11.266	-29.49	2.32
11.276	-29.58	2.71
11.286	-29.52	2.82
11.296	-29.54	3.08
11.303	-29.4	3.16
11.308	-29.89	1.01
11.318	-30.02	0.36
11.328	-29.88	0.29
11.338	-29.49	0.28
11.345	-29.65	2.99
11.395	-29.97	3.25
11.445	-30.03	3.87
11.495	-30.53	3.84
11.555	-30.54	3.46
11.588	-30.45	3.56
11.62	-30.41	3.51
11.7	-30.3	3.95
11.8	-30.5	4.01
11.9	-30.3	4.2
12	-30.37	4.58
12.1	-30.32	5.73
12.2	-30.39	6.06
12.3	-30.66	4.92
12.6	-30.21	2.87
12.7	-30.39	4.49
12.8	-30.36	5.3
12.9	-29.96	1.94
13	-29.41	2.11

13.1	-29.36	3.2
13.2	-29.29	3.05
13.3	-29.38	2.98
13.4	-29.3	3.14
13.5	-29.38	2.65
13.6	-29.27	3.13
13.7	-29.24	2.53
13.8	-29.19	2.79
13.9	-29.02	3.33
14	-28.99	3.19
14.1	-28.81	3.09
14.2	-28.62	2.96
14.3	-28.73	2.97
14.4	-28.84	3.35
14.5	-28.76	3.21
14.6	-28.83	2.59
14.7	-28.65	3.65
14.8	-28.39	3.81
14.9	-28.17	2.1
15	-28.22	3.7
15.1	-28.25	3.49
15.3	-27.49	2.76
15.6	-27.42	2.95
15.7	-27.24	3.01
15.8	-27.26	3.02
15.9	-27.58	3.27
16	-27.37	2.98
16.1	-27.33	3.33
16.2	-27.45	2.72
16.3	-27.07	2.94
16.4	-27.51	2.88
16.5	-27.06	4.18
16.6	-27.36	3.21
16.7	-27.21	2.39
16.8	-26.83	3.59
16.9	-27.43	3.75
17	-26.92	3.55
17.1	-26.77	3.47
17.2	-27.04	3.65
17.3	-26.81	4.89
17.4	-27.15	3.98
17.5	-27.34	4.28
17.6	-27.43	2.97

17.7	-27.42	2.85
17.8	-27.5	4.09
17.9	-27.35	2.52
18	-27.48	3.22
18.1	-27.63	2.75
18.2	-27.35	3.84
18.3	-27.54	3.06
18.4	-27.54	3.12
18.5	-27.37	3.06
18.6	-27.43	3.04
18.7	-27.36	3.62
18.8	-27.45	3.03
18.9	-27.44	2.78
19	-27.4	3.49
19.38	-27.51	2.54
19.5	-27.32	2.35
19.6	-27.43	2.93
19.7	-27.46	2.94
19.8	-27.32	3.46
20.12	-27.64	2.9
20.32	-27.46	3.48
20.52	-27.28	4.2
20.72	-27.54	2.93
20.92	-27.63	2.2
21.4	-27.4	3.46
21.6	-27.5	3.45
21.8	-27.27	3.24
22	-27.12	1.39
22.2	-27.5	2.29

Appendix B. Chapter 2: East Tributary rhenium, osmium, $\delta^{13}C_{org}$ and TOC.

Batch/Sample	Stratigraphic height (m)	Re (ppb)	±	Os (ppt)	±
RO718-9_ET30	0.5	255.5	0.6	1041.1	7.0
RO718-8_ET29	1.35	144.6	0.4	692.3	4.4
RO718-6_ET27	2.99	38.5	0.1	241.6	1.5
RO718-7_ET28	3.33	61.4	0.2	421.4	2.5
RO718-5_ET26	4.5	72.5	0.2	433.8	2.7
RO718-4_ET25	5.4	76.1	0.2	457.5	2.7
RO718-1_ET31	6.5	62.6	0.2	730.2	3.3
RO718-3_ET24	7.5	98.8	0.2	710.4	3.8
RO718-2_ET23	8.65	32.3	0.1	467.3	2.3
RO597-10_ET54	9.6	39.6	0.1	495.0	2.5
RO626-8_ET6	9.63	33.9	0.1	394.2	2.4
RO622-3_ET-5	9.9	31.1	0.1	440.2	2.3
RO626-7_ET4	10.35	54.6	0.2	1037.4	4.0
RO626-6_ET2	10.75	58.6	0.1	430.3	2.5
RO622-2_ET-3	10.92	77.7	0.3	952.5	3.5
RO622-1_ET-1	11.12	79.7	0.3	936.0	3.3
RO622-4_ET-7	11.26	55.8	0.2	814.3	3.5
RO629-1_ET-8	11.84	9.8	0.0	187.1	1.3
RO622-5_ET-9	12.02	8.7	0.0	187.0	1.2
RO597-11_ET81	12.6	17.4	0.1	239.5	1.9
RO629-2_ET-10	12.75	12.9	0.0	266.3	1.5
RO622-6_ET-11	13	4.8	0.0	160.4	1.0
RO629-3_ET-12	13.55	9.4	0.0	140.9	1.1
RO626-1_ET13	13.8	9.0	0.0	119.6	1.0
RO629-4_ET-14	14.5	3.9	0.0	103.8	0.7
RO626-2_ET15	14.75	9.6	0.0	121.5	1.0
RO629-5_ET-16	15.1	8.0	0.0	115.1	0.9
RO626-3_ET17	15.25	11.6	0.0	116.0	0.9
RO629-8_ET-22	16.7	82.9	0.3	502.9	2.9
RO626-5_ET21	18.6	33.8	0.2	340.2	2.4
RO629-6_ET-18	19.03	72.4	0.3	376.3	2.6
RO626-4_ET19	19.45	54.6	0.2	314.9	2.3
RO597-12_ET145	19.5	48.7	0.2	368.9	2.4
RO629-7_ET-20	20.51	85.6	0.3	530.3	3.0

Batch/Sample	Stratigraphic height (m)	^{192}Os (ppt)	±	^{187}Re/^{188}Os	±
RO718-9_ET30	0.5	227.2	0.8	2236.9	9.5
RO718-8_ET29	1.35	169.8	0.6	1694.1	7.3
RO718-6_ET27	2.99	68.3	0.3	1121.4	5.8
RO718-7_ET28	3.33	123.0	0.5	992.8	4.6
RO718-5_ET26	4.5	118.5	0.5	1216.2	5.6
RO718-4_ET25	5.4	126.8	0.5	1194.8	5.4
RO718-1_ET31	6.5	248.1	0.9	501.8	2.2
RO718-3_ET24	7.5	214.4	0.8	916.6	4.0
RO718-2_ET23	8.65	162.7	0.7	394.6	1.9
RO597-10_ET54	9.6	170.3	0.8	463.1	2.7
RO626-8_ET6	9.63	133.5	0.8	505.7	3.6
RO622-3_ET-5	9.9	154.1	0.8	401.2	2.5
RO626-7_ET4	10.35	381.8	1.4	284.7	1.4
RO626-6_ET2	10.75	149.3	0.9	450.3	3.1
RO622-2_ET-3	10.92	327.2	0.9	472.7	2.0
RO622-1_ET-1	11.12	318.2	0.7	498.5	2.0
RO622-4_ET-7	11.26	286.4	1.0	387.8	1.9
RO629-1_ET-8	11.84	65.7	0.6	296.4	2.8
RO622-5_ET-9	12.02	66.9	0.5	259.0	2.3
RO597-11_ET81	12.6	80.0	0.8	431.7	4.4
RO629-2_ET-10	12.75	93.9	0.6	272.5	2.0
RO622-6_ET-11	13	58.7	0.5	161.9	1.4
RO629-3_ET-12	13.55	47.4	0.5	393.2	4.0
RO626-1_ET13	13.8	39.8	0.4	451.4	4.9
RO629-4_ET-14	14.5	37.5	0.3	204.7	1.9
RO626-2_ET15	14.75	40.5	0.4	473.0	5.1
RO629-5_ET-16	15.1	39.1	0.4	404.4	4.4
RO626-3_ET17	15.25	36.6	0.3	628.4	6.0
RO629-8_ET-22	16.7	137.4	0.6	1200.1	6.5
RO626-5_ET21	18.6	90.9	0.6	1282.1	8.9
RO629-6_ET-18	19.03	94.2	0.5	1528.1	10.1
RO626-4_ET19	19.45	83.8	0.6	1295.9	9.7
RO597-12_ET145	19.5	110.5	0.6	876.6	5.6
RO629-7_ET-20	20.51	147.4	0.6	1155.1	6.0

Batch/Sample	Stratigraphic height (m)	$^{187}Os/^{188}Os$	±	rho
RO718-9_ET30	0.5	6.9640	0.0346	0.577
RO718-8_ET29	1.35	5.3649	0.0269	0.581
RO718-6_ET27	2.99	3.6622	0.0227	0.634
RO718-7_ET28	3.33	3.3032	0.0187	0.575
RO718-5_ET26	4.5	4.0447	0.0220	0.594
RO718-4_ET25	5.4	3.8838	0.0207	0.590
RO718-1_ET31	6.5	1.7753	0.0090	0.582
RO718-3_ET24	7.5	2.9464	0.0148	0.581
RO718-2_ET23	8.65	1.5538	0.0095	0.602
RO597-10_ET54	9.6	1.6606	0.0106	0.617
RO626-8_ET6	9.63	1.8065	0.0146	0.682
RO622-3_ET-5	9.9	1.5011	0.0109	0.597
RO626-7_ET4	10.35	1.0598	0.0054	0.544
RO626-6_ET2	10.75	1.5866	0.0126	0.667
RO622-2_ET-3	10.92	1.6746	0.0058	0.476
RO622-1_ET-1	11.12	1.7729	0.0056	0.400
RO622-4_ET-7	11.26	1.4600	0.0073	0.514
RO629-1_ET-8	11.84	1.4801	0.0178	0.688
RO622-5_ET-9	12.02	1.3023	0.0149	0.654
RO597-11_ET81	12.6	1.9340	0.0242	0.715
RO629-2_ET-10	12.75	1.4359	0.0123	0.648
RO622-6_ET-11	13	1.1121	0.0127	0.651
RO629-3_ET-12	13.55	1.8589	0.0232	0.716
RO626-1_ET13	13.8	1.9668	0.0255	0.730
RO629-4_ET-14	14.5	1.2283	0.0146	0.675
RO626-2_ET15	14.75	1.9584	0.0252	0.723
RO629-5_ET-16	15.1	1.7781	0.0232	0.734
RO626-3_ET17	15.25	2.4928	0.0264	0.770
RO629-8_ET-22	16.7	4.0467	0.0200	0.686
RO626-5_ET21	18.6	4.3061	0.0295	0.788
RO629-6_ET-18	19.03	5.1050	0.0312	0.781
RO626-4_ET19	19.45	4.3570	0.0331	0.793
RO597-12_ET145	19.5	3.0276	0.0208	0.686
RO629-7_ET-20	20.51	3.8489	0.0183	0.667

Batch/Sample	Stratigraphic height (m)	$\delta^{13}C$	TOC	Age (Ma)
RO718-9_ET30	0.5	-27.98	5.6	187.3521039
RO718-8_ET29	1.35	-28.05	5.5	187.0163907
RO718-6_ET27	2.99	-28.53	4.0	186.3686617
RO718-7_ET28	3.33	-28.18	4.6	186.2343764
RO718-5_ET26	4.5	-28.22	4.1	185.7722771
RO718-4_ET25	5.4	-27.69	4.2	185.416816
RO718-1_ET31	6.5	-27.92	4.2	184.9823637
RO718-3_ET24	7.5	-27.72	3.9	184.587407
RO718-2_ET23	8.65	-27.89	3.8	184.1332067
RO597-10_ET54	9.6	-27.46	4.3	183.7579979
RO626-8_ET6	9.63	-27.52	3.6	183.7461492
RO622-3_ET-5	9.9	-27.06	1.7	183.6395109
RO626-7_ET4	10.35	-26.78	4.1	183.4617803
RO626-6_ET2	10.75	-27.09	5.2	183.3037977
RO622-2_ET-3	10.92	-26.84	4.9	183.236655
RO622-1_ET-1	11.12	-26.94	4.9	183.1576637
RO622-4_ET-7	11.26	-27.05	5.5	183.1023697
RO629-1_ET-8	11.84	-30.49	3.8	183.0650993
RO622-5_ET-9	12.02	-30.54	5.2	183.0541548
RO597-11_ET81	12.6	-30.14	2.9	183.0188893
RO629-2_ET-10	12.75	-30.83	4.8	183.009769
RO622-6_ET-11	13	-30.37	4.1	182.9945683
RO629-3_ET-12	13.55	-29.40	2.5	182.9611269
RO626-1_ET13	13.8	-29.13	2.6	182.9459262
RO629-4_ET-14	14.5	-28.85	2.9	182.9033644
RO626-2_ET15	14.75	-28.70	3.2	182.8881638
RO629-5_ET-16	15.1	-28.33	3.4	182.8668829
RO626-3_ET17	15.25	-28.12	3.6	182.8577625
RO629-8_ET-22	16.7	-27.12	3.3	182.7695987
RO626-5_ET21	18.6	-27.41	3.0	182.6540738
RO629-6_ET-18	19.03	-27.29	3.1	182.6279287
RO626-4_ET19	19.45	-27.13	2.0	182.6023916
RO597-12_ET145	19.5	-27.24	3.1	182.5993514
RO629-7_ET-20	20.51	-27.41	4.2	182.5379408

Batch/Sample	Stratigraphic height (m)	Osi	±
RO718-9_ET30	0.5	-0.029	0.064
RO718-8_ET29	1.35	0.078	0.050
RO718-6_ET27	2.99	0.175	0.041
RO718-7_ET28	3.33	0.218	0.033
RO718-5_ET26	4.5	0.275	0.039
RO718-4_ET25	5.4	0.187	0.037
RO718-1_ET31	6.5	0.227	0.016
RO718-3_ET24	7.5	0.123	0.027
RO718-2_ET23	8.65	0.341	0.015
RO597-10_ET54	9.6	0.241	0.019
RO626-8_ET6	9.63	0.256	0.026
RO622-3_ET-5	9.9	0.272	0.019
RO626-7_ET4	10.35	0.188	0.010
RO626-6_ET2	10.75	0.209	0.022
RO622-2_ET-3	10.92	0.229	0.012
RO622-1_ET-1	11.12	0.250	0.012
RO622-4_ET-7	11.26	0.275	0.013
RO629-1_ET-8	11.84	0.575	0.026
RO622-5_ET-9	12.02	0.511	0.022
RO597-11_ET81	12.6	0.616	0.038
RO629-2_ET-10	12.75	0.604	0.018
RO622-6_ET-11	13	0.618	0.017
RO629-3_ET-12	13.55	0.659	0.035
RO626-1_ET13	13.8	0.589	0.040
RO629-4_ET-14	14.5	0.604	0.020
RO626-2_ET15	14.75	0.515	0.041
RO629-5_ET-16	15.1	0.544	0.037
RO626-3_ET17	15.25	0.575	0.045
RO629-8_ET-22	16.7	0.387	0.040
RO626-5_ET21	18.6	0.399	0.057
RO629-6_ET-18	19.03	0.449	0.062
RO626-4_ET19	19.45	0.409	0.063
RO597-12_ET145	19.5	0.357	0.038
RO629-7_ET-20	20.51	0.331	0.037

Appendix C. Chapter 3: Outcrop and drill core $\delta^{13}C_{org}$, TOC, and iron speciation.

East Tributary

Height (m)	$\delta^{13}C$	TOC	S wt %	S/C
0.2	-27.29	5.21	1.8	0.35
0.4	-28.07	4.78		
0.6	-28.29	4.68		
0.8	-29.02	3.67		
1	-28.3	3.03		
1.2	-28.29	5.84	0.6	0.1
1.4	-28.23	3.48		
1.6	-28.22	3.7		
1.8	-28.35	2.75		
2.2	-28.05	4.96		
2.4	-28.36	1.93	0.6	0.31
2.6	-28.3	4.47		
2.8	-28.61	2.81		
3	-28.74	3.34		
3.2	-28.11	4.19		
3.4	-28.39	3.89	0.9	0.23
3.6	-28.14	4.05		
3.8	-28.29	4.14		
4	-28.23	4.2		
4.2	-28.21	4.49		
4.4	-28.04	4.82	0.5	0.1
4.6	-28.14	4.91	1	0.2
4.8	-28.1	4.68		
5	-27.94	4.19		
5.2	-27.87	4.55		
5.4	-27.84	3.75	0.6	0.16
5.6	-27.37	3.65		
5.8	-27.45	3.42		
6	-27.94	1.38		
6.2	-27.79	4.52		
6.4	-27.71	4.65	0.5	0.11
6.6	-27.69	4.27		
6.8	-27.98	4.15		
7	-27.3	4.17		
7.2	-27.52	4.17		
7.4	-27.39	4.31	0.8	0.19
7.6	-27.83	4.84		

7.8	-27.89	4.2		
8	-27.73	4.72		
8.1	-27.79	4.25		
8.2	-27.37	4.01	0.8	0.2
8.4	-27.4	4.71		
8.5	-27.95	3.6		
8.6	-27.68	4.05		
8.6625	-27.73	3.34		
8.8695	-27.41	1.86		
9.0275	-27.24	2.64		
9.1225	-27.6	2.34	0.6	0.26
9.2905	-27.23	1.38		
9.4135	-27.26	3.47		
9.5135	-27.14	2.53		
9.6	-27.41	4.23		
9.7075	-27.46	2.33		
9.8475	-27.19	6.08		
9.9	-27.19	5.42		
10	-27.01	3.67		
10.1	-26.72	3.39		
10.215	-26.97	2.46	0.8	0.31
10.3	-27.1	4.11		
10.4	-27.18	7.57		
10.5	-27.01	3.41		
10.6	-26.84	3.15		
10.7	-27.08	4.96		
10.79	-26.66	3.7	1	0.27
10.9	-27.37	3.32		
11.066	-26.93	4.19		
11.071	-26.87	4.42		
11.081	-27.01	4.41		
11.091	-26.98	4.04		
11.101	-27.13	4.13	1.3	0.31
11.111	-27	3.86		
11.121	-26.91	4		
11.131	-27.11	3.87		
11.156	-27.4	3.81		
11.166	-27.54	4.32		
11.176	-27.37	4.59	1.4	0.31
11.186	-27.36	4.5		
11.191	-27.59	3.31		
11.194	-27.84	3.14		
11.196	-27.88	2.62		

11.2	-28.03	3.11		
11.203	-27.92	3.18		
11.206	-27.25	4.58		
11.209	-27.16	5.52		
11.212	-27.27	5.53	2.079	0.38
11.216	-28.24	1.97		
11.226	-28.38	3.27		
11.236	-28.43	1.95		
11.24	-28.69	1.81		
11.243	-27.27	5.68		
11.246	-26.97	5.55		
11.25	-27.08	5.52		
11.256	-27.04	4.8	1.352	0.28
11.259	-26.97	5.05		
11.26	-27.1	5.39		
11.262	-27.04	5.07		
11.264	-26.98	4.39		
11.266	-29.49	2.32	1.6	0.69
11.276	-29.58	2.71		
11.286	-29.52	2.82		
11.296	-29.54	3.08		
11.303	-29.4	3.16	2.097	0.66
11.308	-29.89	1.01		
11.318	-30.02	0.36		
11.328	-29.88	0.29		
11.338	-29.49	0.28		
11.345	-29.65	2.99		
11.395	-29.97	3.25		
11.445	-30.03	3.87	1.7	0.44
11.495	-30.53	3.84	2.823	0.74
11.555	-30.54	3.46		
11.588	-30.45	3.56		
11.62	-30.41	3.51	1.7	0.48
11.7	-30.3	3.95		
11.8	-30.5	4.01		
11.9	-30.3	4.2		
12	-30.37	4.58	3.1	0.68
12.1	-30.32	5.73		
12.2	-30.39	6.06		
12.3	-30.66	4.92		
12.6	-30.21	2.87	3.4	1.19
12.7	-30.39	4.49		
12.8	-30.36	5.3		

12.9	-29.96	1.94		
13	-29.41	2.11		
13.1	-29.36	3.2	2.9	0.91
13.2	-29.29	3.05		
13.3	-29.38	2.98		
13.4	-29.3	3.14		
13.5	-29.38	2.65		
13.6	-29.27	3.13	1.8	0.58
13.7	-29.24	2.53		
13.8	-29.19	2.79		
13.9	-29.02	3.33		
14	-28.99	3.19		
14.1	-28.81	3.09	2.9	0.94
14.2	-28.62	2.96		
14.3	-28.73	2.97		
14.4	-28.84	3.35		
14.5	-28.76	3.21		
14.6	-28.83	2.59	2.8	1.08
14.7	-28.65	3.65		
14.8	-28.39	3.81		
14.9	-28.17	2.1		
15	-28.22	3.7		
15.1	-28.25	3.49	2.8	0.8
15.3	-27.49	2.76		
15.6	-27.42	2.95		
15.7	-27.24	3.01		
15.8	-27.26	3.02	3.2	1.06
15.9	-27.58	3.27		
16	-27.37	2.98		
16.1	-27.33	3.33		
16.2	-27.45	2.72		
16.3	-27.07	2.94	2.5	0.85
16.4	-27.51	2.88		
16.5	-27.06	4.18		
16.6	-27.36	3.21		
16.7	-27.21	2.39		
16.8	-26.83	3.59	3	0.84
16.9	-27.43	3.75		
17	-26.92	3.55		
17.1	-26.77	3.47		
17.2	-27.04	3.65		
17.3	-26.81	4.89	2.5	0.51
17.4	-27.15	3.98		

17.5	-27.34	4.28		
17.6	-27.43	2.97		
17.7	-27.42	2.85		
17.8	-27.5	4.09	3.7	0.9
17.9	-27.35	2.52		
18	-27.48	3.22		
18.1	-27.63	2.75		
18.2	-27.35	3.84		
18.3	-27.54	3.06	3.2	1.05
18.4	-27.54	3.12		
18.5	-27.37	3.06		
18.6	-27.43	3.04		
18.7	-27.36	3.62		
18.8	-27.45	3.03	2.3	0.76
18.9	-27.44	2.78		
19	-27.4	3.49		
19.38	-27.51	2.54		
19.5	-27.32	2.35		
19.6	-27.43	2.93	2.5	0.85
19.7	-27.46	2.94		
19.8	-27.32	3.46		
20.12	-27.64	2.9		
20.32	-27.46	3.48		
20.52	-27.28	4.2	2.5	0.6
20.72	-27.54	2.93		
20.92	-27.63	2.2		
21.4	-27.4	3.46		
21.6	-27.5	3.45		
21.8	-27.27	3.24	3	0.93
22	-27.12	1.39		
22.2	-27.5	2.29		

Height (m)	Fe_{carb}	Fe_{ox}	Fe_{mag}	Fe_{py}
0.2				
0.4				
0.6				
0.8				
1				
1.2				
1.4				
1.6				
1.8				
2.2				
2.4				
2.6				
2.8				
3				
3.2				
3.4				
3.6				
3.8				
4				
4.2				
4.4				
4.6				
4.8				
5				
5.2				
5.4				
5.6				
5.8				
6				
6.2				
6.4	0.10807	0.008	0.016	0.46199
6.6				
6.8				
7				
7.2				
7.4				
7.6				
7.8				
8				
8.1				
8.2				
8.4				

8.5				
8.6				
8.6625				
8.8695				
9.0275				
9.1225	0.1516	0.008	0.017	0.5052
9.2905				
9.4135				
9.5135				
9.6				
9.7075				
9.8475				
9.9				
10				
10.1				
10.215	0.12528	0.004	0.015	0.67059
10.3				
10.4				
10.5				
10.6				
10.7				
10.79				
10.9				
11.066				
11.071				
11.081				
11.091				
11.101	0.16628	0.017	0.026	1.1446
11.111				
11.121				
11.131				
11.156				
11.166				
11.176	0.17945	0.017	0.014	1.2063
11.186				
11.191				
11.194				
11.196				
11.2				
11.203				
11.206				
11.209				
11.212				

11.216				
11.226				
11.236				
11.24				
11.243				
11.246				
11.25				
11.256	0.18211	0.013	0.02	1.1771
11.259				
11.26				
11.262				
11.264				
11.266	0.25061	0.016	0.026	1.3636
11.276				
11.286				
11.296				
11.303	0.25437	0.022	0.026	1.826
11.308				
11.318				
11.328				
11.338				
11.345				
11.395				
11.445	0.29573	0.03	0.034	1.495
11.495				
11.555				
11.588				
11.62	0.20216	0.01	0.017	1.4613
11.7				
11.8				
11.9				
12	0.21175	0.021096	0.027473	2.726
12.1				
12.2				
12.3				
12.6	0.2068	0.020049	0.025814	2.9448
12.7				
12.8				
12.9				
13				
13.1	0.20488	0.020977	0.022862	2.525
13.2				
13.3				

13.4				
13.5				
13.6				
13.7				
13.8				
13.9				
14				
14.1	0.21798	0.018411	0.021127	2.5239
14.2				
14.3				
14.4				
14.5				
14.6	0.2321	0.026905	0.022584	2.4073
14.7				
14.8				
14.9				
15				
15.1				
15.3				
15.6				
15.7				
15.8	0.33034	0.033	0.023	2.756
15.9				
16				
16.1				
16.2				
16.3	0.30982	0.008	0.03	2.1849
16.4				
16.5				
16.6				
16.7				
16.8	0.28089	0.036	0.039	2.6356
16.9				
17				
17.1				
17.2				
17.3	0.24926	0.047	0.033	2.1708
17.4				
17.5				
17.6				
17.7				
17.8	0.3412	0.049	0.038	3.2097
17.9				

18				
18.1				
18.2				
18.3	0.31862	0.08	0.033	2.7437
18.4				
18.5				
18.6				
18.7				
18.8	0.26104	0.064	0.036	1.97
18.9				
19				
19.38				
19.5				
19.6	0.31034	0.024	0.03	2.1935
19.7				
19.8				
20.12				
20.32				
20.52	0.24566	0.057	0.05	2.1351
20.72				
20.92				
21.4				
21.6				
21.8	0.29024	0.028	0.031	2.5986
22				
22.2				

Height (m)	Fe_{HR}	Fe_{Tot}	Fe_{py}/Fe_{HR}	Fe_{HR}/Fe_{Tot}
0.2				
0.4				
0.6				
0.8				
1				
1.2				
1.4				
1.6				
1.8				
2.2				
2.4				
2.6				
2.8				
3				
3.2				
3.4				
3.6				
3.8				
4				
4.2				
4.4				
4.6				
4.8				
5				
5.2				
5.4				
5.6				
5.8				
6				
6.2				
6.4	0.594	0.80213	0.778	0.74073
6.6				
6.8				
7				
7.2				
7.4				
7.6				
7.8				
8				
8.1				
8.2				
8.4				

8.5				
8.6				
8.6625				
8.8695				
9.0275				
9.1225	0.682	0.73838	0.741	0.92347
9.2905				
9.4135				
9.5135				
9.6				
9.7075				
9.8475				
9.9				
10				
10.1				
10.215	0.815	0.99861	0.823	0.81592
10.3				
10.4				
10.5				
10.6				
10.7				
10.79				
10.9				
11.066				
11.071				
11.081				
11.091				
11.101	1.354	1.4639	0.845	0.92479
11.111				
11.121				
11.131				
11.156				
11.166				
11.176	1.417	1.859	0.851	0.7624
11.186				
11.191				
11.194				
11.196				
11.2				
11.203				
11.206				
11.209				
11.212				

11.216				
11.226				
11.236				
11.24				
11.243				
11.246				
11.25				
11.256	1.392	1.596	0.846	0.87209
11.259				
11.26				
11.262				
11.264				
11.266	1.656	4.0988	0.824	0.40398
11.276				
11.286				
11.296				
11.303	2.129	3.0482	0.858	0.69839
11.308				
11.318				
11.328				
11.338				
11.345				
11.395				
11.445	1.855	2.9657	0.806	0.62555
11.495				
11.555				
11.588				
11.62	1.691	2.93	0.864	0.57715
11.7				
11.8				
11.9				
12	2.986	3.4132	0.913	0.87492
12.1				
12.2				
12.3				
12.6	3.197	4.1879	0.921	0.76351
12.7				
12.8				
12.9				
13				
13.1	2.774	3.9015	0.91	0.71095
13.2				
13.3				

13.4				
13.5				
13.6				
13.7				
13.8				
13.9				
14				
14.1	2.781	3.5924	0.907	0.77424
14.2				
14.3				
14.4				
14.5				
14.6	2.689	3.7305	0.895	0.7208
14.7				
14.8				
14.9				
15				
15.1				
15.3				
15.6				
15.7				
15.8	3.143	3.4144	0.877	0.92038
15.9				
16				
16.1				
16.2				
16.3	2.533	3.0513	0.863	0.83003
16.4				
16.5				
16.6				
16.7				
16.8	2.992	3.1987	0.881	0.93531
16.9				
17				
17.1				
17.2				
17.3	2.5	2.8969	0.868	0.86308
17.4				
17.5				
17.6				
17.7				
17.8	3.638	4.0416	0.882	0.90022
17.9				

18				
18.1				
18.2				
18.3	3.175	3.6595	0.864	0.86756
18.4				
18.5				
18.6				
18.7				
18.8	2.331	2.9814	0.845	0.78186
18.9				
19				
19.38				
19.5				
19.6	2.558	2.79	0.858	0.91667
19.7				
19.8				
20.12				
20.32				
20.52	2.487	3.0191	0.858	0.82386
20.72				
20.92				
21.4				
21.6				
21.8	2.948	3.5844	0.881	0.82258
22				
22.2				

Core 1-35-62-5W6

Depth (m)	$\delta^{13}C$	TOC	S wt %	S/C
2025.4	-26.64	4.3	1.8321	0.42284
2025.7	-26.85	6.9	1.5249	0.22227
2026	-27.38	3.7	1.6385	0.44744
2026.1	-27.1	5.5	1.4574	0.26524
2026.3	-27.47	5.9	1.5571	0.26592
2026.6	-27.38	2.5	1.6188	0.64585
2026.9	-27.86	4.8	1.5525	0.32201
2027.2	-28.57	4.9	1.8304	0.37444
2027.3	-28.52	7	1.8221	0.25879
2027.6	-29.55	5	1.4443	0.28869
2027.9	-29.69	5.7	1.2712	0.22207
2028.4	-30.6	7.9	1.1455	0.14522
2028.6	-28.27	7.5	1.5949	0.21129
2028.9	-27.56	8.2	0.88213	0.10715
2029.2	-27.63	6.2		
2029.4	-27.39	1.6		
2029.7	-27.4	1.3		
2030	-27.36	1.7		
2030.3	-27.32	2.8	1.0381	0.37186
2030.5	-27.83	4.2	0.87116	0.20904
2030.7	-27.78	3		
2030.9	-27.57	5.1	1.3304	0.26345
2031	-27.89	2.8	1.0634	0.37798
2031.3	-28.42	5.4		
2031.6	-28.84	4.3		
2031.7	-28.58	4.4	1.2578	0.28803
2032	-28.73	4.9		
2032.3	-28.85	5.1	0.57529	0.11232
2032.7	-28.26	9	2.9129	0.32443
2032.9	-28.67	9.2		
2033.4	-28.77	6.4		
2034.2	-28.78	4		
2034.4	-29.16	6.7		
2034.7	-28.78	4.8		
2035	-28.51	4.7	0.71942	0.15464
2035.4	-29.14	1.3		
2035.6	-27.8	1.7		
2035.9				
2036.2	-28.23			
2036.5	-29.17	4.7		

2036.8	-29.41	5.4		
2037.1	-30.05	5.9		
2037.4	-29.88	6.5		
2037.7	-29.78	6.7		
2038	-29.74	6.4		
2038.3	-30.07	8.3		
2038.6	-30.14	8.3		
2038.9	-29.9	7.5	0.7958	0.10605
2039.2	-29.98	6.2		
2039.5	-30.12	9.1		
2039.8	-30.4	5.8		
2039.9	-30.32	5.3	0.12873	0.024159
2040.1	-29.87	7.1		
2040.2	-29.3	14.2		
2040.4	-29.37	10.3		
2040.6	-29.16	10.9		
2040.7	-28.93	8.8	1.4786	0.16832

Depth (m)	**Fe_{carb}**	**Fe_{ox}**	**Fe_{mag}**	**Fe_{py}**
2025.4	0.16	0.016	0.028	1.5957
2025.7	0.181	0.022	0.025	1.3281
2026	0.126	0.016	0.015	1.427
2026.1	0.19	0.012	0.022	1.2693
2026.3	0.198	0.011	0.02	1.3561
2026.6	0.202	0.018	0.024	1.4099
2026.9	0.246	0.012	0.026	1.3522
2027.2	0.292	0.012	0.027	1.5941
2027.3	0.211	0.022	0.022	1.5869
2027.6	0.242	0.013	0.027	1.2579
2027.9	0.265	0.009	0.02	1.1072
2028.4	0.275	0.028	0.015	0.99765
2028.6	0.304	0.028	0.027	1.3891
2028.9	0.353	0.02	0.009	0.76828
2029.2				
2029.4				
2029.7				
2030				
2030.3	0.12	0.014	0.017	0.9041
2030.5	0.13	0.015	0.015	0.75873
2030.7				
2030.9	0.134	0.015	0.019	1.1587
2031	0.294	0.016	0.012	0.92615

2031.3				
2031.6				
2031.7	0.198	0.022	0.021	1.0955
2032				
2032.3	0.214	0.014	0.01	0.50104
2032.7	0.315	0.085	0.04	2.537
2032.9				
2033.4				
2034.2				
2034.4				
2034.7				
2035	0.138	0.011	0.01	0.62658
2035.4				
2035.6				
2035.9				
2036.2				
2036.5				
2036.8				
2037.1				
2037.4				
2037.7				
2038				
2038.3				
2038.6				
2038.9	0.26	0.036	0.013	0.6931
2039.2				
2039.5				
2039.8				
2039.9	0.051	0.002	0.001	0.11212
2040.1				
2040.2				
2040.4				
2040.6				
2040.7	0.719	0.066	0.028	1.2878

Depth (m)	**Fe_{HR}**	**Fe_{Tot}**	**Fe_{py}/Fe_{HR}**	**Fe_{HR}/Fe_{Tot}**
2025.4	1.8	3.041	0.887	0.592
2025.7	1.556	1.529	0.854	1.018
2026	1.584	2.119	0.901	0.747

2026.1	1.493	2.458	0.85	0.607
2026.3	1.585	2.133	0.855	0.743
2026.6	1.654	3.574	0.852	0.463
2026.9	1.636	2.88	0.827	0.568
2027.2	1.925	3.168	0.828	0.608
2027.3	1.842	2.184	0.862	0.843
2027.6	1.539	2.797	0.817	0.55
2027.9	1.402	1.443	0.79	0.971
2028.4	1.315	1.226	0.759	1.072
2028.6	1.748	1.879	0.795	0.93
2028.9	1.151	1.093	0.668	1.053
2029.2				
2029.4				
2029.7				
2030				
2030.3	1.055	1.1585	0.857	0.911
2030.5	0.918	1.0198	0.826	0.901
2030.7				
2030.9	1.327	1.3117	0.873	1.011
2031	1.248	1.2027	0.742	1.037
2031.3				
2031.6				
2031.7	1.337	1.2844	0.819	1.041
2032				
2032.3	0.738	0.71663	0.678	1.03
2032.7	2.977	2.9664	0.852	1.004
2032.9				
2033.4				
2034.2				
2034.4				
2034.7				
2035	0.786	0.73485	0.797	1.07
2035.4				
2035.6				
2035.9				
2036.2				
2036.5				
2036.8				
2037.1				
2037.4				
2037.7				
2038				
2038.3				

2038.6				
2038.9	1.002	1.2635	0.692	0.793
2039.2				
2039.5				
2039.8				
2039.9	0.166	0.16773	0.675	0.991
2040.1				
2040.2				
2040.4				
2040.6				
2040.7	2.101	2.9964	0.613	0.701

Core 6-32-78-20W5

Depth (m)	$\delta^{13}C$	TOC	S wt %	S/C
1207.2	-29.99	4.8	1.2835	0.26811
1207.5	-29.67	4.5		
1207.7	-30.93	7.1		
1208	-30.81	5.8		
1208.6	-30.78	9.1	1.1537	0.12666
1208.9	-31.12	9.1		
1209.2	-31.13	5.9		
1209.3	-30.71	8		
1209.5	-30.87	16.7		
1209.8	-30.61	9.4	1.4768	0.15727
1210.2	-30.34	8.8		
1210.5	-30.54	9.2		
1210.8	-30.44	8.5		
1211.1	-30.06	8.5		
1211.5	-30.28	6.7	1.1305	0.16849
1211.8	-30.22	8.3		
1212.1	-30.34	9.2		
1212.4	-30.21	9.6		
1212.9	-29.63	7.5		
1213.2	-29.66	6.2		
1213.4	-29.58	6.3		
1213.7	-29.48	7.8		
1213.9	-29.25	8.2		
1214.2	-29.3	6.9		
1214.6	-29.27	8.9		
1214.8	-29.15	6.5		
1215.1	-29.06	8.5		
1215.4	-28.83	7.3		
1215.7	-28.5	7.8		
1215.9				
1216	-28.82	4.7		
1216.1	-28.85	3		
1216.2	-28.46	5.2		
1216.3	-28.53	6.5		
1216.4	-28.24	6.2	1.1317	0.18157
1216.6	-28.12	6.5		
1216.7	-27.57	7.7		
1216.7	-27.65	6.8		
1216.8	-27.52	6.2		
1216.9	-29.22	3.6		

1217	-28.21	3.8	1.0507	0.13697
1217.1	-28.55	2.9		
1217.2	-28.61	2.8		
1217.3	-28.39	2.7		
1217.4	-27.83	7.1		
1217.5	-27.9	6.2	1.4361	0.23239
1217.6	-28.08	5		
1217.7	-28.44	2.3	0.47782	0.2045
1217.8	-28.3	3.7	1.1739	0.31984
1217.9	-27.73	6	1.0634	0.17614
1218	-28.78	8.1	1.3575	0.16667
1218.1	-28.73	9.8	1.3217	0.13454
1218.2	-29.56	9.2	1.2133	0.13162
1218.2	-29.35	7.8	1.2169	0.15525
1218.3	-30.5	4.8		
1218.4	-30.7	5.6		
1218.5	-30.89	7.8	0.99618	0.12788
1218.6	-31.99	7.4		
1218.7	-31.3	6.4		
1218.8	-32.12	5.7	0.82232	0.14316
1218.9	-30.92	6.5	1.3632	0.21023
1219	-30.6	11.7	1.6974	0.14466
1219.1	-29.17	7.4		
1219.4	-29.82	6.9		
1219.7	-29.49	5.1		
1219.8	-28.8	5.9		
1220	-27.99	7.7		
1220.2	-28.05	6.2		
1220.3	-28.8	6.6	1.3505	0.20396
1220.6	-28.07	8.3		
1220.9	-27.85	5.8	1.4248	0.24758
1221.1	-27.99	9.6		
1221.4	-28.3	7.8		
1221.8	-28.44	10.9		
1222	-29.13	6.5	0.58257	0.089984
1222.2	-29.21	5		
1222.4	-28.53	10		
1222.8	-29.08	10.8		
1223.1	-29.29	13.2		
1223.3	-29.4	13.2	1.5735	0.11961
1223.7	-29.73	14.2		
1224	-29.34	4.1		
1224.3	-28.95	10.7		

1224.6	-29.07	18
1224.9	-29.39	8.1
1225.2	-28.93	7.8
1225.5	-27.89	1

Depth (m)	Fe_{carb}	Fe_{ox}	Fe_{mag}	Fe_{py}
1207.2	0.1253	0.01944	0.031022	1.1179
1207.5				
1207.7				
1208				
1208.6	0.17912	0.023012	0.021824	1.0048
1208.9				
1209.2				
1209.3				
1209.5				
1209.8	0.25659	0.023397	0.031649	1.2862
1210.2				
1210.5				
1210.8				
1211.1				
1211.5	0.090012	0.01328	0.021447	0.9846
1211.8				
1212.1				
1212.4				
1212.9				
1213.2				
1213.4				
1213.7				
1213.9				
1214.2				
1214.6				
1214.8				
1215.1				
1215.4				
1215.7				
1215.9	0.097733	0.010955	0.010887	0.47596
1216				
1216.1				
1216.2				
1216.3				
1216.4				
1216.6				

1216.7				
1216.7				
1216.8				
1216.9				
1217	0.17367	0.024583	0.022654	0.82522
1217.1				
1217.2				
1217.3				
1217.4				
1217.5	0.24364	0.034005	0.035244	1.2508
1217.6				
1217.7	0.084069	0.0089509	0.010015	0.41615
1217.8	0.23159	0.026918	0.022786	1.0224
1217.9	0.15019	0.030764	0.027228	0.92615
1218	0.12216	0.026639	0.025322	1.1823
1218.1	0.18548	0.040866	0.044157	1.1511
1218.2	0.1762	0.02286	0.017091	1.0567
1218.2	0.25998	0.02801	0.035006	1.0599
1218.3				
1218.4				
1218.5	0.19138	0.02396	0.02954	0.86762
1218.6				
1218.7				
1218.8	0.21619	0.021804	0.030119	0.7162
1218.9	0.3174	0.041673	0.04254	1.1872
1219	0.53082	0.045614	0.056622	1.4783
1219.1	0.12434	0.020895	0.014758	1.0658
1219.4				
1219.7				
1219.8				
1220				
1220.2				
1220.3	0.14051	0.028956	0.033067	1.1762
1220.6				
1220.9	0.28207	0.038807	0.026523	1.2409
1221.1				
1221.4				
1221.8				
1222	0.20374	0.022256	0.026981	0.50738
1222.2				
1222.4				
1222.8				
1223.1				

1223.3	0.17332	0.035101	0.043276	1.3705
1223.7				
1224				
1224.3				
1224.6				
1224.9				
1225.2				
1225.5				

Depth (m)	**Fe_{HR}**	**Fe_{Tot}**	**Fe_{py}/Fe_{HR}**	**Fe_{HR}/Fe_{Tot}**
1207.2	1.2936	2.9792	0.86413	0.43422
1207.5				
1207.7				
1208				
1208.6	1.2288	1.4626	0.81774	0.84013
1208.9				
1209.2				
1209.3				
1209.5				
1209.8	1.5979	3.2631	0.80497	0.48967
1210.2				
1210.5				
1210.8				
1211.1				
1211.5	1.1093	1.2969	0.88756	0.85538
1211.8				
1212.1				
1212.4				
1212.9				
1213.2				
1213.4				
1213.7				
1213.9				
1214.2				
1214.6				
1214.8				
1215.1				
1215.4				
1215.7				
1215.9	0.59554	0.71365	0.79922	0.8345
1216				
1216.1				

1216.2				
1216.3				
1216.4				
1216.6				
1216.7				
1216.7				
1216.8				
1216.9				
1217	1.0461	1.2461	0.78883	0.83952
1217.1				
1217.2				
1217.3				
1217.4				
1217.5	1.5637	1.9599	0.7999	0.79784
1217.6				
1217.7	0.51919	0.50861	0.80155	1.0208
1217.8	1.3037	1.3298	0.78423	0.98037
1217.9	1.1343	1.1847	0.81647	0.95751
1218	1.3564	1.8195	0.87163	0.74546
1218.1	1.4216	1.7831	0.80972	0.79727
1218.2	1.2729	1.6985	0.83018	0.74941
1218.2	1.3829	1.857	0.76643	0.74468
1218.3				
1218.4				
1218.5	1.1125	1.4446	0.77988	0.77012
1218.6				
1218.7				
1218.8	0.98431	1.2495	0.72761	0.78774
1218.9	1.5889	2.0982	0.74723	0.75723
1219	2.1114	2.4156	0.70017	0.87406
1219.1	1.2258	1.9346	0.86947	0.63359
1219.4				
1219.7				
1219.8				
1220				
1220.2				
1220.3	1.3787	1.4152	0.8531	0.97423
1220.6				
1220.9	1.5883	2.3128	0.78128	0.68677
1221.1				
1221.4				
1221.8				
1222	0.76036	0.83882	0.66729	0.90647

1222.2				
1222.4				
1222.8				
1223.1				
1223.3	1.6222	1.9632	0.84484	0.82629
1223.7				
1224				
1224.3				
1224.6				
1224.9				
1225.2				
1225.5				